



FACULTY OF SCIENCE

School of Physics & Astronomy

The Characterisation of the High  
Throughput Imaging Echelle Spectrograph  
and Investigations of Hydrogen Balmer  $\beta$   
Emission over Svalbard

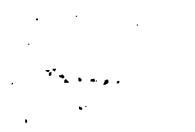
*by*

Stuart Robertson

Thesis for the degree of Doctor of Philosophy

9<sup>th</sup> April 2005

# Contents



<b>1</b>	<b>Introduction</b>	<b>11</b>
1.1	Investigation of Hydrogen Aurora . . . . .	11
1.1.1	Dayside Merging between the IMF and Geomagnetosphere . . . . .	12
1.2	Investigation of Auroral Proton Precipitation over Svalbard . . . . .	14
1.2.1	The Geographic Location of Nordlysstasjonen . . . . .	14
1.2.2	The Geomagnetic Location of Nordlysstasjonen, Svalbard . . . . .	15
1.2.3	Observing the dayside aurora from Svalbard . . . . .	16
1.3	Instrumentation used to investigate Hydrogen Aurora . . . . .	16
1.4	Other Observed Phenomena . . . . .	17
1.4.1	The Hydrogen Geocorona . . . . .	17
1.4.2	Coronal Mass Ejection . . . . .	18
1.4.3	Cosmic Rays . . . . .	18
1.5	Synopsis . . . . .	19
<b>2</b>	<b>Theory of Dayside Proton Aurora</b>	<b>20</b>
<b>3</b>	<b>HiTIES: the High Throughput Imaging Echelle Spectrograph</b>	<b>27</b>
3.1	Spectrograph Components . . . . .	28
3.2	The Echelle Grating . . . . .	28
3.3	The Aperture . . . . .	32
3.4	The Sensor . . . . .	32

3.4.1	The Charge Coupled Device (CCD)	33
3.4.2	Intensified CCD	34
3.5	Practical Instrument considerations	36
<b>4</b>	<b>Spatial Calibration of the Platform</b>	<b>40</b>
4.1	Calibration Of Video Data.	41
4.1.1	Fitting a frame	43
4.2	Calibration Of Photometer Data.	46
4.3	Calibration Of Spectrograph Data.	47
4.3.1	Slit Diffraction	48
4.3.2	Point spread function	49
4.3.3	Star field calibration	50
4.3.4	More Slit Width Measurements	53
4.4	Spatial Correlation With Other Data Sets.	54
<b>5</b>	<b>Spectral Calibration</b>	<b>60</b>
5.1	Spectral Characterisation of the Video Camera	60
5.2	Spectral Characterisation of the Photometers	60
5.3	Spectral Characterisation of the Spectrograph	61
5.3.1	The Echelle Grating	61
5.3.2	Filter Selection	62
5.3.3	Calibrating the Wavelength Scale	65
5.3.4	Calculating the Spectral Resolution	68
<b>6</b>	<b>Brightness Calibration</b>	<b>71</b>
6.1	Surface Brightness Unit	71
6.2	Conventional Brightness Calibration of the Spectrograph	72

6.3	Theoretical Brightness Response . . . . .	72
6.4	A Practical Brightness Calibration Method . . . . .	73
6.4.1	An Efficiency Calculation Using Starlight . . . . .	73
6.5	How Does the Spectrograph Performance Relate to Proton Aurora . . . . .	77
<b>7</b>	<b>Removing Instrumental Artifacts from the Data</b>	<b>79</b>
7.1	Dark Subtraction . . . . .	79
7.1.1	Dark Current . . . . .	79
7.1.2	Read Noise . . . . .	85
7.1.3	Removing the Dark Frame . . . . .	86
7.2	Flat-Fielding . . . . .	87
7.2.1	Natural Vignetting . . . . .	87
7.2.2	Rectifying Pixel Performance Variance . . . . .	87
7.2.3	Flat-Fielding Data Frames . . . . .	89
7.3	Quantisation Noise . . . . .	91
7.4	Warping The Pin Cushion . . . . .	91
7.5	ESR Gain Mask For The Video Camera . . . . .	92
<b>8</b>	<b>Removing External Contaminants from the Data</b>	<b>94</b>
8.1	Removal of sunlight contamination. . . . .	94
8.1.1	Twilight Periods . . . . .	94
8.1.2	Twilight Contamination . . . . .	97
8.2	Cosmic Ray Filtering . . . . .	103
8.3	Removing the unshifted hydrogen line . . . . .	107
8.3.1	Gaussian line fit with Bi-Gaussian profile subtraction . . . . .	107
8.3.2	Ignore the emission . . . . .	108

8.3.3	The flat line fit . . . . .	109
8.3.4	The "targeted" line fit . . . . .	110
<b>9</b>	<b>Investigation of Atmospheric Hydrogen Emission</b>	<b>112</b>
9.1	Observation . . . . .	112
9.2	The possible origin of the emission . . . . .	112
9.2.1	Exospheric Hydrogen . . . . .	113
9.2.2	Thermalised Auroral Hydrogen . . . . .	114
9.3	The Omnipresence of Unshifted Hydrogen Emission . . . . .	115
9.4	A Higher Time Resolution Survey of Unshifted Hydrogen . . . . .	116
9.4.1	Unshifted Hydrogen Line Analysis . . . . .	117
9.4.2	Temporal Behavior of the Unshifted Hydrogen Emission . . . . .	119
9.5	The unshifted hydrogen emission response to the shock on November 26th, 2000	120
9.6	Analysis and Discussion . . . . .	123
<b>10</b>	<b>Measurement of the Auroral Proton Emission.</b>	<b>124</b>
10.1	The Event of November 26 <sup>th</sup> . . . . .	124
10.1.1	Satellite Observations of the Event . . . . .	124
10.1.2	HiTIES H $\beta$ Observations . . . . .	125
10.1.3	The Lummerzheim Bi-Gaussian Line Fit . . . . .	126
10.1.4	Fitting Parameter Analysis . . . . .	129
10.2	Observation of aurora due to cusp precipitation during northward IMF . . . . .	133
10.3	Observations . . . . .	134
10.3.1	HiTIES . . . . .	134
10.3.2	IMAGE . . . . .	134
10.3.3	ESR Observations . . . . .	139

10.3.4 The IMF . . . . .	139
10.4 Analysis and Discussion . . . . .	140
<b>11 Conclusion</b>	<b>144</b>
11.1 Sunlight Subtraction . . . . .	144
11.2 Ground Based Observation of the High Latitude Cusp . . . . .	144
11.3 Proton Aurora Observation . . . . .	145
11.4 Geocorona Study . . . . .	145
11.5 Further Work . . . . .	145

UNIVERSITY OF SOUTHAMPTON

ABSTRACT

FACULTY OF SCIENCE

SCHOOL of PHYSICS & ASTRONOMY

Doctor of Philosophy

THE CHARACTERISATION OF THE HIGH THROUGHPUT IMAGING ECHELLE SPECTROGRAPH AND INVESTIGATIONS OF HYDROGEN BALMER  $\beta$  EMISSION OVER SVALBARD.

by Stuart Charles Robertson

This thesis details the calibration of the High Throughput Imaging Echelle Spectrograph and observations of hydrogen Balmer  $\beta$  emission made with it from Svalbard. It presents calibration tools and instrumental artifact removal techniques. It introduces innovative techniques for removing sunlight and line contamination from spectral data.

An investigation of the hydrogen Balmer  $\beta$  emission due to a dayside auroral event on November 26<sup>th</sup> 2000 and a detection of cusp aurora over Svalbard on November 27<sup>th</sup> are presented. Evidence is presented for red shifted auroral protons in dayside aurora and the hydrogen  $\beta$  emission profile is shown to provide a range of information on the velocity distribution and origin of precipitating particles.

Geocoronal and atmospheric hydrogen  $\beta$  emission over Svalbard is investigated. Geocoronal emission is found to be omnipresent and to have an emission inertia of approximately 4 hours. Evidence for unshifted hydrogen line emission response to auroral precipitation is presented.





### **Acknowledgements**

First of all, thank you to my long suffering supervisor Betty Lanchester, without whom none of this work would have been possible. Special thanks to Nikita Shumilov for all his help and support with my practical work at Nordlysstasjonen, and Alan Aylward for his recent support. I would also like to thank Fred Rees, Ian Furniss, Ian McWhirter, Dirk Lummerzheim, Mike Hill, Mike Lockwood, Hermann Opgenoorth, Mats André, The Marie Curie scholarship, Mykola Ivchenko, Trond Trondsen, Scott Smedley, Steve Barrington and Claudio Marengo for all the help you have given to me. I would like to add a big thank you, lots of love, and all the best for the future to my ex-fiancee, Eva Boralv, a unique woman who has been very supportive throughout my extended period of writing up.

This book is dedicated to my parents Elizabeth Jane Robertson and Brian John Michael  
Robertson.

# Chapter 1

## Introduction

In 1619 Galileo Galilei produced a thesis called 'Discorso Delle Comete' [Guiducci et al. (1619)]. It was published under the name of one of his students Mario Guiducci to avoid direct violation of the Spanish Inquisition edict he was under at the time. This thesis contradicted the Caelestis Sphaerae [Ptolemy (2)] model of a Geocentric universe, and instead supported an alternate hypothesis that Earth orbited the Sun [Copernicus (1514)]. One of the propositions of this heretical thesis was that aurora is reflected sunlight. Although the phenomenon was later proved to result from precipitating particles [Vegard (1948)], it is still named for Aurora, Roman Goddess of the Morning and Herald of the Sun.

### 1.1 Investigation of Hydrogen Aurora

Spectral investigation of auroral phenomena began with Ångström in 1869. It wasn't until Vegard (1948) proved that the auroral phenomena contained hydrogen moving at a high velocity toward the earth. This theory was consolidated by earlier observations [Vegard (1938)] and by subsequent observations [Gartlein (1951); Meinel (1951)] of the Doppler shifted hydrogen Balmer emission line from auroral forms. Gartlein also confirmed the presence and proportion of the Balmer series at  $\alpha$  at 6563 Å,  $\beta$  at 4861 Å and  $\gamma$  at 4340 Å emission. Meinel estimated the peak was Doppler shifted by around 8 Å, corresponding to an average Earthward particle velocity of 500 km/s at the magnetic zenith. The observation also displayed no peak shift from the magnetic horizon, indicating that the emitting particles were propagating from somewhere near the magnetic zenith. Further study found this auroral hydrogen emission to originate from

extraterrestrial protons that had captured an electron during precipitation into the upper atmosphere [Eather (1967)].

### 1.1.1 Dayside Merging between the IMF and Geomagnetosphere

These protons form the main part of the solar wind, the constant particle flux emerging from the Sun [Gloeckler and Geiss (1989)]. The solar wind, also containing alpha particles, electrons and trace metals, flows out from the Sun with the interplanetary magnetic field (IMF). The IMF flux lines merge with the Earth's magnetospheric flux lines in a process known as reconnection, first described by Dungey (1953) and later reviewed in Cowley (1982). Merging between the IMF and the Earth's magnetospheric field occurs between anti-parallel field lines and results in field lines that extend from the surface of the planet out into interplanetary space. Different IMF-magnetosphere orientations result in correspondingly different merging points on the magnetopause. Crooker (1982) presents the various merging geometries for northward (parallel field lines) and southward (anti-parallel field lines) IMF. Figure 1.1 displays the anti-parallel merging process between southward IMF and the closed field lines of the sunward geomagnetosphere. This process generates lines of geomagnetospheric flux open to space symmetrically in both the north and south hemispheres. Parallel merging occurs between the northward IMF and previously opened lines of the geomagnetosphere, anti-sunward of the poles. This scheme, shown in figure 1.2, requires previously opened magnetic field lines. The process generates open lines of magnetic flux over just one of the poles. Again, the merging process allows the solar wind particles to enter the Earth's magnetic field, guiding them along the open field lines over one of the Earth's polar regions. Technically it is possible for the IMF to connect with the same field line at both poles resulting in closed field lines. Practically this lobe reconnection process produces asymmetric reconnection, in one of the hemispheres. The merging process gives the solar wind particles access to the Earth's magnetic field, funnelling them down the open field lines and often into the atmosphere over the Earth's polar regions.

The cusp is that region of the dayside magnetosphere through which precipitating particles gain direct entry to the atmosphere along newly reconnected field lines [Smith and Lockwood (1996)]. These newly connected field lines guide the precipitating particles down into the Earth's atmosphere where they collide with particles of the atmosphere, exciting auroral photon emission. The

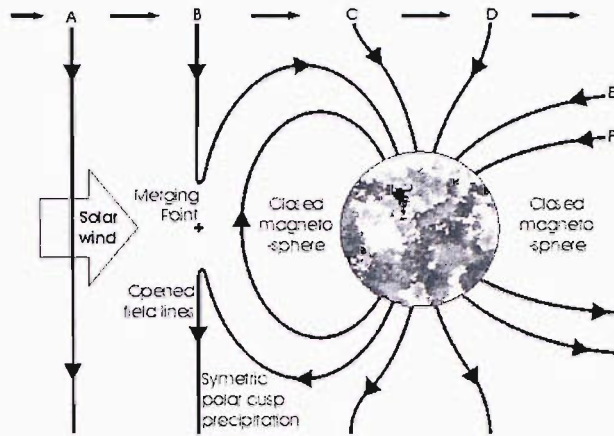


Figure 1.1: The geometry of reconnection between a southward IMF and the geomagnetosphere. The cusp occurs where the newly opened field line (B) touches the Earth. This occurs symmetrically in both hemispheres.

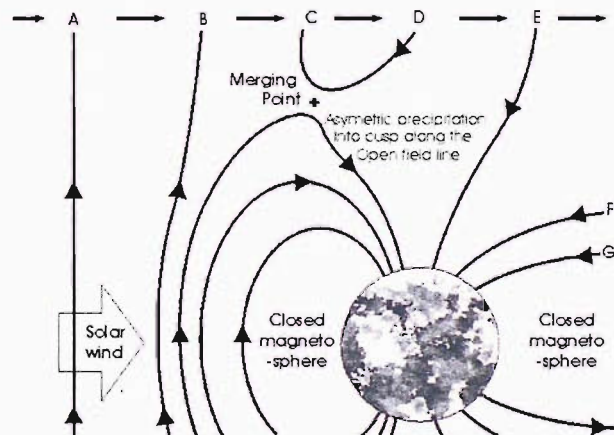


Figure 1.2: The geometry of cusp reconnection with northward IMF. Field line C has reconnected with field line D at the marked merging point to create the configuration shown over the northern hemisphere. The cusp is located where the field line below the merging point touches the Earth, slightly northward of the Southward IMF cusp.

protons precipitating in the cusp have a typical energy of 2 keV [Hardy et al. (1989)] and result in doppler shifted hydrogen emission. The cusp particle entry region due to dayside reconnection, was first defined in a large statistical data survey of DMSP data [Newell and Meng (1994)]. Newell and Meng showed that the southward IMF cusp could occur many hours from local noon in the dawn and dusk sectors of the dayside magnetosphere. A survey [Frey et al. (2002)] of Imager for Magnetopause-to-Aurora Global Exploration (IMAGE) data presented a statistical analysis of the cusp position for all orientations of the IMF. The survey used a region or spot of Ly- $\alpha$  proton emission as a tracer for the cusp. This emission was measured by the S12 instrument on the IMAGE satellite, described by the same article and references therein. The study shows that the cusp position is strongly dependent on the IMF direction. The longitudinal position of the cusp is dictated by the IMF  $B_y$  (GSM) component. The latitudinal position of the cusp is affected by the north-south orientation of the IMF, the pressure of the solar wind, and the phase of the substorm cycle. Phan (2003) showed that a discrete dayside proton auroral spot at auroral altitudes, signifies magnetopause reconnection with a northward IMF. A negative  $B_y$  component moves the cusp toward the dawn sector and conversely a positive  $B_y$  moves the cusp into the dusk sector [Pitout (2002)]. Frey reported that the limits of the cusp occurrence are  $70.8^\circ\text{MLat}$  to  $85.6^\circ\text{MLat}$  (magnetic latitude) and 6.6 MLT and 16.0 MLT (magnetic local time). Measurements have shown that it can extend over 2.5 hours of MLT but it is limited to a single degree of latitude [Oulu Space Physics Textbook]. The optical signature of this cusp aurora during northward and southward IMF, is one of the primary interests of this thesis.

## 1.2 Investigation of Auroral Proton Precipitation over Svalbard

### 1.2.1 The Geographic Location of Nordlysstasjonen

The optical data described here are from Nordlysstasjonen or ‘The Northern lights station’ located at  $78.2^\circ\text{N}$  and  $15.8^\circ\text{E}$ . The observatory is situated in Adventdalen, near the EISCAT Svalbard Radar (ESR) facility. The ESR has two incoherent scatter radar antennae, one 42m wide and aligned along the median magnetic zenith, the other is a 32m dish mounted on an azimuth and elevation agile base. The proximity of the ESR was a large factor in locating the HiTIES platform, and many ESR support campaigns have resulted from this arrangement. No radar data are presented in this thesis.

Figure 1.3 is the solar zenith angle at noon and midnight at Nordlysstasjonen, showing the daily

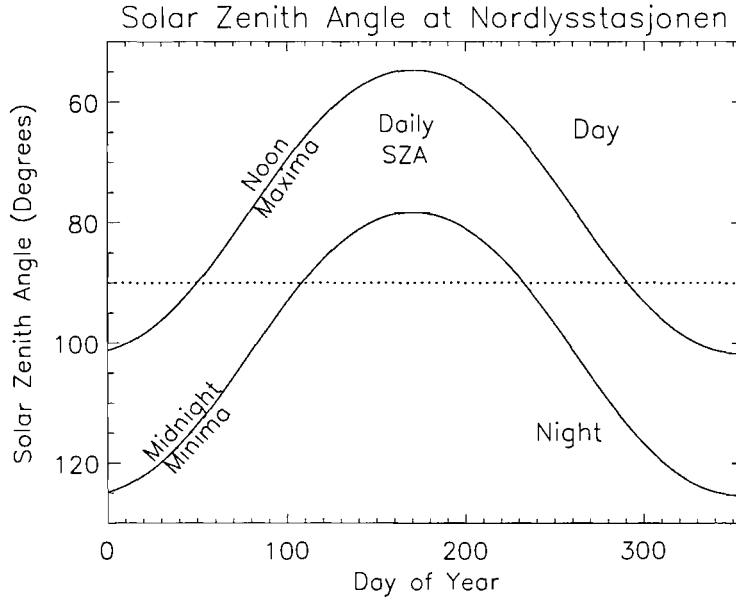


Figure 1.3: The solar zenith angle (SZA) at Nordlysstasjonen over a year. The upper curve represents the SZA at noon (10:57UT) while the lower curve represents the SZA at midnight. The horizon is represented by the horizontal dotted line.

period of direct sunlight or night over the year. The solar zenith angle is the angle subtending the local zenith, and the Sun-Earth line. A solar zenith angle of  $>90^\circ$  indicates the sun is below the horizon. Chapter 8 presents an analysis of Sunlight on Svalbard: see figure 8.1 for a more detailed description of this geometry.

The Sun is below the horizon between 27 October and 15 February, although Rayleigh scattered sunlight illuminates the sky over Svalbard for several hours around midday. Therefore, arctic night is considered to last from 14 November to 29 January, a period when the Sun rises no higher than  $6^\circ$  below the horizon. Even during this time, the twilight contamination around local noon can be up to three orders of magnitude brighter than proton aurora emission.

### 1.2.2 The Geomagnetic Location of Nordlysstasjonen, Svalbard

Nordlysstasjonen is located at a geomagnetic latitude of  $75^\circ\text{N}$  MLat. During the day, this is typically north of the auroral oval, and on the southern edge of the magnetic cusp. It is thus possible to observe many kinds of aurora from Svalbard. Figure 9 from Frey et al. (2002)

indicates that around 5% of the IMAGE observed cusp positions were at  $75 \pm 0.5^\circ \text{MLat}$ . Study of the cusp is possible from Svalbard, particularly if the effects of scattered sunlight contamination are reduced.

### 1.2.3 Observing the dayside aurora from Svalbard

During arctic night, optical aurora can be observed from Nordlysstasjonen during the day with minimal sunlight interference. The first dayside measurement of proton aurora was performed by Henriksen (1985). Henriksen presents measurements made from Longyearbyen and ascribed to proton auroral emission from the polar cleft. Almost a decade later Sigernes presented high resolution spectral observations of Doppler shifted auroral hydrogen emission measured from Svalbard in order to evaluate a model of proton precipitation [Sigernes et al. (1993); Sigernes et al. (1994)]. Lorentzen et al. (1998) developed this model and presented further measurements of the Doppler shifted auroral hydrogen profile of dayside cusp precipitation over Svalbard. Most recently Lanchester [Lanchester et al. (2002); Lanchester et al. (2003)] presented measurements of auroral hydrogen Balmer  $\beta$  emission ( $H\beta$ ) from dayside cusp precipitation due to an intensification in the solar wind. These papers present detailed spectral and temporal analysis of proton emission from the cusp during southward IMF, some of which is presented later in this thesis.

## 1.3 Instrumentation used to investigate Hydrogen Aurora

The first auroral observations were carried out using photographic plates. Once photoelectric detectors [Geitel and Elster (1893)] reached a suitable state of maturity, they were utilised by Hunten (1955) and Montalbetti (1959) in spectrophotometers, improving the signal to noise and temporal resolution of auroral measurements at the time. Unfortunately the spectrometer is poorly suited to low light spectrometry as the slit entrance aperture provides very little collection area for incident auroral photons. Omholt (1957) built a photoelectric detector with a  $10 \text{ \AA}$  filter to select the hydrogen bandpass. This instrument provided higher signal and temporal resolution than anything that had come before it, mostly due to its relatively large filter collection area. Early filter lenses did not completely suppress the wavelengths outside the desired bandpass and the transmission of the filter pass band itself was not very efficient. To combat this and make sense of this data, the output of a second photometer measuring the



spectral background was subtracted from the primary photometer to reveal the desired signal. Improvements in filters and the use of the tilting filter technique, resulted in high signal to noise measurements of the hydrogen Doppler profile to a few Å [Eather and Jacka (1966)].

The development of the Fastie-Elbert (F-E) scanning spectrometer provided the auroral spectrometry tool of choice until recent years. This spectrometer design maximises the optical throughput. However, the scanning process constitutes an integration of each spectral element and measurement of the entire hydrogen profile stretched over 30-40 Å with a reasonable spectral resolution takes several minutes. Thus a (F-E) spectrometer provides either high spectral resolution or high temporal resolution [Sigernes et al. (1994), Lorentzen et al. (1998)].

The advent of CCD detectors allows the imaging of an entire spectral line in one integration, although the slit limits measurement in the low light regime. The electronic detectors of today rival the photographic plate for sensitivity and they offer an unprecedented combination of speed, resolution and usability. The CCD detector can be amplified for operation in the low light regime although there is a trade off in noise and intensity scale linearity [Trondsen (1996)]. CCD detector instruments are currently the tool of choice for investigating auroral emissions. The High Throughput Imaging Echelle Spectrograph (HiTIES) [Chakrabarti et al. (2001)] is one such instrument used to investigate auroral phenomena from Svalbard [Lanchester et al. (2002): Lanchester et al. (2003)]. This thesis discusses the characterisation and initial measurements of HiTIES on Svalbard.

## 1.4 Other Observed Phenomena

### 1.4.1 The Hydrogen Geocorona

Spectral emission from exospheric hydrogen was first measured during the International Geophysical Year 1957. At Zvenigorod, USSR, Krassovsky and Galperin (1958) measured hydrogen Balmer  $\alpha$  emission and concluded it was primarily of Earth origin. From this work Sheglov (1963) concluded that the daily maximum occurred in the early morning hours, and later work by Kerr (1986) placed the maximum between 02:00-06:00LT. Shih et al. (1985) further refined the time of this maxima to around 04:00LT. All of these observations were made from a latitude experiencing diurnal sunlight illumination and normalised for shadow height. A six year survey [Fishikova and Marzvaladze (1966)] from Abustuani Observatory near solar maximum reported

the brightness of this phenomena to vary between 9 and 16 Rayleighs. A seasonal variation was reported in the Northern hemisphere [Tinsley (1974)] with the H $\alpha$  maximum in January and a second smaller maximum during the summer months.

The hydrogen geocorona is comprised of hydrogen atoms on ballistic, satellite and hyperbolic trajectories in the Earth's exosphere. The exosphere is generally considered to lie within the altitude range of 500 km and extends out into space. Meriwether et al. (1980) showed that the distortion of the geocoronal hydrogen emission curve, moving from a Maxwellian thermal distribution to a non-Maxwellian distribution, decreased the line width with increasing shadow height.

### 1.4.2 Coronal Mass Ejection

During active times, the Sun can eject billions of tonnes of solar material from the corona. These coronal mass ejections (CMEs) are potentially the most energetic events in the solar system. These violent events, reviewed by Wagner (1984), frequently accompanied by a solar flare, accelerate the ejected mass, or plasmoid, out of the solar system at supersonic speeds. The supersonic plasma pushes the solar wind, creating a dense bow shock of solar wind plasma before it. Any ejection of mass at supersonic speed creates these shocks observed in the solar wind. Very occasionally one of these CMEs will collide with the Earth's Magnetosphere. When this happens, a vast amount of energy is injected into the magnetosphere through compression, particle precipitation and friction, resulting in massive geomagnetic activity and auroral emission. These are 'halo' CMEs, so called for their appearance around the Sun from Earth as they approach.

### 1.4.3 Cosmic Rays

Cosmic rays are highly energetic particles first proved to be of extra-terrestrial origin by Victor Hess in 1912. This constant flux of extra-terrestrial particles are mostly protons, but also consist of high energy  $\alpha$  particles, heavier ions, electrons, photons and neutrinos [Groom et al. (2000)]. The cosmic rays interacting with atmospheric particles give rise to a number of secondary products, often with high energies. These in turn interact with atmospheric particles to produce a cascade of particles, or air shower, through the atmosphere. These secondary particles can interact with the silicon substrate used in the HiTIES CCD detector. These cosmic ray events (CRE)

are usually observed as an elevated count on just one pixel. This phenomenon is investigated more thoroughly in section 8.2.

## 1.5 Synopsis

This thesis can be considered to have two broad components, technical work and scientific research, the latter being based on the former. Chapter 2 describes the physics of proton aurora. The technical aspects of using a mosaic filtered echelle spectrograph are described in chapter three. Chapters 4, 5 and 6 present the characterisation and calibration of the spectrograph. Chapters 7 and 8 contain the software tools and algorithms required to analyse HiTIES data, including a technique for removing sunlight contamination from auroral data. The final three chapters contain the research which uses the first eight chapters. Chapter 9 presents an investigation into unshifted  $H\beta$  hydrogen emission from the atmosphere. Chapter 10 holds two studies of auroral proton precipitation in the cusp. The first is an event study during a southward IMF shock event, the second is a study of proton aurora during a period of sunlight contamination and northward IMF near magnetic noon. The last chapter is the conclusion.

## Chapter 2

# Theory of Dayside Proton Aurora

Protons are the dominant positively charged constituent of the solar wind, making up approximately 95% of the positive particles. Alpha particles (4%) and heavier ions (1%) make up the remainder [Gloeckler and Geiss (1989)]. The Earth's magnetosphere is coupled to the interplanetary magnetic field (IMF) via the process of reconnection [Dungey (1953); Cowley (1982)]. Reconnection on the dayside can take several forms, described in the introduction. These reconnected field lines provide the solar wind particles carried with the IMF a point of entry into the Earth's magnetosphere. The primary energy carrier is the electron [Galand et al. (2001)], while protons carry about 15% of the total energy. The average energy of the protons precipitating on the dayside varies between 0.1 keV to 2 keV for different latitudes and local times. The latter value is the average energy of cusp protons [Hardy et al. (1989); Hardy et al. (1991)]

Entry into the upper atmosphere changes the behavior of the magnetically bound stream of positively charged particles. The scattering characteristics of precipitating electron and proton streams are very different. The low mass of the electron means it often suffers large angle deflection during atmospheric interactions. However, the higher mass proton suffers very little deflection during its passage through, and interaction with, the atmosphere. Thus the proton is able to penetrate deeply into the atmosphere even though on average, it has less energy. Equation 2.1 to 2.3 [Rees (1989)] show the three possible interactions between protons and atmospheric particles ( $M$ ).

Proton Ionisation:



Proton Excitation:



Charge Capture:



Where the '\*' symbol indicates the atom is excited. In equation 2.3 the proton captures an electron in its orbit and becomes hydrogen. This newly formed hydrogen atom is still precipitating with auroral velocities, but behaves very differently from the precipitating proton. The precipitating hydrogen atom is subject to the following reactions.

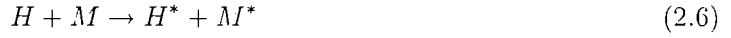
Charge Loss:



Double Ionisation:



Hydrogen Excitation:



The collision processes described by equations 2.1 to 2.6 excite or ionise the atmospheric particle ( $M$ ). This energy deposition is identical to that caused by some electron precipitation and results in the same auroral emissions. The brightness of these atmospheric emissions can reach several kiloRayleighs [Dashkevich et al. (1996)] and they are spectrally indistinguishable from electron aurora.

When the precipitating proton undergoes the charge capture process 2.3, the resulting particle gains two important qualities: the particle can now emit photons and is electrically neutral. The newly formed precipitating hydrogen atom is now unconstrained by the magnetic flux lines which bound the proton. The resulting trajectory of precipitating protons as they undergo collision processes 2.3 and 2.4 again and again is shown in diagram 2.1.

The spiral motion shown in figure 2.1 is due to the action of the Lorentz force. The velocity of the particle is represented by two vectors, the velocity parallel to the field line ( $\underline{v}_{\parallel}$ ) and the velocity perpendicular to the field line ( $\underline{v}_{\perp}$ ). The Lorentz force is described by equation 2.7.

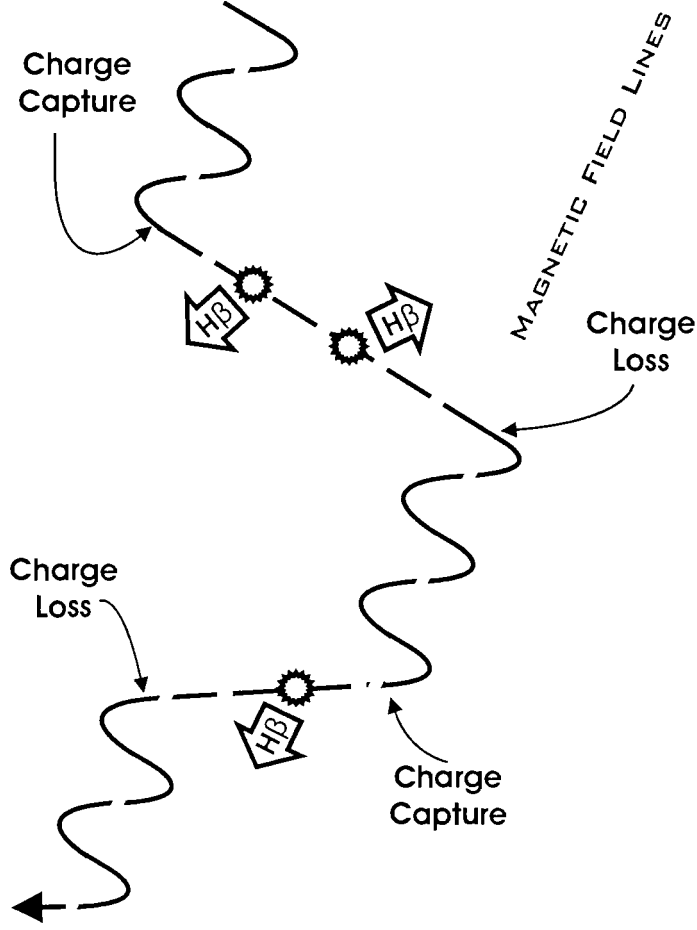


Figure 2.1: A schematic plot of the trajectory of a precipitating proton and  $H\beta$  emission. The diagonal white lines represent the field lines along which the protons travel. Solid black lines represent the proton trajectory. Precipitating hydrogen is represented by broken lines. The star symbol and  $H\beta$  arrow represent a  $H\beta$  emission event.

$$F = q\underline{v}_{\perp} \times \underline{B} + e\underline{E} \quad (2.7)$$

where  $q$  is the particle charge,  $\underline{B}$  is the magnetic field vector,  $e$  is electron charge and  $\underline{E}$  the electric field vector. For zero electric field, The particle is bent into circular gyration around the field line by the  $\underline{v}_{\perp} \times \underline{B}$  Lorentz force. Thus the proton trajectory takes the form of a spiral shown figure 2.1, moving along the field line with a velocity of  $\underline{v}_{\parallel}$ , rotating with a radius  $r_g$ , defined by equation 2.8.

$$r_g = \frac{mv_{\perp}}{qB} \quad (2.8)$$

at a frequency of  $\omega_g$ , defined by equation 2.9.

$$\omega_g = \frac{v_{\perp}}{r_g} \quad (2.9)$$

The particle executes this motion only while it is ionised. Once the precipitating particle achieves charge neutrality it is free from the effects of the magnetic and electric field. The hydrogen atom moves with velocity of magnitude  $v_H$ , as defined by the equation 2.10,

$$v_H = \sqrt{v_{\perp}^2 + v_{\parallel}^2} \quad (2.10)$$

Equations 2.6 and 2.3 both produce excited hydrogen. This excitation and associated emission form a spectrally unique auroral emission. Depending on the amount of excitation, these excited hydrogen atoms will emit photons from the Lyman, Balmer, Paschen, Brackett, Pfund and Humphreys series [Rees (1989)]. From the ground we only observe the Balmer series as atmospheric nitrogen oxide effectively absorbs the Lyman series and atmospheric water absorbs all of the Paschen and lower emission series. The first three lines of the Balmer series are  $\alpha$  at  $6563\text{\AA}$ ,  $\beta$  at  $4861\text{\AA}$  and  $\gamma$  at  $4340\text{\AA}$ . These were all observed by HiTIES during the solar eclipse in Cornwall, 1999. The relative intensities or line decrements between  $H\alpha:H\beta:H\gamma$  are not exactly known. Empirically auroral measurements show  $H\alpha$  is roughly three times stronger than  $H\beta$  [priv. comm., Fred Rees]. However, this bright line is contaminated by an auroral emission from  $N_2(1P)$  [Galand et al. (2001)], which interferes with measuring the shape of the  $H\alpha$  doppler profile. To avoid the complexities and inaccuracies introduced by removing this nitrogen emission,  $H\beta$ , or  $H\gamma$  is used to detect proton aurora with HiTIES. The profile is Doppler broadened by the line of sight velocity ( $v_{\parallel}$  assuming we view along the field line) and is unrelated to any emission. The temperature broadened line profile is unlike the doppler broadened hydrogen aurora. Thus it can be seen that proton precipitation is detectable through a unique airglow emission.

An example of a Doppler shifted  $H\beta$  profile, peaking at  $4859.5\text{\AA}$ , is displayed in figure 2.2. This is a Doppler shift of  $1.8\text{\AA}$  from the unshifted  $H\beta$  line emission at  $4861.3\text{\AA}$ . This Doppler shift is due to the velocity of the emitting particle along the line of sight between the particle and the

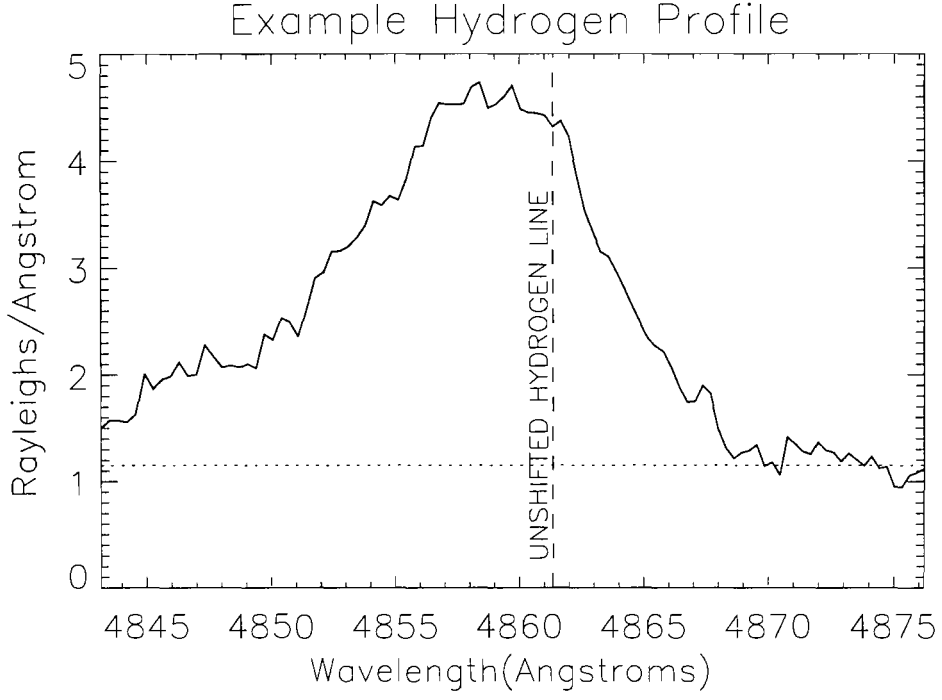


Figure 2.2: An example auroral hydrogen spectrum. This spectrum was acquired from the HiTIES spectrograph during a sixty second exposure. The data is dark subtracted, flat fielded and cosmic ray filtered. This spectrum was integrated from four degrees of elevation centered on the magnetic zenith.

observer. Equation 2.11 describes this Doppler shift.

$$\lambda' = \lambda \left(1 - \frac{v}{c}\right) \quad (2.11)$$

where  $\lambda'$  represents the Doppler shifted wavelength of the  $H\beta$  emission and  $\lambda$  the unshifted emission line wavelength, both of which are in the operating wavelength unit. The velocity of the hydrogen atom along the line of sight between the atom and the observer is  $v$  and  $c$  represents the speed of light. For the usual case of the observer viewing the aurora along the magnetic zenith,  $v = v_{\parallel}$ . Rearranging this equation to find the velocity of the particles causing the doppler shifted wavelength emission.

$$v_{\parallel} = c \left(1 - \frac{\lambda'}{\lambda}\right) \quad (2.12)$$



Using equation 2.12, the profile in figure 2.2 is re-plotted with the wavelength axis translated into a velocity axis in figure 2.3. The graph describes the velocity of the emitting hydrogen atoms along the observer's line of sight with positive defined as toward the observer.

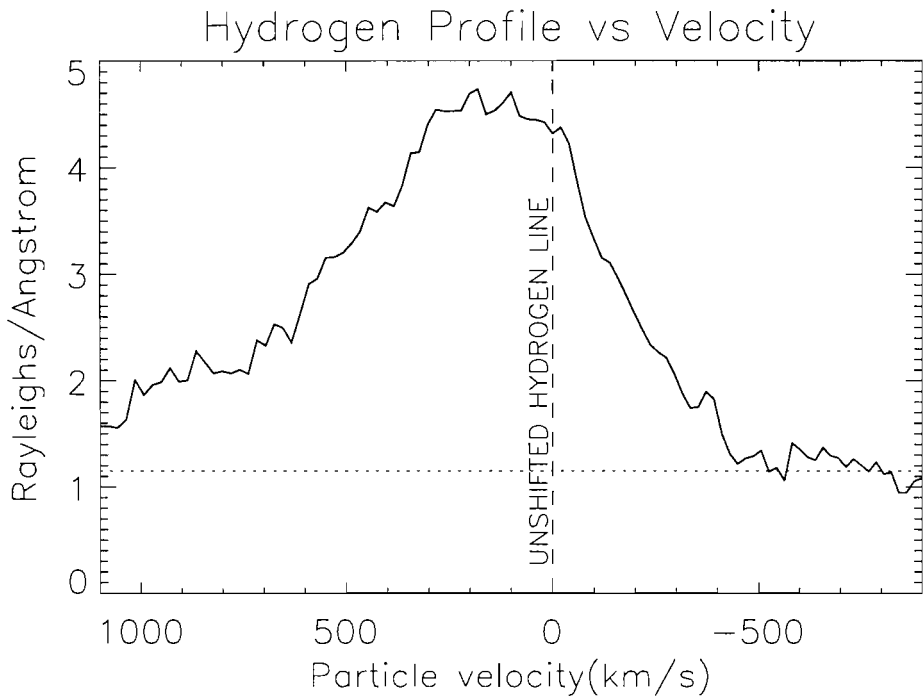


Figure 2.3: Example Doppler shifted H $\beta$  profile using equation 2.12 to re-plot the wavelength axis as the velocity of the emitting particle along the observer's line of sight. Positive is toward the observer.

The particles emitting the profile are diffusing away from the magnetic field lines. Each precipitating particle undergoes numerous charge exchange collisions. This results in the particle population as a whole diverging away from the source flux tubes while neutral, in a random-walk process. This diffusion process is characteristic of proton aurora resulting in emission over large areas of sky. The extent of dayside proton arcs can be of the order of several degrees of latitude; covering a large percentage of the sky with weak Doppler shifted hydrogen emission.

At high energies the proton/hydrogen precipitation exists mainly as protons, at lower energies hydrogen dominates. The peak height of proton aurora emission is a function of energy, however the height of maximum emission can be assumed to occur at around 120 km see [Eather (1970)]. The physics of this energy deposition as a function of height are modelled and described by

[Basu et al. (2001)]. Once the particle energies have been quenched by the atmosphere, the recombined protons merge with the ambient atmospheric hydrogen.

## Chapter 3

# HiTIES: the High Throughput Imaging Echelle Spectrograph

This chapter discusses the design considerations and description of the HiTIES spectrograph. The High Throughput Imaging Echelle Spectrograph (HiTIES) is an instrument designed for making optical observations of airglow in the Earth's atmosphere. The Southampton-UCL HiTIES is one of a series of similar spectrographs constructed by Boston University and described in Chakrabarti et al. (2001). The instrument species is unique in airglow aeronomy, recording high resolution spectrographic data along a spatial dimension. It has a high spectral resolution due to the use of a high order echelle diffraction grating. This grating, in combination with a mosaic filter arrangement, provides around 100 Å of spectrographic data. The range of the recorded spectrum is broken up into selected bands through selection of interference filters of chosen wavelength regions. The spectrograph was mounted on a steady, variable elevation platform with an ICCD video camera and two photometers. This platform holds all of the instrument sensors, the cryogenic and computer support units are attached to these instruments by various required cables and tubes.

The platform of instruments were assembled at the Atmospheric Physics Laboratory at UCL as part of the collaboration between the University of Southampton and University College London. The nomenclature adopted in this thesis to denote the High Throughput Imaging Echelle Spectrograph is simply the spectrograph, while the term 'platform' is used for the spectrograph, auxiliary instrumentation and support units.

## 3.1 Spectrograph Components

### 3.2 The Echelle Grating

The defining element of a spectrograph is its diffraction grating. The choice of diffraction grating dictates the operation of the spectrograph and is selected with the desired spectral output in mind. The operation of all of these diffraction gratings is explained by the grating equation in equation 3.1.

$$\frac{m\lambda}{D} = \sin(\theta) + \sin(\psi) \quad (3.1)$$

where ' $m$ ' is the diffraction order, ' $\lambda$ ' is the operating wavelength in the operating unit, ' $D$ ' is the line spacing in mm, ' $\theta$ ' is the incident angle and ' $\psi$ ' is the exit angle. These terms are all described graphically in figure 3.1.

Conventional spectrographs use densely lined, precision engineered gratings with 1000+ lines/mm to resolve the first few diffraction orders and achieve high resolution (eg/  $m=2$  and  $D=1/1000$ ). Echelle spectroscopy [Baranne et al. (1972)] targets high diffraction orders however, utilising gratings with low line densities of around 50 lines/mm (eg/  $m=40$  and  $D=1/50$ ) to achieve high resolution. It can be readily seen from equation 3.1 that for a fixed wavelength, the diffraction produced by the example figures for  $m$  and  $D$  are equivalent.

When light diffracts from a conventional grating, the first diffraction order gets around 90% of the diffracted power. The power transmitted into each increasing diffraction order decreases dramatically with order number, resulting in almost nothing being transmitted into the higher orders. To alter this situation for echelle spectroscopy, the diffracting face of the grating is angled away from the grating normal to reflect light along a pre-chosen direction. Altering the face or 'blaze' angle of a grating effectively alters the angle of the normal about which the power is reflected. This transmitted power diversion does not affect the positions of the diffraction orders, it simply moves the power vector into the orders of diffraction around the diverted angle. In fact the diffracted power tends toward maximum as  $\psi \rightarrow \phi$  [Meaburn (1939)], where  $\psi$  is the diffraction angle and  $\phi$  is the blaze angle. Figure 3.1 displays both these angles, conventionally measuring them and the others from the grating normal (N).

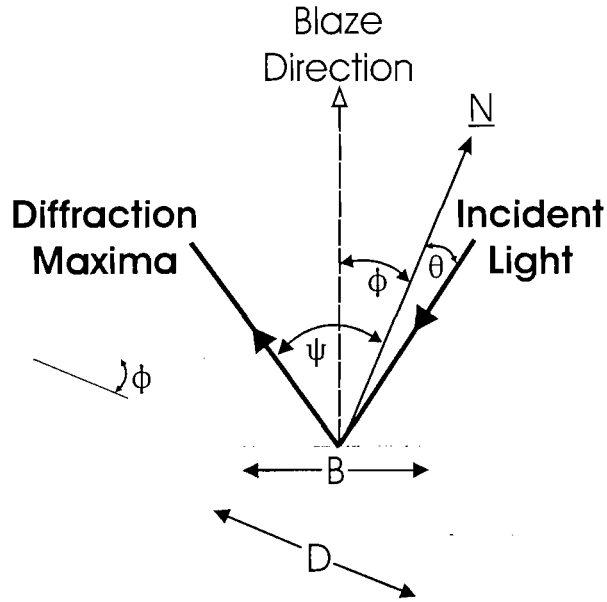


Figure 3.1: Displays the diffraction geometry from an Echelle grating.  $N$  denotes the grating normal.

The use of high diffraction orders introduces an acute problem of diffraction order overlap. Each order diffracts a different wavelength onto the same diffraction angle. The wavelength of each order can be calculated by rearranging equation 3.1 for  $\lambda$ , shown in equation 3.2.

$$\lambda = \frac{\sin(\theta) + \sin(\psi)}{gm} \quad (3.2)$$

where  $g$  is the line density given by,

$$\varrho = \frac{1}{D} \quad (3.3)$$

For a fixed spectrograph grating,  $\theta$  and  $\varrho$  are constant and  $\psi$  represents a limited range of diffraction angles that are focused on the spectrograph sensor. For a given order, this range of recorded wavelength is a function of the range of  $\psi$  focused on the recording sensor. This can be seen from equation 3.2 and it is likewise clear that each separate order has a different range of wavelengths diffracting onto the sensor. These diffraction order wavelength ranges are described in figure 3.2. Considering these ranges together, the wavelength coverage is excellent across the visible wavelengths. Sizable gaps appear in the spectral coverage toward the red of the spectrum. If these gaps occur in areas that require spectral coverage, the angle of grating can be altered to change both the incident and diffraction angle of incident light on it. From equation 3.2, it can be seen that changing  $\theta$  and  $\psi$ , the diffracted wavelength will change, resulting in the movement of all the diffracted orders shown in figure 3.2.

152x286 160x295

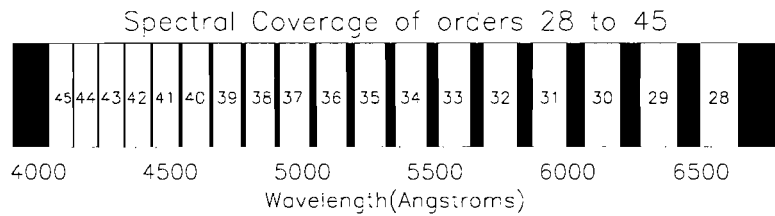


Figure 3.2: Displays an example of the spectral coverage of the echelle diffraction orders 28 through to 45 for the HiTIES. Each number represents a diffraction order and the white area beneath represents the imaged spectral range of that order on the wavelength axis at the bottom. This figure was compiled from the data in table 5.3.1.

The spectra from each order of diffraction are superimposed upon one another at the sensor. Separation of the target spectra from the rest of the spectral coverage is achieved through interference filters. Interference filters efficiently absorb every wavelength bar a specific range decided during the filter construction. The filter range required to admit a good fraction of an order on the CCD is around 50 Å. Placing a filter of this kind into the spectrograph optical path creates a filtered area on the sensor containing just the wavelength of a single diffraction order. Through appropriate positioning of both the grating and filter, the target spectral line

is brought within the filter on the CCD. This feature/filter arrangement is repeated for each of the other target features, carefully positioning each feature/filter on the sensor. Once all of the desired features/filters are positioned in a mutually exclusive way, this 'mosaic' of discrete filters can be fixed in the optical axis. The mosaic will now transmit only the desired spectrum of discrete spectra dictated by the grating position and filter arrangement. Figure 3.3 shows an example 'mosaic of filters' and the selected target wavelength spectra transmitted to the spectrograph sensor.

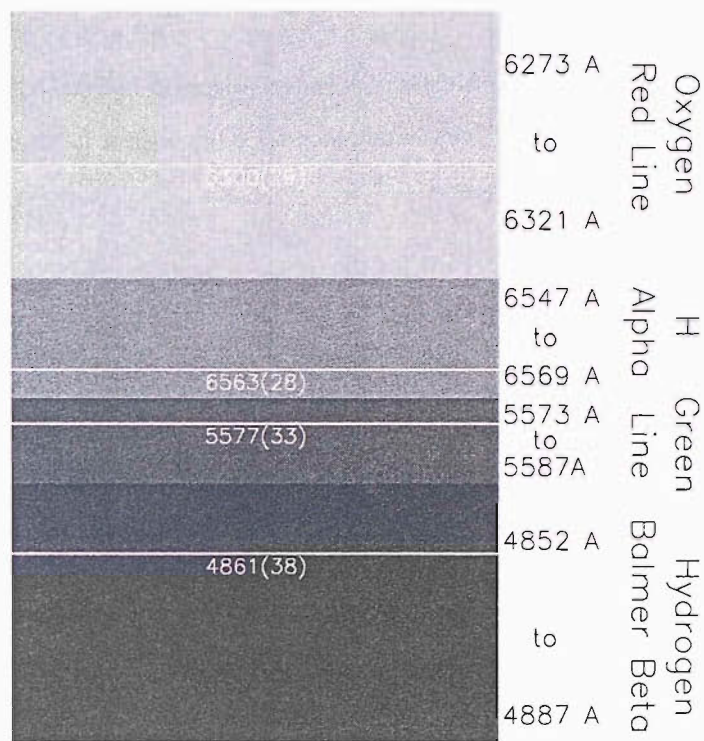


Figure 3.3: Model of the 4 filter wavelength selection mechanism of the echelle spectrograph. The area of the figure represents the detector, with wavelength on the vertical axis and a nominal horizontal spatial axis. The four coloured panels in the detector area represent different filters or non-consecutive wavelength bands. Each band is placed to capture a target spectral emission line, marked on the figure as a horizontal line with its respective wavelength in Ångströms and its diffraction order in brackets.

The efficiency of the Echelle grating is a function of wavelength, diffraction order, incident and diffraction angles. This efficiency is calculated from equation 3.4 [Chakrabarti et al. (2001)]

$$BlazeFunction = \frac{\sin^2 \gamma}{\gamma^2} \tag{3.4}$$

where,

$$\gamma = \frac{\pi D \cos \phi}{\lambda} (\sin \psi + \sin \phi) \quad (3.5)$$

Filter transmission varies with individual filters and with the spectral range of the filter. The introduction of filters in the optical path does however introduce a loss in transmission of the target features. The combination of Echelle grating and the interference filters accounts for a loss of around 80% of the target wavelength signal. Imperfections in the grating and filters further increase this loss, as does the use of diffraction angles away from the blaze angle. The sensitivity of the optical sensor must be considered carefully as the brightness of the emissions being observed is low.

### 3.3 The Aperture

The basic HiTIES aperture is a curved slit and a telescope unit. The lens is attached to the aperture through a standard commercial interface. This provides the ability to mount other lenses to accommodate changing field of view requirements.

The spectrograph optics introduce a pin cushion effect into the optical axis. The pincushion effect curls the edges of the image and to redress this effect, an opposing curve is introduced by the spectrograph slit aperture. The slit curve is a mirror image of that induced by the optics at the centre of the CCD chip when the grating is positioned at the mid point of its range. This modification to the spectrograph creates straight spectral lines on the centre of the CCD array.

### 3.4 The Sensor

The layout of the spectrograph is clearly displayed in figure 3.4. The position of the CCD detector is marked at the end of the optical path. The detector unit is attached to the spectrograph via an industry standard interface. The initial design of the spectrograph called for a high quality bare CCD. Due to malfunctions in the primary CCD, the HiTIES detector has at various times been replaced with an intensified CCD and the MIC, a photon counting detector described in [Fordham (1992)]. The MIC detector and data gained from it are not described herein.



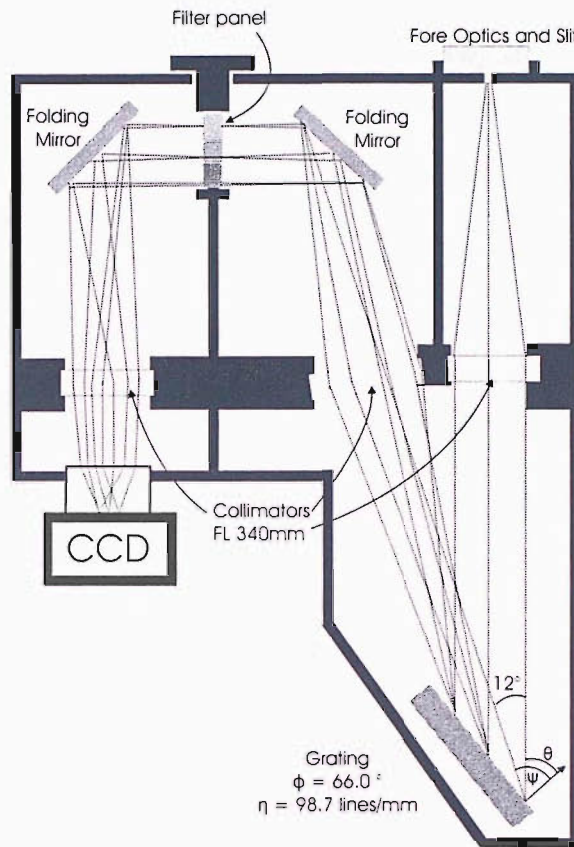


Figure 3.4: The layout and optical path of the High Throughput Imaging Echelle Spectrograph (HiTIES).

### 3.4.1 The Charge Coupled Device (CCD)

The sensor of choice in modern imaging applications is the CCD, invented in 1970 at Bell Laboratories [Janesic et al. (1989)]. CCD hardware requirements and data output are highly compatible with current demand in consumer electronics. As such, construction, and research and development of CCD technology is a mainstream commercial endeavor which produces even high end CCD technology at a reasonable price and availability.

The CCD detector unit is constructed from a silicon substrate on which an array of pixels and readout circuitry is deposited and etched. CCD detection is based on the silicon substrate

photosensitivity to visible wavelengths. The silicon lattice absorbs the energy from the photons, releasing free electrons into the lattice in the process. A photon with a wavelength over 3000 Å can produce one free electron [Janesic et al. (1989)] within the substrate. These free electrons are captured by the local potential wells created by the pixel array deposited on the silicon. The electrons can be 'read out' of the silicon lattice as a current through the superstrate circuitry and into the CCD readout buffer. The analogue current in each pixel in the buffer can be converted into counts in a digital array of pixels the same size as the CCD pixel array, and stored in computer media.

Some generalisations can be made in the use of CCD detectors in echelle spectroscopy. Firstly, the substrate temperature must be minimised to reduce the noise introduced through thermal vibration. Secondly, when using a bare CCD to study the faint light sources, the read out noise must be minimised to improve S/N. The third consideration is the quantum efficiency of photon detection (DQE). The efficiency and sensitivity vary between different CCD models and should be maximised. The most advanced CCDs are able to detect single photons with quantum efficiency of over 80%.

The initial configuration of HiTIES included a high quality, unintensified, megapixel CCD made by Pixelvision. This expensive CCD unit was selected for to its low noise, high pixelation, dynamic range and sensitivity in the spectral region of interest. As previously mentioned the CCD has been subject to complex malfunctions requiring replacement for varying lengths of time. In fact the primary sensor unit of the spectrograph was rarely available for calibration and the data described herein does not involve this sensor. However, several of the construction parameters of this CCD are known and can be stated with confidence.

### 3.4.2 Intensified CCD

Image intensification technology was developed by the military for night vision purposes. A conventional CCD intensifier takes the form of a photocathode, a micro-channel plate (MCP), a phosphor layer and a fibre optic coupling to the CCD pixel array. This arrangement, with the aid of a high voltage and vacuum in the MCP chamber can produce very high signal gain given by equation 3.6.

$$Gain_I = QE_I \cdot Gain_{MCP} \cdot V_I \cdot P_I \quad (3.6)$$

where  $QE_I$  is the quantum efficiency of the photocathode,  $Gain_{MCP}$  is the gain of the micro channel plate,  $V_I$  is the potential across the amplifier and  $P_I$  represents the efficiency with which Phosphor converts the electrons into light. From this equation the intensifier  $Gain_I$  ranges from a single order gain to a gain of almost five orders of magnitude for the new generation of intensifiers.

Although the signal gain introduced by the intensifier is large, the system also introduces new sources of noise. The thermal noise from the photocathode is similar to that of the CCD dark current. The thermal vibration releases electrons from the photocathode which in turn are amplified by the MCP to create a tangible source of noise dependent on the temperature of the photocathode. The gain of the MCP increases with  $V_I$  however so does the error in the potential across the MCP. These two sources of noise are far larger than any noise source originating in the CCD unit. Thus the important factors in using an intensified CCD to record data is keeping the temperature of the intensifier as cool as possible and balancing the signal gain with the amplification noise. Another practical factor to consider is that an intensified CCD has a potentially high temporal resolution. The useful dynamic range of an intensified CCD is much lower than that of an unintensified CCD. Thus, the benefits of introducing an intensifier into the sensor system must be considered carefully with respect to what exactly is being observed and what will be gained and lost by its introduction.

The first replacement sensor of HiTIES was an old second generation, intensified CCD with less than 0.1 megapixels. All of the data used for this thesis were gathered using this detector and it is using this sensor that most of the calibration was performed. The CCD chip itself holds a 256 by 384 matrix of pixels. The wavelength was dispersed along the long axis, leaving the short axis to measure spatial information.

The CCD unit has an air cooled cryogenic system that brings the Intensifier and CCD down to a working temperature of between 258°K and 263°K. At this temperature, one source of noise is several orders of magnitude larger than any of the other noise sources in the ICCD, rendering them largely inconsequential. The thermal vibration of the intensifier cathode frees electrons and these electrons are amplified by several orders of magnitude as they pass through the intensifier. This is the dominant source of noise in the ICCD.

### 3.5 Practical Instrument considerations

The practical issues of positioning, operating and supporting an auroral spectrograph are some of the most important issues facing a spectrograph project.

The instrument was moved between UCL, Cornwall, Tromsø and Svalbard. All of the data described in this thesis were taken from Svalbard which was chosen as a location due to proximity of the EISCAT Svalbard Radar and the presence of cusp aurora. Although ESR data has not been presented in this thesis, there have been several papers utilising the proximity of the radar and the platform of instruments; [Ivchenko et al. (2004a); Galand et al. (2004); Ivchenko et al. (2004b); Blixt et al. (2005); Ivchenko et al. (2005)].

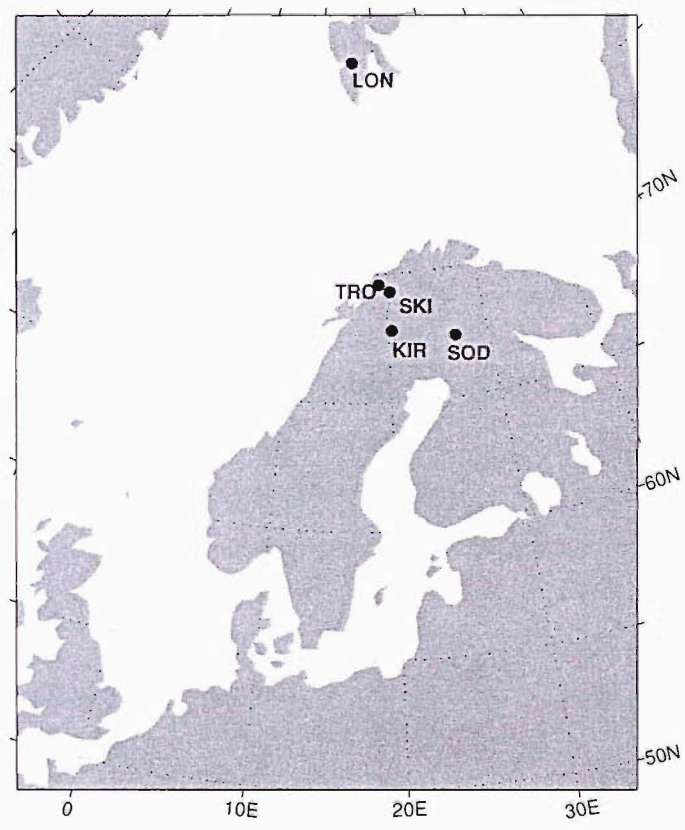


Figure 3.5: Displays the main auroral observation stations in Europe. Courtesy of Eva Borälv.

#### Maintenance

The spectrograph unit and supporting equipment are to be left in the observing location for many years. Observers will be at the observatory with the instrument for no more than 10% of

the year, and this time will be valuable observing time, leaving very little time for instrument work. This situation requires a robust and reliable instrument and support system with stable and durable components requiring little or no maintenance.

## Observation and Control

Observation with the instrument may require it to be operated by a member of the campaign team who may have only cursory knowledge of the spectrograph. As such the instrument control interface is designed to be simple and record all pertinent data into the data file header. Operation requires little or no modification and no routine complex tasks. Likewise the camera and photometer operation is also a simple matter of writing data labels and pressing start/stop when required so the whole platform can be operated by an observer with basic operational knowledge.

## Data Format

### Video Camera Data

The camera can currently record to both PAL SVHS tapes and computer hard disk. PAL format runs at 25 frames/second and has 625 lines of resolution<sup>1</sup> The tape format is very useful for the 350Gb of data that each tape can store. This property, in conjunction with a variable speed video recorder, ensures that even a nonstop ten day campaign can be brought back to the UK on ten video tapes.

Recording data onto videotape is lossy and introduces significant noise. The noise in figure 4.1 displays this. To remedy this, a direct camera-computer recording mechanism was designed, constructed and deployed with the platform in Nordlysstasjonen. The project work carried out on this Auroral Radar Camera System was based on a scholarship from the Marie Curie Trust, and is outside the scope of this thesis. However, the construction of this instrument enables a direct spatial and temporal correlation between the radar electron measurement and higher quality images from the camera auroral emission measurement.

---

<sup>1</sup>NTSC on the other hand has 525 lines and runs at 29.97 frames/second. NTSC is used almost exclusively by the US and Japan.

## **Photometer Data**

Photometer data rate of 5 Hz balances temporal resolution with data file size. Ten days of photometer data can be stored on a single CD.

## **Spectrograph Data**

The data gained during a 10 day campaign fills between one and eight CDs, depending on the detector used. This poses no significant problems for transportation or storage. At present this data cannot be transported via the internet.

## **Future Work: Remote Control**

The small amount of in situ observation time makes it desirable to establish remote control over the platform. Currently Virtual Network Control (VNC) is installed on both of the Windows PCs that control the photometers and spectrograph, and the Linux computer that controls the video camera. VNC is a high bandwidth control mechanism not suitable for control of computers in Nordlysstasjonen due to its low data rate connection. Plans are on the drawing board for a fibre data connection between Svalbard and Norway.

## **Control hub**

The command line interface of the Linux PC is optimal for current low data rate operation. Ideally the control mechanisms for the platform instruments on the Windows PCs should be slaved to the Linux PC and everything controlled via Linux command line. If the start up script for each machine includes network configuration and connection and any daemons required for the slaving process, then if the connection is active, the instrument should be controllable. The command line control also provides the option for scheduling observation tasks through batch scripting and developed into a GUI if/when required.

## **Data Archiving**

Remote controlled systems require automated data archiving. There are various data storage methods available. Of these, computer hard disks are reasoned to be the best choice for archiving

data. They can be placed in a stand alone enclosure for versatility and can be used to store all of the platform data. As time goes by hard disk volume is increasing and their cost dropping, making them the best choice for future data storage. When the fibre optic data connection is made with Svalbard, these data could be downloaded on a trickle (a tiny fragment of the bandwidth dedicated to our download task) and if not, the disks themselves could be brought back and plugged into a raid array, creating an instant online archive.

# Chapter 4

## Spatial Calibration of the Platform

Calibration of the spatial data recorded by the platform instrumentation is achieved through reference to star signatures in the data sets. The platform video camera records a field of view that contains both the other platform instrument fields of view and the star field background. An example field of view from the video camera with an associated time stamp is shown in figure 4.1.

The platform itself is located below a Nordlysstasjon dome. A single GPS reading has a normal distribution  $\sigma$  value of 3.7 meters, that is, the reading is within 3.7m of the measured value 65% of the time [www.wsrcc.com]. In geographic coordinates, this translates to a single reading  $\sigma$  of  $\pm 0.000036^\circ$  in latitude and  $\pm 0.000166^\circ$  of longitude at  $78^\circ\text{N}$ . Assuming this  $\sigma$  is random in nature, twenty GPS measurements were made of the station and averaged to create a station position measurement. The error in this position is reduced by a factor of  $\sqrt{20}$ . These measurements locate Nordlysstasjon at  $78.202491^\circ \pm 0.000008\text{N}$ ,  $15.829220^\circ \pm 0.000037\text{E}$ .

The image in figure 4.1 subtends a field of view of approximately  $12^\circ$  by  $16^\circ$ . The camera, along with the accompanying platform instrumentation, observes the local geomagnetic zenith at an elevation ( $\tau$ ) of  $81^\circ$  and an azimuth ( $\eta$ ) of  $156^\circ\text{E}$ . The camera is focused on infinity and the resulting video frame is inverted to create the field of view with up corresponding to north.

Nordlysstasjon:  $78.202491^\circ \pm 0.000008\text{N}$ ,  $15.829220^\circ \pm 0.000037\text{E}$

The position can be stated without the errors as

**Nordlysstasjon [78.2025°N, 15.829°E]**





Figure 4.1: A single video frame recorded on to SVHS by the platform video camera. It was captured to file by the Southampton Frame Grabber. The image is inverted to display north as up.

## 4.1 Calibration Of Video Data.

The image in figure 4.1 was detected by the HiTIES ICCD video camera. The camera frame is then converted from digital to analogue and recorded in SVHS format on an SVHS videotape. This format has two interlaced frames with a total vertical resolution of 460 rows, an analogue horizontal resolution and frequency of 25 Hz (the interlaced frames occur at a frequency of 50 Hz, alternating with each other). This data format can be digitised into an 8-bit array with 384 columns (x) and 288 rows (y) using a frame grabber.

To calibrate the spatial orientation and measurement of the platform, the stars in this video frame are correlated with stellar position, intensity and where necessary, spectral data. To perform this correlation a visual representation of this reference star field must be created by a sky mapping program such as XEphem or Skymap. The author recommends XEphem [[www.xephem.com](http://www.xephem.com)] with the ppm upgrade for its intuitive interface, functionality, catalogue and freeware distribution.

The reference software star field was sized and oriented to match the field of view of the video frame to aid visual star field recognition. The XEphem was instructed to display stars of a magnitude equal to those in the frame, noting that through the filtered HiTIES video camera the measured brightness of a bluer star appears an order of magnitude weaker than XEphem indicated, and redder stars appear an order of magnitude brighter. Once the star frame was been identified, the video star field data was integrated over one or two seconds to reduce the noise of the video tape to an acceptable level. Next the video frame used for the spatial calibration was taken from a time that contained a well populated, well distributed star field to improve the fitting mechanism. Thirteen stars were selected in the video data frame.

For each identified star, the central pixel coordinates (x,y) and the azimuth and elevation ( $\eta, \tau$ ) (with the exact time of day and observing location) were noted from the reference data and frame viewer. Through mapping each x-y coordinate to each  $\eta$ - $\tau$  coordinate, the data to define a transform between the two coordinate frames is collected. The system used to map a cartesian (x,y) frame to a non-cartesian spherical frame ( $\eta, \tau$ ) is achieved via an equivalent cartesian system described [Lloyd (1971)]. This equivalent cartesian system is denoted with the letters (f,g), where (f,g) are described by equations 4.1 and 4.2 in spherical coordinates defined with respect the centre point of the image, denoted by ( $\eta_{CEN}, \tau_{CEN}$ ).

$$f = \frac{\cot(\chi) \tan(\eta - \eta_{CEN})}{\sin(\tau_{CEN}) + \cos(\tau_{CEN}) \cot(\chi)} \quad (4.1)$$

$$g = \frac{\cos(\tau_{CEN}) - \sin(\tau_{CEN}) \cot(\chi)}{\sin(\tau_{CEN}) + \cos(\tau_{CEN}) \cot(\chi)} \quad (4.2)$$

where,

$$\cot(\chi) = \cot(\tau) \cos(\eta - \eta_{CEN}) \quad (4.3)$$

The standard coordinates (f,g) are a cartesian system related to the cartesian (x,y) frame through a frame offset ( $a_0, b_0$ ) and axis scaling and rotation ( $a_1, a_2$  and  $b_1, b_2$ ). These factors are implemented in equations 4.4 and 4.5.

$$f = a_0 + a_1 x + a_2 y \quad (4.4)$$

$$g = b_0 + b_1 x + b_2 y \quad (4.5)$$

At each identified star the equivalent coordinate system relates the data points  $(x,y)$  to the reference values  $(\eta,\tau)$  using constants  $a_{0-2}$  and  $b_{0-2}$ . These constants are calculated through a least squares fit procedure which requires at least three points.

The centre point  $(\eta_{CEN},\tau_{CEN})$  need not be exactly central, Smart[1965] has shown that no accuracy is lost in the ordinate system through displacement of this point from the centre of the image. The displacement simply results in an offset in  $a_0$  and  $b_0$ . The accuracy of the frame fit increases with both the number of identified star and the evenness with which the points are spread about the frame. An example fit to the star field in figure 4.1 is shown in figure 4.2.

The stars are blurred by the instrument into spread out points.

#### 4.1.1 Fitting a frame

Figure 4.2 contains the star field shown in figure 4.1. A dozen stars in the frame have been identified and the fitting process has been performed using these data. The image displays both frames after they have been mapped together. The pixel image holds the x-y coordinate frame and onto it are mapped the spherical coordinates. To check the accuracy of this fit the star positions have been remapped from the astronomical data to the x-y pixel frame and plotted as circles on the figure. These circles, while not exactly centred on each star in most cases, still contain the star position. The uncertainty of this frame mapping process is a function of the quantity and distribution of identified stars used in the process. An estimate of this uncertainty in the transform is derived from comparing the calculated star positions with the catalogue positions [Lloyd (1971)]. The fitted frame shown in figure 4.2 is accurate to  $\pm 0.022^\circ$ . The angle subtended by the camera frame along its long and short axes are measured directly from this frame transform. The short vertical axis extent is  $11.79^\circ$ . This value is derived from subtracting two frame positions, the error adding in quadrature to give the angular extent of the short video axis to be  $11.79^\circ \pm 0.03^\circ$ . The CCD of the camera has square pixels and the optics of the camera are radial, therefore the angle subtending the long horizontal camera axis can be scaled from the short axis simply using the camera pixel ratio  $\frac{384}{288}$ . Thus the angular extent of the long video axis is  $15.72^\circ \pm 0.04^\circ$ . Each individual camera pixel subtends  $0.0409^\circ \pm 0.0011^\circ$  on both the x and y axis.

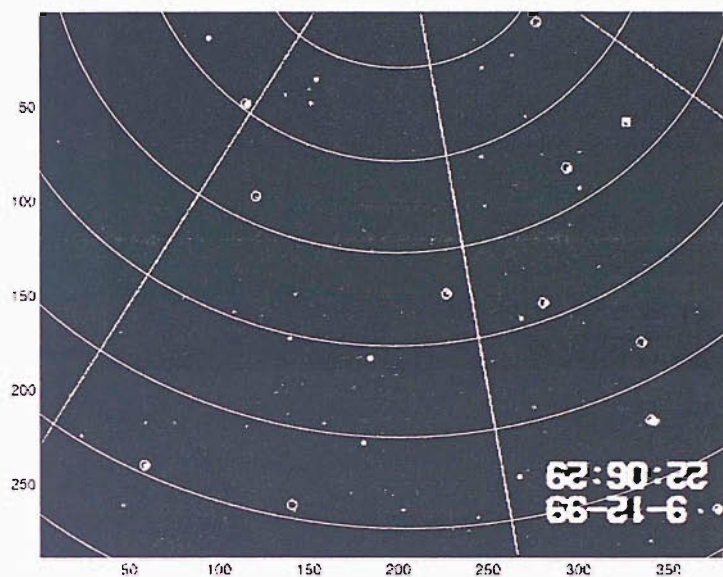


Figure 4.2: The video frame in figure 4.1 has been used here to calibrate the camera field of view. The circles denote the star positions re-calculated from the catalogue azimuth and elevation and transformed into the pixel coordinate frame. The spherical coordinate frame mapped onto the pixel coordinate frame is represented by dotted lines: the straight lines radiating from a point a little out of frame are the lines of azimuth and the incomplete concentric circles are lines of elevation.

The camera field of view subtends the other instrument fields of view on the platform and it is with respect to this calibration that the other instruments are spatially calibrated.

Video Camera FOV: $11.79^{\circ} \pm 0.03^{\circ}$ by $15.72^{\circ} \pm 0.04^{\circ}$ Each Pixel subtends $0.041^{\circ} \pm 0.001^{\circ}$
---

The spatial resolution of the camera system is not limited by the pixel size however. Atmospheric seeing effects, optical components and flaws all contribute to reducing spatial resolution. A star is an excellent light source with which to calibrate the spatial resolution of an instrument, providing essentially a point source of light. Upon entry into the atmosphere, this star light is diffracted by the turbulent atmosphere to a disc approximately  $0.003^{\circ}$  in diameter, fluctuating with the amount of turbulence. This effect is small in comparison to the point spread caused by finite aperture size, optical flaws, foreign particles on the optical components and ICCD digitization and blooming. A star selected from the top right corner of figure 4.1 for analysis of its spread characteristics. A close up 10 by 10 pixel view of the star distribution is shown in figure 4.3.

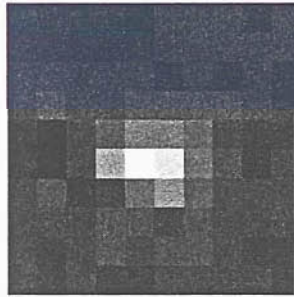


Figure 4.3: A close up of a star in the top right corner of figure 4.1. The starlight is blurred by the atmosphere and detection and recording process into spread out point.

The interlaced video camera CCD reads out the horizontal rows as analogue current signal. The vertical columns are however kept in the quantised form. The differing format of the axes gives a different point spread function (PSF) along the different dimensions. The PSF for both the horizontal and vertical dimension is shown in figure 4.4.

The analogue video encoding of the data results in different spatial resolution along the x and y axes. Thus although the pixels are square and the optics radially symmetric, the spatial resolution of the camera data is different along the long and short axes of the chip. The  $\sigma$  of the point spread function distribution is 0.73 pixels along the short axis and 1.39 pixels along the

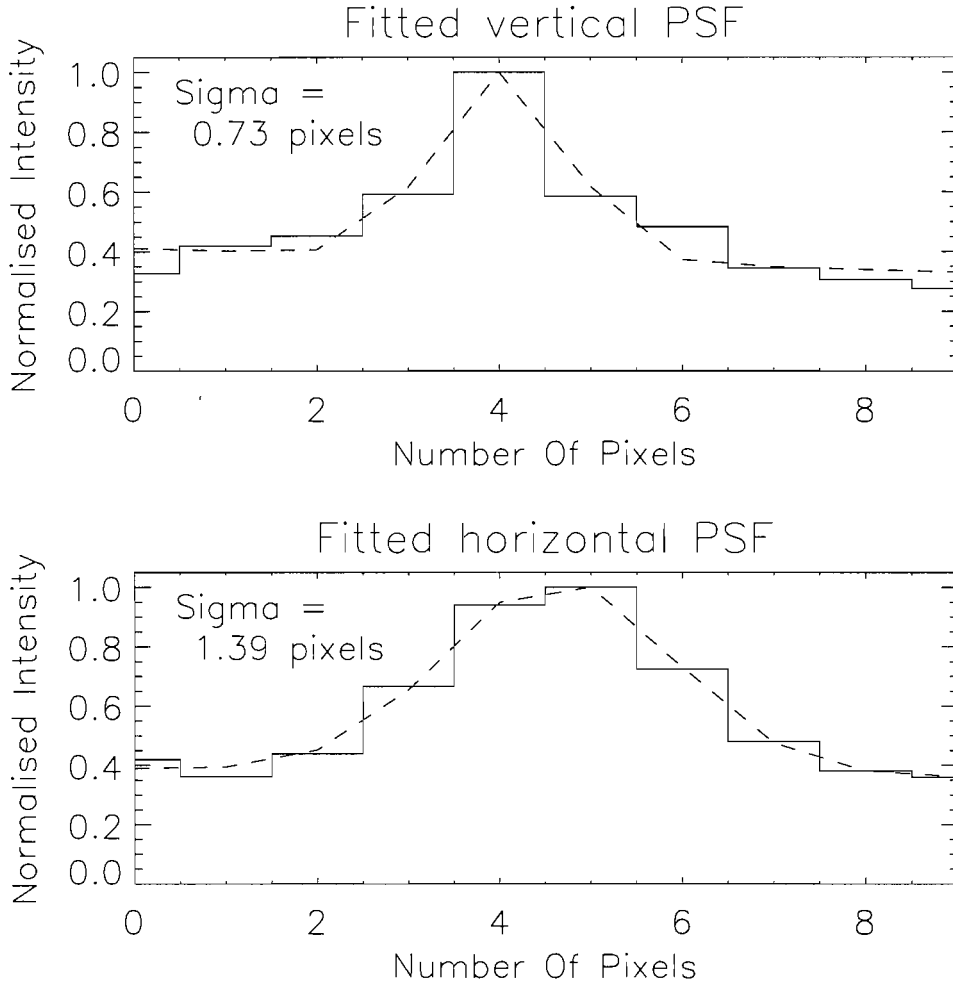


Figure 4.4: The horizontal and vertical PSFs for the star in figure 4.3.

long axis. If resolution of objects is defined to occur when the object is larger than two sigma of the PSF, and the object range is 110 km - the video camera resolves objects  $>120\text{m}$  along the short axis and  $>220\text{m}$  along its long axis. At the time of writing, the camera alignment had remained unchanged since figure 4.1 was captured on the 9th of December, 1999.

## 4.2 Calibration Of Photometer Data.

The platform holds two narrow angle photometers, co-aligned with the camera and the spectrograph and separated from both by just a few centimeters. The photometers are identically designed and constructed by Dr Ian McWhirter. The optics give a  $1^\circ$  field of view [Private Com-

Figure 4.5: The video frame in figure 4.1 is used here to show the field of view of the photometers in the camera field of view. At the time of writing, the neither the photometer or camera alignment have been changed since the image was captured on the 9th of December, 1999.

### 4.3 Calibration Of Spectrograph Data.

The HiTIES aperture is comprised of a fore optic telescope unit and a slit. The slit is constructed from two curved metal edges, the lower edge static and the upper edge with a small range of motion giving the aperture a variable width. The active length of the slit along its curve is  $43 \pm 2$  mm. The 2 mm error related to both the measurement error at each end and the inaccuracy in aligning the optical path onto the full length of the slit. The width of the slit could not be measured directly with the available resources due its sub-millimeter size. However, the slit size was small enough to measurably diffract visible light and the slit width was thus calculated from

Slit Size:  $0.32 \pm 0.12$  mm to  $0.92 \pm 0.32$  mm

the diffraction pattern it created.

#### 4.3.1 Slit Diffraction

In slit diffraction, the zeroth diffraction order contains 90% of the diffracted light and lies at  $0^\circ$  to the path of the incident light. The first order contains 9.4% of the diffracted light and lies at a diffraction angle of  $\alpha$  radians from the path of the zeroth order.  $\alpha$  is described by the slit diffraction equation 4.6.

$$\sin \alpha = \frac{m\lambda}{L} \quad (4.6)$$

where 'm' represents the order of diffraction, ' $\lambda$ ' the diffracting wavelength and 'L' the slit width. Through measurement of the position of the first and higher order diffraction angles for a known wavelength, L can be calculated.

Light from a He:Ne laser ( $6328 \text{ \AA}$ ) was diffracted through the slit and its diffraction pattern placed  $3000 \text{ mm} \pm 20 \text{ mm}$  away on the opposite wall. The position of the first three diffraction orders were clear and measured with a precision error of  $\pm 1.1 \text{ mm}$ , estimated from the inaccuracy in reading and marking the orders. Using equation 4.6 the minimum separation (L) of the aperture jaws was calculated to be  $0.32 \pm 0.12 \text{ mm}$  and likewise the maximum separation is  $0.92 \pm 0.32 \text{ mm}$ . When the aperture is set to minimum width, several discrete flaws along the length of the slit visibly interfere with the transmission of light. Though this does not manifest any notable effect in the data, the flaw reduces the amount of light and therefore the efficiency of the instrument. It may also cause a reduction of throughput at a point on the spatial axis, something to consider whilst troubleshooting flat field issues. The smaller the slit width, the closer the aperture approaches to the ideal light source for diffraction, increasing the spectral resolution. A smaller slit of course means a smaller throughput and consequently less sensitivity. The slit, after this calibration and experimentation period, was set to minimum width to provide maximum spectral resolution.

The slit width has no effect upon the point spread function of the spectrograph, although the



larger slit allows a higher signal to noise for a given integration time. The instrument function will vary linearly with slit width and the spectral axis will move with the centre of the slit.

### 4.3.2 Point spread function

As mentioned for the camera, while a star is a point source, measurements of the star spread its light over several pixels of the CCD. An example spectrograph measurement of the star Draco  $\epsilon$ -63 in figure 4.6 shows the effect clearly.

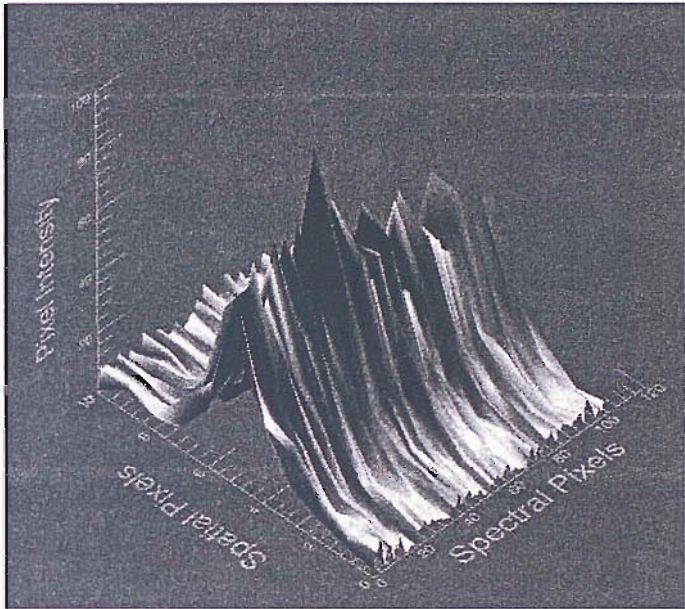


Figure 4.6: This graph shows the light distribution from Draco  $\epsilon$ -63 on the spectrograph pixel array. The point spread function shows an extent of three pixels from its peak along the spatial pixel axis. The spectral axis quantified in pixel number shows a steady point spread distribution along the pixel rows between 4843.1 Å to 4876.2 Å

This point spreading action on the starlight distributes it over eleven pixels on the spatial axis and clearly shows approximately the same PSF in each of the 103 spectral axis rows. This point spread function or PSF of the spectrograph, quantifies the spectrograph spatial resolution. Using this Draco  $\epsilon$ -63 data from figure 4.6 to make an approximate PSF, each of the 103 spectral channels were summed and displayed on a normalised intensity axis in figure 4.7.

Figure 4.7 shows the approximate PSF gained from a star, positioned not exactly in the centre of a pixel. From the asymmetry of the curve it is clear that the peak of the star light distribution

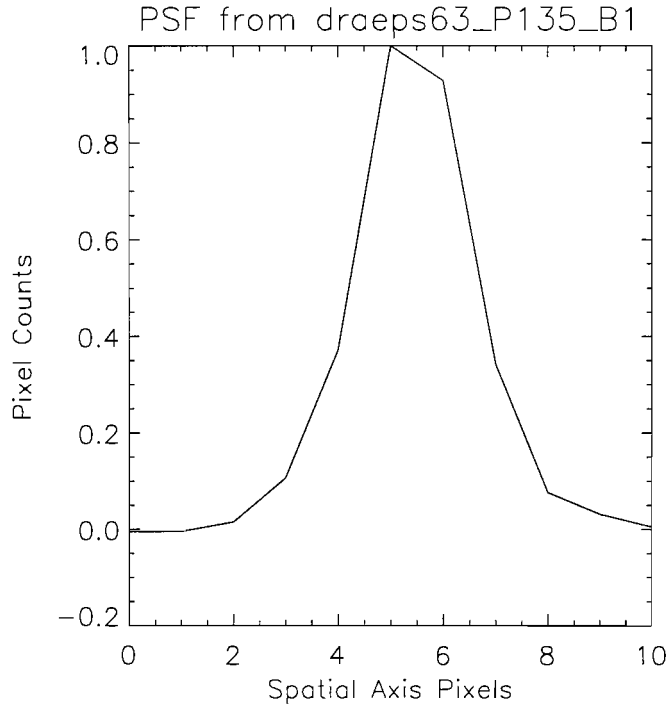


Figure 4.7: A HiTIES measurement of a star. Closely approximating the point spread function (PSF) of the spectrograph.

spread lies somewhere between pixels four and five. If the source of the emission is known to be discrete, as in the case of the star, the PSF can be considered a normal distribution of light about a center point. This center point can then be estimated by fitting a gaussian to the PSF curve. Using the curve in figure 4.7, the gaussfit routine in IDL 5.2 estimates the peak of the distribution to lie on the pixel scale at  $4.64 \pm 0.45$ . This slightly irregular point spread function closely describes the spatial accuracy of the instrument.

### 4.3.3 Star field calibration

The spatial calibration of slit shape, extent and orientation is performed by identifying the star signatures in the data. On a clear night, star signatures are commonplace, introducing regular, spatially discrete interference into the data. An example of a star signature in HiTIES data is shown in figure 4.8.

During the reconstruction of the HiTIES platform in Nordlysstasjonen, the instruments were co-aligned to within a few degrees using a distant mountaintop light source. With the spectro-

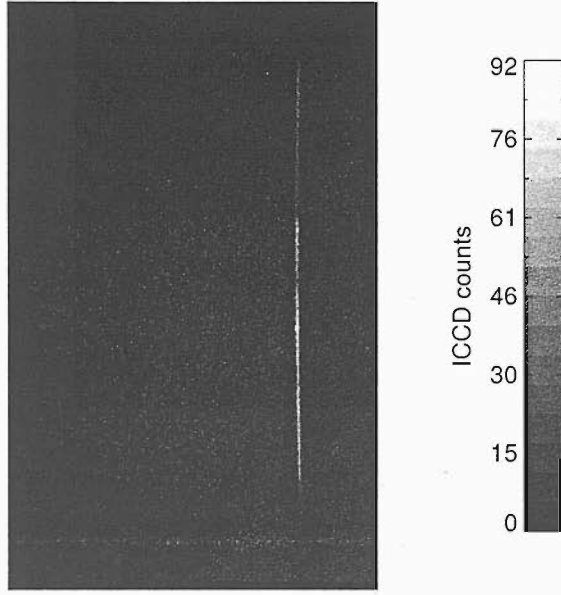


Figure 4.8: Figure showing the signature of a star in HiTIES data. This star is Umi  $\gamma$ -13, identified via video data and the XEphem star catalogue. The slight curve of the line, bending out toward the corners of the CCD is caused by the pincushion distortion from overcorrection of the image plane.

graph field of view known to lie within that of the camera and the orientation of the slit known to lie roughly along the short axis of the video camera field of view, a star correlation process similar to that of the video camera can be performed. An overview of the pixel positions of the star signatures over several hours. The slit subtends approximately  $8^\circ$  and as mentioned before is roughly equivalent to the short (video) axis. The time separation of each the star signatures represents the spatial separation of the stars along the long axis of the video frame. For example, two bright star signatures recorded ten minutes apart at positions 39 and 187 on the 241 pixel spatial axis describe a distinct spatial distribution. The stars are 148 pixels apart. This is  $\frac{148}{241} \cdot 8^\circ$  or  $5^\circ$  vertical separation and a small amount of horizontal separation with the pixel 39 star leading. All of the star signatures can be fitted together in this way and correlation with the identified stars in the video star field becomes a formality.

Using a monitor with an acetate page secured over the screen, the star frame video was played back over the period containing the identified star field. At the exact time of each star signature, a dot was drawn on the acetate screen over the star responsible for the signature with associated pixel number. This was done for all the identified stars measured by the spectrograph and the

resulting line of dots with pixel numbers was used to accurately estimate the slit field of view in the video frame. This process was also useful as an error check as falsely identified stars became obvious as they did not lie along the 'slit'. The result of this process is displayed in figure 4.9.



Figure 4.9: The video frame in figure 4.1 is used here to show the field of view of view of the spectrograph. The spectrograph alignment has not been altered since the image was captured on the 9th of December, 1999.

The pair of star signatures peaking at pixel axis locations of 39 and 187 discussed above were used to measure the spatial extent of the slit. The first star, identified as HD136064, had an elevation of  $79.124^\circ$  from Nordlysstasjonen at that time. The second star, Umi-11, was observed at an elevation of  $83.576^\circ$ . The exact position of the star on the pixel axis can be pin pointed to sub-pixel accuracy by using the PSF distribution. The PSF is effectively a normal distribution about a spatial origin point. A gaussian fit described in equation 4.7 is applied to the PSF ( $F(\lambda)$ ) to accurately describe the peak position.

$$F(\lambda) = A_0 * \exp\left(-\frac{(\lambda - A_1)^2}{A_2}\right) + A_3 + A_4 * \lambda + A_5 \lambda^2 \quad (4.7)$$

where  $A_0$  is the amplitude of the profile,  $A_1$  is the peak, the spatial location of the star,  $A_2$  is the sigma of the PSF,  $A_3$  is spectrally invariant background,  $A_4$  any linear spectral offset and  $A_5$  is quadratically varying spectral offset.

Spectrograph Elevation Extent: $7.25^\circ \pm 0.03^\circ$ Pixel Elevation Extent: $0.030083^\circ \pm 0.000125^\circ$
---

Fitting the normal distribution to the signature of HD136064, its estimated position is refined to pixel  $39.0 \pm 0.4$ ; the one decimal place of accuracy derived from the sigma value of the normal distribution about the point. The Umi-11 is estimated to lie at pixel  $187.3 \pm 0.4$ . For the instrument field of view, the  $148.3 \pm 0.6$  pixel separation of these stars is directly related to  $4.452^\circ$ , the elevation separation of the two stars. As the curvature of the slit is constant, this linear calibration can be extended to the limits of the slit. Thus the elevation range of the slit extends from  $77.94^\circ \pm 0.02^\circ$  to  $84.52^\circ \pm 0.02^\circ$  giving an elevation extent of  $7.25^\circ \pm 0.03^\circ$ . The extent of each pixel along the elevation axis corresponds to  $\frac{1}{241}$  of the  $7.25^\circ \pm 0.03^\circ$  slit extent or  $0.030083^\circ \pm 0.000125^\circ$ .

#### 4.3.4 More Slit Width Measurements

While the spatial extent of each pixel along the azimuthal direction is irrelevant, the azimuthal extent of the slit aperture is required to calculate the instrument collection area. Measurement of this angle was achieved earlier in this chapter using diffraction, but it can also be achieved through timing the passage of stars across the field of view.

The slit was set to minimum aperture, as per usual observing mode. Selecting the lowest practical integration time of 10 seconds, maximum temporal/spatial resolution of the star passing through the field of view is attained. The spectrograph was set to record in this mode until several star signatures were acquired. Unfortunately the day had patchy cloud and only one unambiguous star signature was acquired. Fortunately, this star was recorded at the upper edge of the slit at an elevation of  $83.5^\circ$  and as thus stays within the field of view for the longest period of time, providing a higher accuracy measurement of the slit width. The star signature was present in six consecutive frames in the field of view for between 49 and 70 seconds. By taking into account the relatively tiny star signatures in both the start and end frames the upper end of this limit can be reduced by 10 seconds with confidence. This gives a transit time with the absolute limits of 49 to 60 seconds. These figures are conservative estimates that include seeing



Slit Subtended Angle: $0.059\text{-}0.072^\circ$ Slit width: $0.347 \pm 0.016$ mm - $0.425 \pm 0.020$ mm
---

effects introduced by the atmosphere.

The apparent rotation of the star is a function of its latitude ( $\xi_C$ ) on the celestial sphere. This is equal to the observation latitude (Lat) minus the star elevation ( $\tau$ ). Inserting the numbers we get equation 4.8.

$$\xi_C = 78.202491^\circ \pm 0.000033^\circ - (90 - 83.5167^\circ \pm 0.0111^\circ) = 71.719^\circ \pm 0.011^\circ N \quad (4.8)$$

This star travels  $\cos(\xi_C) * 2\pi$  radians/day. In  $t$  seconds the star travels  $\alpha$  radians:

$$\alpha = \frac{t}{86400} \cos(\xi_C) * 2\pi \quad (4.9)$$

From equation 4.9, a star with a celestial latitude of  $71.719^\circ \pm 0.011^\circ$  travels  $0.064^\circ$  in 49 seconds and  $0.078^\circ$  in 60 seconds. These two figures have negligible error and define the extent limits of the minimum slit width. The slit is arranged along the magnetic meridian,  $24^\circ$  away from perpendicular to the star motion track, thus adding a factor of  $\cos(\frac{24\pi}{180})$ . This gives the subtended slit to be between  $0.059^\circ$  and  $0.072^\circ$ .

This not only provides the angle subtended by the slit but combines with other calibration knowledge to provide an alternative method of measuring the slit area. By dividing the overall slit length of  $43 \pm 2$  mm by the 241 pixels along the axis to derive a elevation extent of  $0.1784 \pm 0.0083$  mm per pixel. The ratio of the elevation angle subtended by pixel  $0.030083^\circ \pm 0.000125^\circ$  over the azimuth angle subtended by the slit of between  $0.059^\circ$  and  $0.072^\circ$  can be used to calculate the slit width. Thus the slit is calculated to have a minimum slit width of between  $0.347 \pm 0.016$  mm and  $0.425 \pm 0.020$  mm. This agrees with the previous measured value of  $0.32 \pm 0.12$  mm.

## 4.4 Spatial Correlation With Other Data Sets.

When correlating collocated instrument data and observable phenomena such as the geomagnetic zenith and the stars, the coordinate frame of azimuth and elevation centred on the instrument

location is the most useful. However, correlating data from the platform with data from distant instruments, requires both data sets to be defined in latitude and longitude. To map these two coordinate frames together an arbitrary altitude is required. An altitude of 110 km is selected. This is the altitude in the range of stopping altitudes reached by precipitating protons and electrons. The frames are also mapped together at a height of 250 km for parallax comparison with the 110 km geometry. To explain the coordinate frame transform, a representation of the video camera field of view is displayed in figure 4.10 in two coordinate frames. The figure shows the camera field of view in spherical coordinates  $(\eta, \tau)$  and a cartesian frame using geographic surface distance and altitude. This frame is the intermediate step in transforming spherical coordinates to latitude and longitude. Transformation of geographic surface distance to latitude and longitude is relatively straight forward.

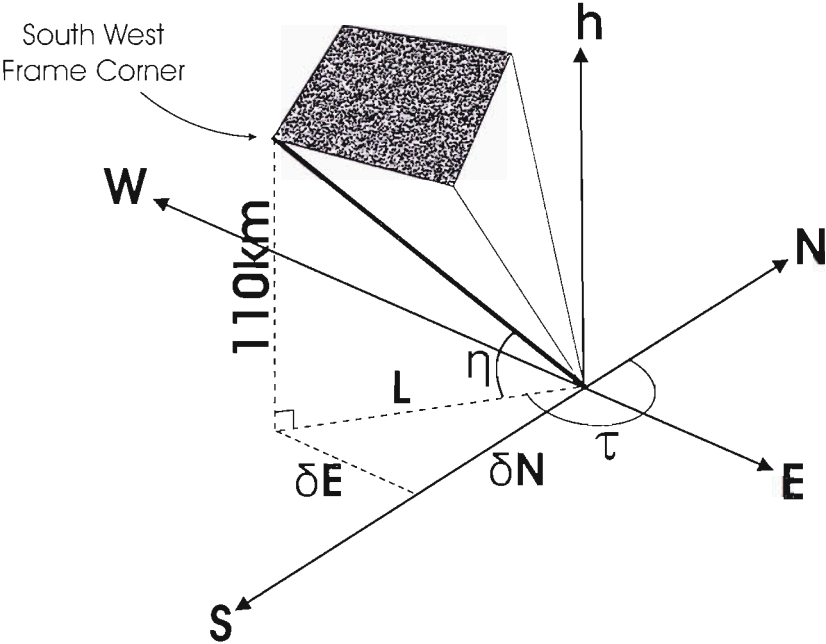


Figure 4.10: Diagram of the video camera field of view in spherical coordinates  $(\eta, \tau)$  and geographic surface displacement  $(\delta N, \delta E)$  and altitude ( $h$ ).

For this transform between spherical coordinates and geographic surface displacement, an approximation of a flat Earth surface was used. At a separation distance of 20 km from the origin, this approximation introduces altitude error of 31.25m or less than 0.03%. The assumption

becomes less acceptable the further the correlated instruments are apart. The origins of both coordinate systems are at Nordlysstasjonen, with positive displacements defined to be in the North and East directions. The spherical coordinates of the corners of the video frame translate to a vector with North-South, East-West and altitude components. For a set altitude of  $h$  km, these displacements are described in kilometers by equations 4.10 and 4.11.

$$\delta N = \frac{h}{\tan(\eta)} \cos(\tau) \quad (4.10)$$

$$\delta E = \frac{h}{\tan(\eta)} \sin(\tau) \quad (4.11)$$

By approximating the Earth as a sphere with a small sinusoidal equatorial radius increase due to centrifugal force, its radius can be closely approximated at the station latitude  $78.2^\circ\text{N}$ . This radius ( $R_{LAT}$ ) at latitude ( $LAT$ ) is given by equation 4.12.

$$R_{LAT} = R_{Pole} + (R_{Equator} - R_{Pole}) \cos(LAT) \quad (4.12)$$

where  $R_{Pole}$  and  $R_{Equator}$  denote the Earth's radius at the given location. The NASA planetary information web site (2000), lists the Earth as having an equatorial radius ( $R_E$ ) of 6378.1 km and a polar radius of 6356.3 km. Using a cosine approximation of the radius change, the Earth's radius at Svalbard ( $R_{Sv}$ ) is found to be 6361.2 km. From figure 4.11, the arc of latitude subtending the North-South displacement can be calculated from equation 4.13.

$$\delta\xi = \frac{\pi\delta N}{180R_{Sv}} \quad (4.13)$$

Again referring to diagram 4.11, the East-West displacement is related to longitude through equation 4.14.

$$\delta\zeta = \frac{\pi\delta E}{180R_{Sv} \sin(90 - \xi)} \quad (4.14)$$

Table 4.1 summarises the frame transform for the video camera field of view at an observation height of 110 km. Using equations 4.10, 4.11, 4.13 and 4.14 the field of view is transformed to latitude and longitude.



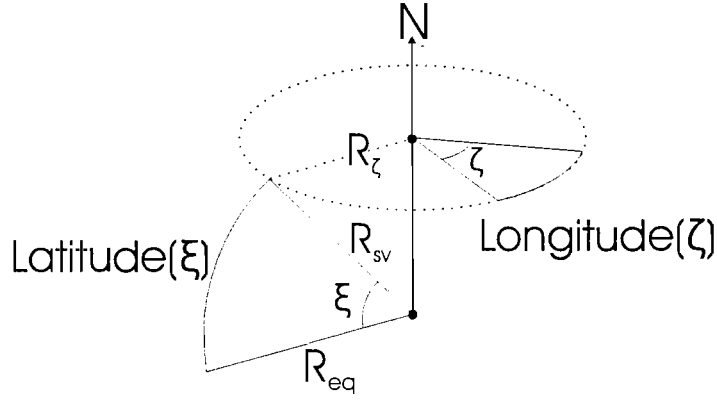


Figure 4.11: Diagram of the latitude ( $\xi$ ) and longitude ( $\zeta$ ) coordinate system.

The same process can be applied to the spectrograph slit between  $77.94^\circ \pm 0.02^\circ$  and  $84.52^\circ \pm 0.02^\circ$  to the right of middle of the video frame and the photometers in the centre of video frame. Knowledge of the latitude and longitude of each instrument field of view allows its data to be correlated with data from other nearby observatories and satellites passing overhead.

As an example, the fields of view of the platform instrumentation are mapped with the boresite of the ESR field aligned dish in figure 4.12. For this purpose the ESR dish positions were measured 30 times with a GPS. Assuming no systematic errors, the ESR fixed dish position is  $78.153063^\circ \pm 0.000006^\circ \text{N}$ ,  $16.03383^\circ \pm 0.00003^\circ \text{E}$ . The ESR field aligned dish is a 42m antenna directed at the geomagnetic zenith with an elevation of  $82.1^\circ$  and an azimuth of  $156^\circ$ . The field aligned dish beam and the platform fields of view are plotted in figure 4.12 for the auroral emission altitude of 110 km and a parallax comparison altitude of 250 km. Assuming that the field aligned dish of the ESR points along the prevailing geomagnetic field, the diagram indicates

Table 4.1: Coordinates of the corners of the video camera field of view.

Frame Corner	Elevation ( $\eta$ )	Azimuth ( $\tau$ )	N-S ( $\delta N$ )	E-W ( $\delta E$ )	Latitude ( $\xi$ )	Longitude ( $\zeta$ )
N-E	81.43°	97.87°	-2.27 km	16.41 km	-0.0204°	0.1596°
N-W	81.98°	239.05°	-7.97 km	-13.29 km	-0.0718°	-0.1293°
S-E	73.40°	139.55°	-24.95 km	21.27 km	-0.2248°	0.2072°
S-W	73.61°	196.85°	-30.97 km	-9.38 km	-0.2789°	-0.0914°

the platform should be angled a few degrees to the west if we wish to do the same.

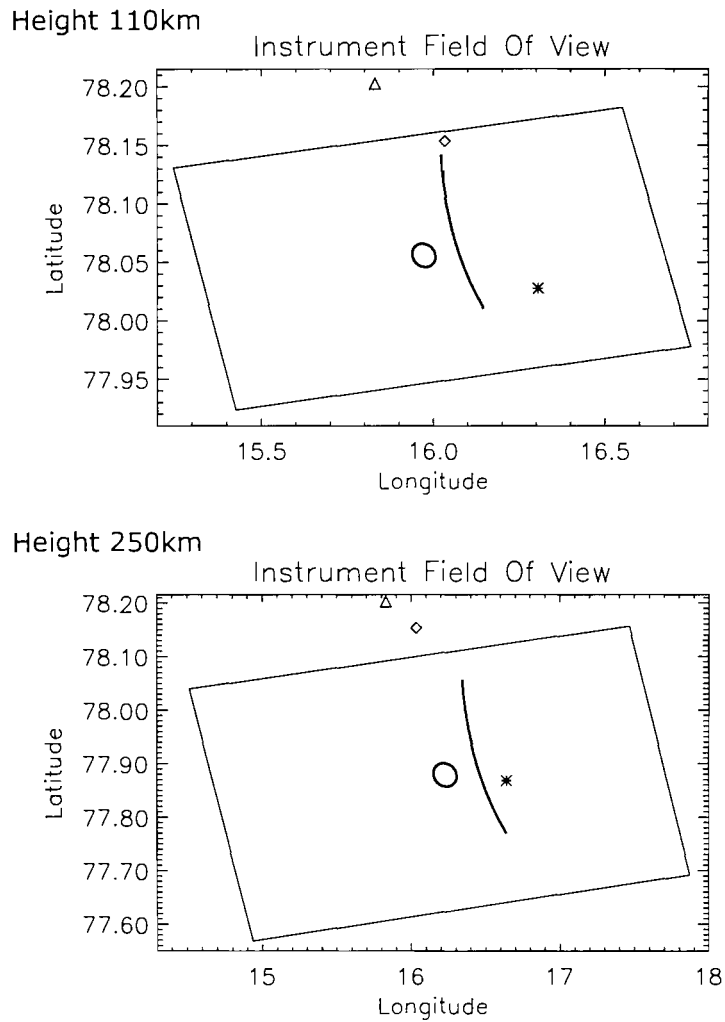


Figure 4.12: Diagram of the platform instrument field of view in the latitude and longitude coordinate system at a heights of 110 km and 250 km. The fields of view of the instruments are represented by a curved line (spectrometer), an oval (photometers), an asterisk (ESR fixed dish) and a parallelogram (the camera). The ground positions of observatories are represented by a diamond (ESR) and a triangle (Nordlysstasjon).

## Chapter 5

# Spectral Calibration

### 5.1 Spectral Characterisation of the Video Camera

The intensifier cathode of the camera is sensitive to light between 2000 Å and 9000 Å. The cathode is most sensitive in the blue/green area of the spectrum. The camera unit also has a wavelength filter which blocks all light below 6500 Å from entering the camera aperture. Meta-stable emissions such as 6300 Å, and to a lesser extent 5577 Å blur the movement of the auroral forms by delaying emission for many seconds after the auroral particle collided with the atmospheric particle. The short wavelength filter enables high time resolution of auroral forms by blocking the meta-stable emissions below 6500 Å. Thus the filtered camera is sensitive between 6500 Å and 9000 Å with the highest sensitivity at the short end of this bandpass.

### 5.2 Spectral Characterisation of the Photometers

Each photonmultiplier tube is capped with an interference filter. Each of these interference filters has been carefully defined to select a particular bandpass. Plots of the wavelength transmission of the four available photometer filters are displayed in figure 5.1. The first filter is  $4651.3 \pm 4.5 \text{ Å}$  and is designed to examine part of the  $\text{N}_2^+(1,2)$  band. The  $\pm 4.5 \text{ Å}$  for these filter descriptions denotes the extent of the bandpass above the FWHM. The second filter is  $4708.8 \pm 4.9 \text{ Å}$  and is designed to examine part of the  $\text{N}_2^+(0,2)$  band. The last two filters are both designed to examine the  $\text{H}\beta$  emission. The first is  $4858.0 \pm 5.3 \text{ Å}$  and the second is  $4857.5 \pm 8.9 \text{ Å}$ . These filters were designed before the width of the Doppler broadened hydrogen emission over Svalbard was known

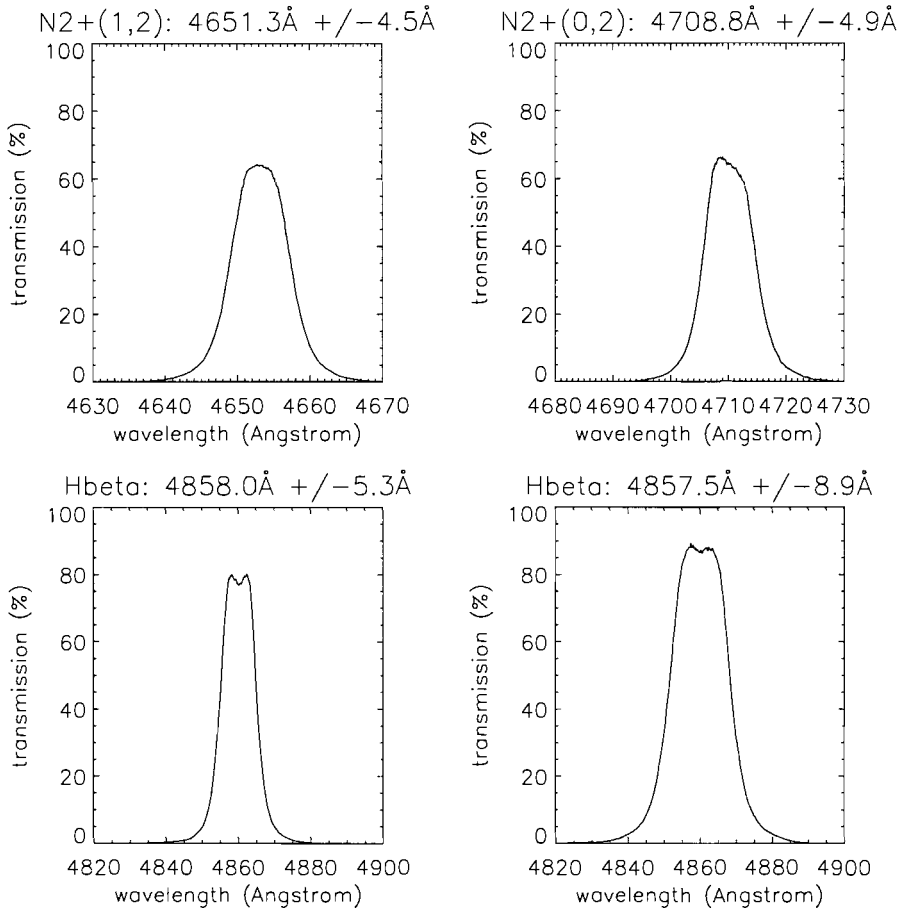


Figure 5.1: The four interference filters for the photometer. The graphs display the percentile transmission curves of each filter as a function of wavelength.

and the second wider filter was selected as being most appropriate after the first detection of the Doppler broadened profile.

## 5.3 Spectral Characterisation of the Spectrograph

### 5.3.1 The Echelle Grating

The echelle grating provides a good deal more spectral coverage than the spectrograph imaging capability is able to record. The diffraction grating utilised by the spectrograph is a soft press of a master echelle grating. However, the diffraction quality of this replica is in all probability superior to that of the grating from which it was pressed due to the carefully inscribed troughs

of the original grating forming the peaks of the replica diffraction rulings. Thus the replica is reproduced with an appreciable gain in efficiency [Thorne, 1974].

Analysis of the grating operation is achieved through equations 3.2 in the instrument section and 5.1 here.

$$\theta - \phi = \psi + \phi \quad (5.1)$$

It can be seen that for a constant angle of incidence( $\theta$ ) and diffraction( $\psi$ ) from a fixed grating, changing the order( $m$ ) changes the diffracted wavelength( $\lambda$ ). The spectrograph CCD sensor subtends not the single diffraction angle discussed above, but a range of diffraction angles. Therefore the CCD subtends a different spectral range for each diffraction order. The spectrograph output is modelled through use of the parameters:  $\theta=60^\circ$ ,  $\varrho=98.76^\circ$  and  $\psi=69-75^\circ$ . The grating blaze angle( $\phi$ ) is calculated through equation 5.1 to be  $66.0^\circ$ . Table 5.3.1 shows the wavelength range for each order and figure 3.2 shows these wavelength ranges graphically.

Above the  $45^{th}$  diffraction order, the range of diffracted wavelengths begins to overlap, diffracting the same wavelength onto different parts of the CCD in different diffraction orders. Investigating wavelengths from orders above 45 can bring about this dual wavelength location with possible interference complications and unless the output is carefully understood, this should be avoided. For the typical grating setup used above, this problem will occur for wavelengths below 4000 Å.

### 5.3.2 Filter Selection

The spectral output of the echelle grating is the wavelength range of every diffraction order superimposed upon each other. For example, from table 5.3.1, it can be seen that the spectrograph CCD subtends 135 Å of the  $27^{th}$  diffraction order, 84 Å of the  $45^{th}$  diffraction order. To examine specific a wavelength range, a specific filter must be placed between the grating and the CCD. The filters used for this purpose have a bandpass of between 40 Å and 50 Å, not quite as narrow as the photometer filters but shorter than the dispersion range subtended by the CCD. This style of interference filter is relatively common and ours were off the shelf commercial purchases. These filters are compiled into 'filter mosaics' discussed in the section 3.2. Figure 5.2 displays the first of two filter mosaics available for experimentation. This mosaic is comprised of four separate bandpass filters. The configuration includes two monatomic oxygen emissions, 5577 Å and 6300 Å and two monatomic hydrogen emissions in the Balmer series, H $\alpha$  and H $\beta$ . This filter

Diffraction Order	Wavelength Minimum	Wavelength Maximum
28	6497.0 Å	6632.5 Å
29	6273.0 Å	6403.8 Å
30	6063.9 Å	6190.3 Å
31	5868.3 Å	5990.6 Å
32	5684.9 Å	5803.4 Å
33	5512.6 Å	5627.5 Å
34	5350.5 Å	5462.0 Å
35	5197.6 Å	5305.0 Å
36	5053.2 Å	5158.6 Å
37	4916.6 Å	5019.2 Å
38	4787.3 Å	4887.1 Å
39	4664.5 Å	4761.8 Å
40	4547.9 Å	4642.7 Å
41	4437.0 Å	4529.5 Å
42	4331.3 Å	4421.6 Å
43	4230.6 Å	4318.8 Å
44	4134.5 Å	4220.7 Å
45	4042.6 Å	4126.9 Å

Table 5.1: The figures here display the bandpass of each diffraction order from 28 through to 45. The following values were used:  $\theta=60^\circ$ ,  $\varrho=98.76^\circ$  and  $\psi=69-75^\circ$ .

arrangement is shown in figure 3.3. Figure 5.3 shows the filter transmission curves for the more commonly used three band filter composition. This filter configuration is designed to transmit the  $H\beta$  emission profile and two  $N_2^+$  bands (4652 Å and 4709 Å). The layout of the filters is shown in figure 5.4.

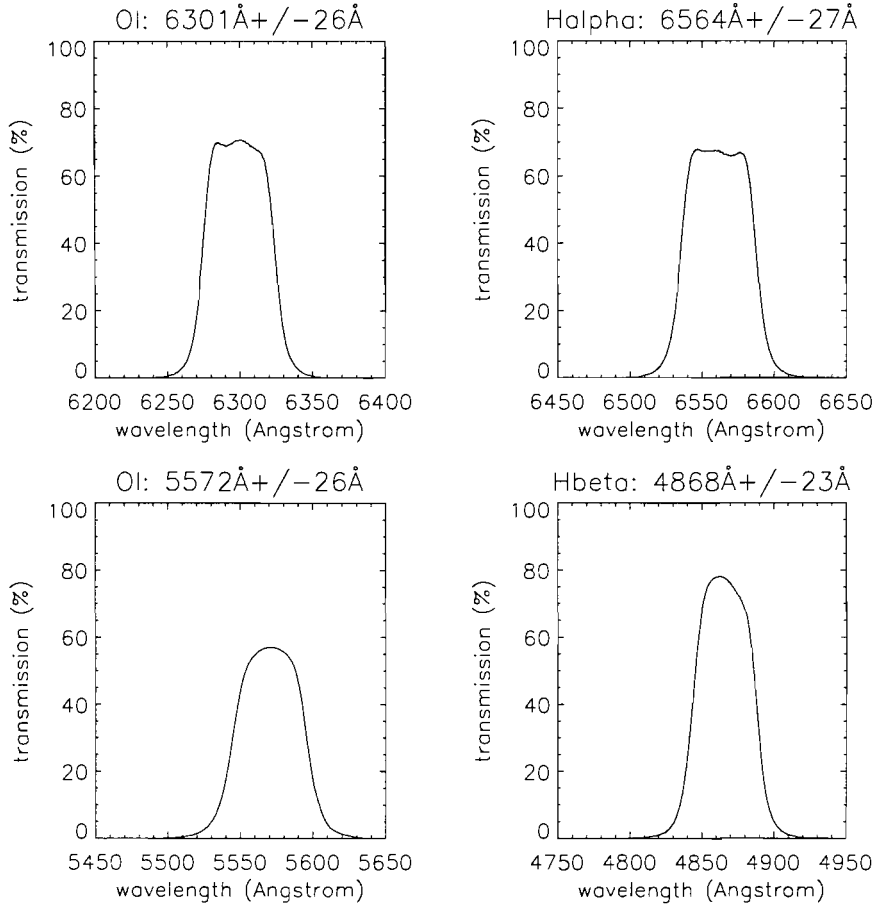


Figure 5.2: The filter transmission curves for the four band filter mosaic shown in figure 3.3. The percentile transmission is plotted against wavelength the four filters: OI( $6301 \pm 26\text{Å}$ ), OI( $5572 \pm 26\text{Å}$ ), H $\alpha$ ( $6564 \pm 27\text{Å}$ ) and H $\beta$ ( $4868 \pm 23\text{Å}$ ).

For the present operation of the spectrograph the three band filter is used. This filter system enables simultaneous coverage of both the auroral proton derived emission ( $H\beta$ ) and auroral electron excited emission in the  $N_2^+$  bands.

The filter mosaics modelled in figures 3.3 and 5.4 are constructions of carefully cut filter sections from larger interference filter panels. The cutting process is detrimental to the structure of the



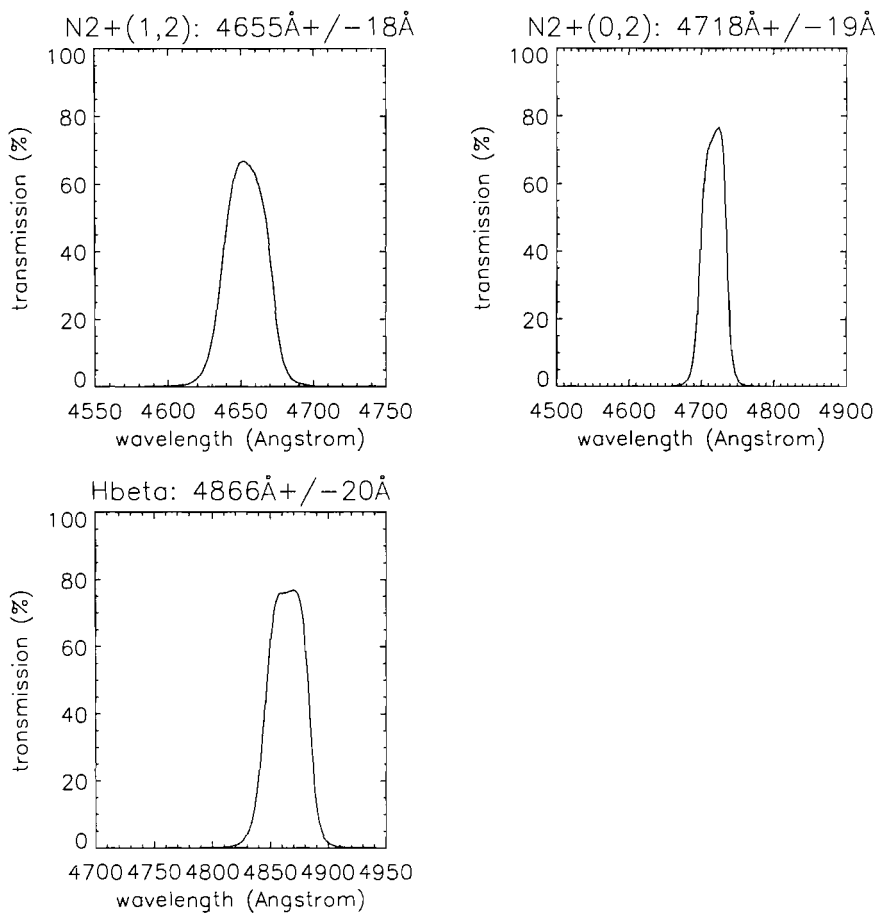


Figure 5.3: The filter transmission curves for the three band filter mosaic shown in figure 5.4. The percentile transmission is plotted against wavelength the three filters:  $N_2^+(1,2)(4655 \pm 18 \text{Å})$ ,  $N_2^+(0,2)(4718 \pm 19 \text{Å})$  and  $H\beta(4866 \pm 20 \text{Å})$ .

fragile filter wafer structure and introduces flaws along the newly cut edge. Unless new filters are designed and made to order with the correct dimensions, data near the filter edges should be avoided.

### 5.3.3 Calibrating the Wavelength Scale

Each filter panel is treated as an independent entity in the wavelength calibration process. The ICCD chip is a 256 by 384 array of pixels which are broken up into the three separate areas of the three band filter. These well defined pixel regions as described by table 5.2.

Initial calibration of the wavelength scale was carried out using known output from element

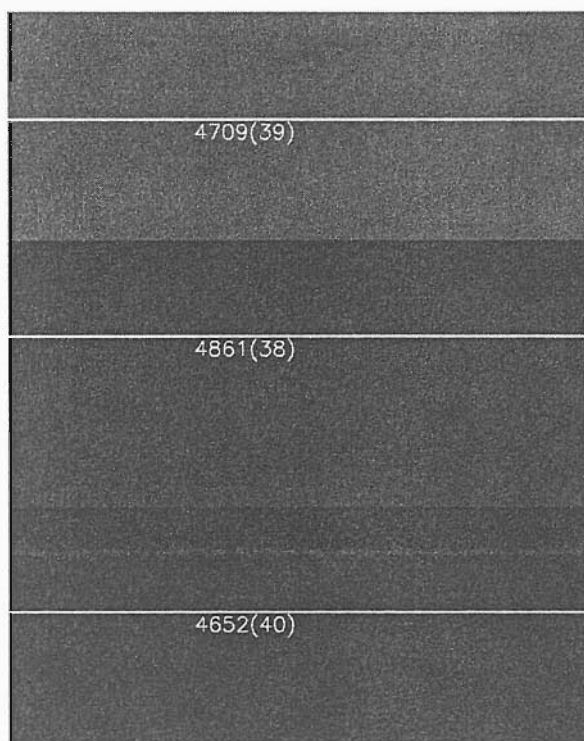


Figure 5.4: Diagram of the three band filter mosaic.

lamps. This process required movement of the grating to position the spectral line onto the CCD. This grating movement changed the dispersion parameters that were to be measured. This process proved invalid. HiTIES requires that the wavelength calibration be carried out without moving the grating from its observation position and at least two known wavelength/pixel conjunctions must be defined within the filter range, preferably as far apart as possible. To solve this several ranges of the Fraunhofer spectrum were used. The Fraunhofer spectrum is investigated more thoroughly in chapter 8, where a mechanism for removing it is described. This spectrum is recorded every day around noon and its form is well known. The Fraunhofer spectrum in the hydrogen panel is displayed in figure 5.5. Only the  $H\beta$  filter of the three band

Table 5.2: Table showing the the pixel ranges of the three band filter on the ICCD.

Filter Panel	Spatial Pixels	Spectral Pixels	Total Pixels
N 4709	13:253	38:121	241x84
$H\beta$	13:253	134:236	241x103
N 4652	13:253	246:338	241x93

mosaic is calibrated here. None of the other filter panels were used in this thesis.

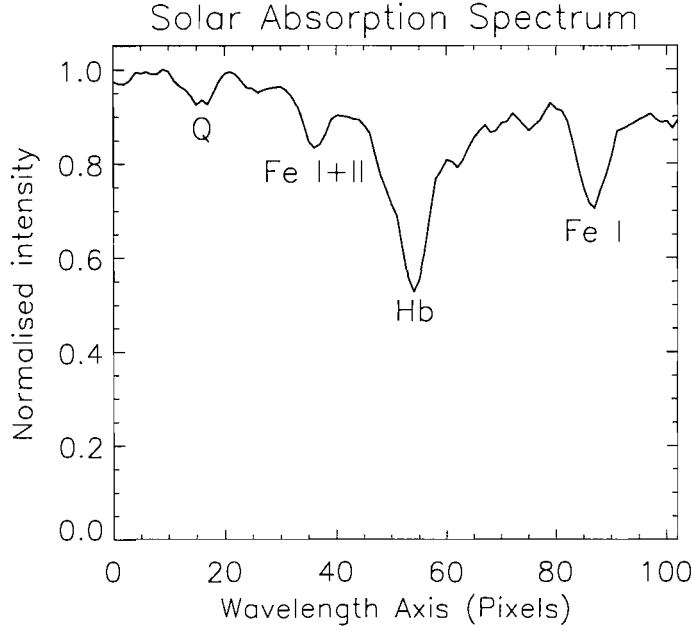


Figure 5.5: Plot of the data integrated between 08:45 UT and 10:01 UT on the 30<sup>th</sup> of November, 2000. The wavelength axis is plotted with pixel number and the features are identified through reference to a Fraunhofer almanac.

Identification of the absorption features is achieved through shape correlation with a library Fraunhofer spectrum reference. Using this an exact wavelength can be assigned to each peak. For example, the feature that is obviously H $\beta$  4861.342 Å peaks at pixel 54 in the filter. A first linear estimate of the dispersion across the filter is achieved through division of the wavelength and pixel separations from the H $\beta$  feature. These estimates are displayed in table 5.3.

Given that an error in the dispersion measurement of one pixel would produce an error of 0.01 Å/pixel the disagreements in dispersion estimates are almost acceptable. Looking at equation 5.2 we see this is not the case. The angles  $\psi_{MAX}$  and  $\psi_{MIN}$  represent the limits of the diffraction angle, subtended by the length ( $L_P$ ) of the CCD pixel array.

$$\Delta = \frac{1}{\rho L_P} \frac{\sin(\psi_{MAX}) - \sin(\psi_{MIN})}{m} \quad (5.2)$$

From equation 5.2, it can be seen that the number of Ångströms per pixel decreases with increasing order. This relation also shows that the grating dispersion varies non-linearly with

Table 5.3: This table shows the pixel positions and wavelengths of known features in the Fraunhofer absorption spectrum and dispersion values derived from them.

Absorption Feature	Known Wavelength	Pixel Number	Dispersion( $\Delta$ ) Relative To H $\beta$
H $\beta$	4861.342 Å	54	N/A
Fe I	4871.734 Å	87	0.315 Å/pixel
Fe I+II	4855.418 Å	36	0.329 Å/pixel
Fe2Fe	-	-	0.320 Å/pixel

Table 5.4: Table of the polynomial calibration factors is used to calculate the pixel wavelength (Å) from pixel number(p). This calibration is only valid for the 103 pixel hydrogen filter, where p runs from 0-102 (134-236 on the ICCD).

Filter Name	Calibration polynomial
H $\beta$	-5.83282e-4 p <sup>2</sup> + 0.390031p + 4841.74

the dispersion angle. This is the non-linearity seen in table 5.3 and it necessitates a non-linear calibration of the axis. The IDL Poly\_fit.pro routine was used and its results are shown in table 5.4. The accuracy of the fit depends on the accuracy of the pixel-wavelength intersections, the number of intersections and the spread uniformity. Thus, even though the fit is more accurate than the linear calibration, it could be improved by identifying more spectral features within the bandpass. Of course the H $\beta$  emission was selected as its bandpass was relatively uncontaminated by identifiable features.

### 5.3.4 Calculating the Spectral Resolution

The spectral resolution of the instrument, or ‘instrument function’ is a similar concept to the point spread function of the spatial axis. The imperfections of the instrument optical path blur the spectral axis. To measure this instrument function(IF) a similar tactic to the PSF spatial axis is used. The output of a spectrally discrete spectral feature (a laser) is examined and the resulting wavelength response will define the instrument function. The profile shown in figure 5.6 is the spectral signature of a He:Ne laser operating at a wavelength of 5433.7 Å, diffracted onto the CCD in the 34<sup>th</sup> diffraction order - as measured by HiTIES. It has been averaged along

the spatial dimension to improve the S/N of the curve and just the relevant pixels have been plotted.

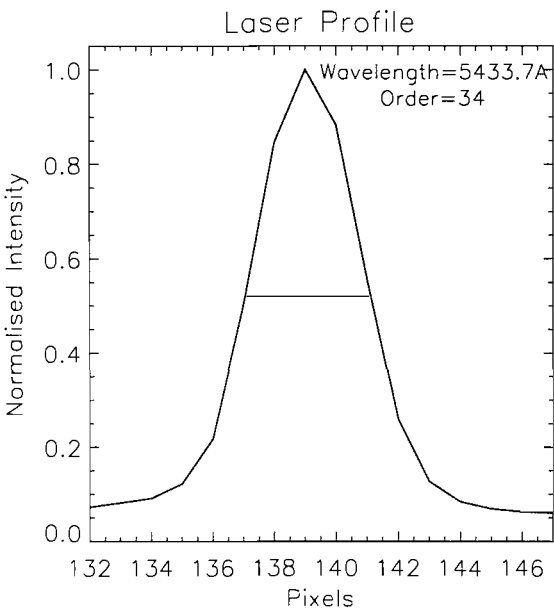


Figure 5.6: Laser line measurement of a 5433.7 Å He:Ne laser in the 34<sup>th</sup> diffraction order. The gaussian analysis reveals the peak exists at pixel 8.03±1.62.

The gaussian line profile is caused by scattering and dispersive processes as the light travels along the optical path of the instrument. The sigma value of this distribution is 1.62 pixels. thus the spectral properties of this normal distribution can be defined as 8.03±1.62 pixels. The shape and size of the instrument function, measured in pixels, must be assumed to be invariant with grating movement. It defines the resolution in pixels, but calculation of the spectral resolution in each of the useful orders is required.

As already mentioned, the spectrograph CCD has the ability to capture between 135 Å (27) and 84 Å(45) in orders 27 through to 45. Using equation 5.2 with a fixed spectrograph setup and grating angle, we find that dispersion is inversely proportional to diffraction order(m). This is described by equation 5.3

$$\Delta = \frac{C}{m} \tag{5.3}$$

where  $\Delta$  and  $m$  are again dispersion and order and  $C$  is a constant defined in  $\text{\AA}/\text{pixel}$  related to the fixed grating configuration of the spectrograph. Referring to table 5.3 the average dispersion measured in order 38 is  $0.321 \text{ \AA}/\text{pixel}$ . Therefore,

$$C = \Delta m = 0.321 * 38 = 12.21 \quad (5.4)$$

where  $C$  is constant at 12.21 aside from

If the sinusoidal perturbation introduced by the echelle grating is considered to be negligibly small,  $C$  is constant at 12.21. While this is a systematic error, it is not fitted and thus it will be treated as a small variance that can be used to calculate the error in  $C$ . The dispersion 'variance' is  $\pm 0.00005$ . This approximates  $C$  as  $12.21 \pm 0.00191 \text{ \AA}/\text{pixel}$ , a negligibly small variation.

As the IF is defined as being 3.24 pixels wide, the spectral resolution limit ( $\alpha_{IF}$ ) is defined by equation 5.5 and 5.7.

$$\alpha_{IF} = \Delta * 3.24 [\text{\AA}] \quad (5.5)$$

Substitute in the equation 5.4

$$\alpha_{IF} = \frac{39.56}{m} [\text{\AA}] \quad (5.6)$$

The error in this figure is negligible. Using this equation to calculate the spectral resolution of the hydrogen filter in order of 38, the spectral resolution is  $1.04 \text{ \AA}$ .

Note here that varying the slit width varies the instrument resolution. These calculations have been carried out at minimum slit width/maximum spectral resolution. To first order, increasing the slit width linearly decreases the spectral resolution. To put this mathematically,

$$\alpha_{IF} = \frac{39.56}{m} \frac{L}{L_{MIN}} [\text{\AA}] \quad (5.7)$$

where  $L$  is the slit width in mm and  $L_{MIN}$  is  $0.425 \pm 0.054 \text{ mm}$ , the minimum slit width.

## Chapter 6

# Brightness Calibration

This chapter describes two alternative methods of calibrating the brightness scale. A purely theoretical method and a part theoretical method uses an efficiency measurement on a star.

### 6.1 Surface Brightness Unit

The ideal auroral brightness measurement would be to count of the photon emission from a given volume of atmosphere, for example in photons/s/cm<sup>3</sup>. Outside a laboratory, the closest measurement that can be achieved is a count of the photons emitted from the column of atmosphere subtended by the aperture into the sensor in photons/s/(solid angle of instrument)/(sensor collection area).

Since the publication of Chamberlain (1961), the Rayleigh is the accepted unit for measuring column emission rates of the atmospheric airglow. This unit of surface brightness is named for the 4<sup>th</sup> Baron Rayleigh, Robert John Strutt (1875-1947). The Rayleigh is defined as column integrated isotropic emission of  $10^{10} \text{photons.s}^{-1} \cdot (1/4\pi) \cdot \text{sr}^{-1} \cdot \text{m}^{-2}$  [Baker and Romick (1976)] or one megaphoton per second per steradian per cm<sup>2</sup>.

$$1R = \frac{10^6}{4\pi} \text{s}^{-1} \text{ster}^{-1} \text{cm}^{-2} \quad (6.1)$$

This standard unit of surface brightness works out to be 79577.5 photons s<sup>-1</sup> sr<sup>-1</sup> cm<sup>-2</sup>

## 6.2 Conventional Brightness Calibration of the Spectrograph

To calibrate the CCD and ICCD sensor, a calibrated source was required. In our case this source was a flat field tungsten lamp, calibrated with respect to a primary C14 standard lamp. Unfortunately the initial calibration data from Boston was unusable; it provided neither an adequate black body fit to extrapolate back to, nor covered the wavelength range of interest. Without these measurements the calibration lamp, intended as a secondary source, became useful only as a flat field lamp. Furniss presented the first brightness calibration of the HiTIES spectrograph [Furniss, priv. comm.].  $H\beta$  measurements scaled with this calibration are an order of magnitude more than the  $H\beta$  measurement of the Nordlysstasjonen meridian scanning photometer (MSP) and rejected as unrealistic. This ended our attempt to calibrate the brightness scale of the ICCD data set through comparison with a conventional standard lamp.

## 6.3 Theoretical Brightness Response

It is difficult to calibrate an instrument brightness scale in Rayleighs. Instruments in the Canadian chain of MSPs, built similarly and calibrated with the same methods by the same person, develop discrepancies of up to 100% [Eric Donovan, priv.comm.]. As this situation arises in relatively homogenous instrument chain, the brightness calibration of instruments around the world must, by inference, vary greatly.

Given the unit definition and a number of instrument parameters, the theoretical instrument count response to a Rayleigh of brightness subtending the field of view can be calculated. The solid angle of emission observed by the spectrograph is opposite but equal to that of the spectrograph aperture. The spectrograph solid angle is found by multiplying the angle subtended by the slit length ( $0.1265 \pm 0.0005^\circ$ ) and the slit width ( $0.00113 \pm 0.00009^\circ$ ); resulting in a subtended solid angle of  $0.000143 \pm 0.000011$  sr. The slit length of  $43 \pm 2$  mm is mapped directly to the  $112 \pm 3$  mm aperture diameter, creating a length magnification factor of 2.6. The slit length times by the slit width (0.386mm), magnified by this factor, results in a collection area of  $0.126 \pm 0.119$  cm<sup>2</sup> at the aperture. If the aperture of the spectrograph is entirely illuminated by a Rayleigh of brightness then it will detect  $79577.5 * 0.000143 \pm 0.000011^\circ * 0.126 \pm 0.119$  cm<sup>2</sup> photons per second or  $12.81 \pm 1.67$  photons/s.



## 6.4 A Practical Brightness Calibration Method

The instrument does not detect all the photons incident upon it. The fraction of these photons that are detected, can be calculated from measuring a known photon source. For this purpose the intensity of a number of known stars were measured. The number of counts from each star was divided by the catalogue flux of that star. This ratio represents a measurement of the efficiency of the spectrograph.

Additionally, this star field offers an identical primary calibration source to all instruments in the northern hemisphere, although stellar intensity typically varies by a few percent over time. A measurement of a star signature even includes the local atmospheric opacity at the location and altitude of the instrument. These calibration star signatures are intrinsic to the data taking process and require no additional experimental effort on the part of the observer to collect. the calibration can all be achieved post-experiment.

To perform this calibration method, the instrument requires a spatial resolution of at least  $10'$  and the ability to identify stars passing through the field of view. This is achieved here using a spatially correlated imager with a  $10^\circ$  by  $10^\circ$  field of view. It is assumed that for a constant level of intensification, the ICCD has a linear brightness scale. The calibration has two parts. The first part is the theoretical brightness response described in the previous section. The second part involves measuring the observation efficiency of the instrument in situ. This is done by comparing the measured counts from an identified star to the catalogued photon flux of that star.

### 6.4.1 An Efficiency Calculation Using Starlight

The spectrograph aperture has a collection area of  $98.5 \pm 2.6 \text{ cm}^2$  for a star is wholly imaged within the slit. Using only those frames which have strong star light signatures before and after, the experimental method ensured the frame observes the whole star throughout the integration. Starlight arrives at the instrument sensor as a point spread function shown figure 5.6. The turbulent atmosphere introduces a spread of around  $10''$ , which is inconsequential when compared to the instrumental imperfections such as finite slit size, optical flaws and foreign particles in the optical path introduce a spreading action of around  $200''$ . An illustrative measurement of Draconis  $\epsilon$ -63 is shown in figure 4.7. This starlight distribution is summed to value of 17,395 counts, and these counts are equated to the catalogue flux of the identified star, Draconis  $\epsilon$ -63

Table 6.1: This table shows the counts measured by the spectrograph for five separate stars. The unusual spectrograph unit in the second column indicates the counts per integration over the filter bandwidth and collection area. The error in the third column is derived from the inaccuracies in the second column unit. The catalogue flux for each star is an average of the values at 4850 Å and 4875 Å in the units of the catalogue.

Star Name	Spectrograph Counts $/25s/33.40 \pm 0.15\text{\AA}/98.5 \pm 2.6\text{cm}^2$	Spectrograph Counts $(/s/\text{cm}^2/\text{\AA})$	Catalogue Flux $(Photons/s/\text{cm}^2/\text{\AA})$
Dra $\epsilon$ -63	17395	$0.211 \pm 0.006$	24.8
Dra $\delta$ -57	36406	$0.443 \pm 0.012$	49.2
Dra $\sigma$ -61	8281	$0.101 \pm 0.003$	12.2
Umi $\gamma$ -13	44500	$0.541 \pm 0.014$	64.0
Umi-11	4359	$0.053 \pm 0.002$	6.7

over the 33.4 Å H $\beta$  filter range. Five stars were identified and used in this way to measure the efficiency of the Spectrograph. The catalogue flux was taken from a star-specific online astronomical catalogue like that available from <http://vizier.cfa.harvard.edu>. The data for these stars were recorded and summarised in table 6.1 along with the spectrograph measured counts and catalogue photon flux for that star over the spectral range of the H $\beta$  filter. The catalogue star flux is listed in photons/second/cm<sup>2</sup>, the spectrograph values are listed first as counts/exposure time/bandpass/receiver area and then counts/second/Å/cm<sup>2</sup>. The counts in this table are equivalent counts, created through flat fielding the data, described in section 7.2.

The measurement of star signatures should be made during optimal seeing conditions. The calibration will then stand for optimal observing conditions, and the effects of less than optimal conditions can be taken into consideration by observers. Additionally, the versatility of this calibration method allows re-calibration of every data frame containing a known star. Once the calibration is in place, an updated calibration based on the current seeing conditions may be possible every hour or so during the data analysis process. This makes the efficiency and opacity estimate as accurate as possible and thus the measured brightness as close as possible to the true emission values of the upper atmospheric emission. After a period of time, the database of calibrated stars will provide a resource for stellar variability and local opacity studies and enable further accuracy in the calibration. The opacity estimate for these observations is near

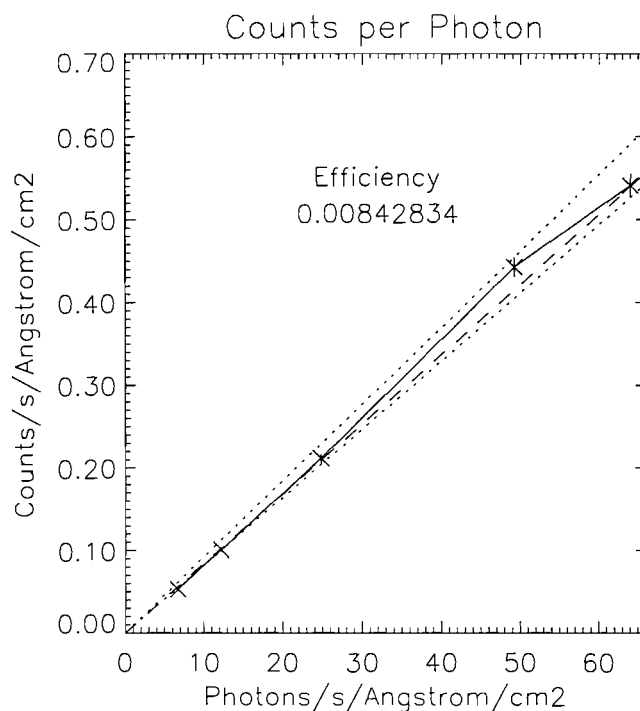


Figure 6.1: This graph shows the ICCD counts per photon data from table 6.1. The gradient is the factor relating counts to photons.

optimal. at around 20%, representing clear weather conditions for Svalbard.

To reduce the spectrograph counts per frame to counts per second a factor of  $\frac{1}{25}$  must be introduced. To reduce the spectrograph counts per bandpass to counts per Å, a factor of  $\frac{1}{33.4}$  is required. And to reduce counts per detector area to counts per  $\text{cm}^2$  requires a factor of  $\frac{1}{98.5}$ . This makes a composite factor of  $1.21584\text{e-}5$  to transform counts  $/25\text{s}/33.40 \pm 0.15\text{Å}/98.5 \pm 2.6^2$  to counts/s/ Å/ $\text{cm}^2$ . Using the count data in table 6.1 in counts/s/ Å/ $\text{cm}^2$  the graph in diagram 6.1 was plotted. From this graph the average factor between these values is  $0.00843 \pm 0.00002$  counts per photon, with curve analysis providing the error estimate. This is the instrument efficiency. This measurement encompasses losses due to dome and lens scattering, atmospheric opacity, grating dispersion, filter transmission and detector quantum efficiency. Combining this efficiency with the theoretical brightness measurement. a Rayleigh of brightness filling the instrument field of view results in  $0.108 \pm 0.014$  counts/second. Conversely, one count represents  $9.263 \pm 1.208$  Rayleighs. The Doppler shift of the catalogue star has not been taken into account. This effect may have an effect on the measured star intensity. The calibration error using this measurement method is  $\bar{20}\%$ .

Table 6.2: Estimated efficiencies of the components in the HiTIES optical path.

Item	Transmission(%)	Estimation Error
Atmosphere*	80	$\pm 10$
Dome	95	$\pm 3$
Lenses	92	$\pm 1$
Grating	29	$\pm 5$
Filter	79	$\pm 1$
DQE	50	$\pm 10$
Total	8	

### Failure of the Starlight Efficiency Measurement

Although this calibration method has been peer reviewed and included in the thesis, the results it produces are unrealistic at an order of magnitude above that of the Nordlysstasjon Meridian Scanning Photometer (MSP) and the brightness we expect from previous research.

### HiTIES Measurement Efficiency Estimate

Due the discrepancy with the MSP, another method of estimating the efficiency was found. The optical path was broken down into component parts and their effects on transmission were measured or estimated. A list of these components and related optical transmission is presented in table 6.2. The values are either known, in the case of the lenses and filter efficiency, or approximated with an accuracy represented by the error.

This table gives the instrument efficiency expected by the instrument constructors, 5-10% [Priv.Comm., J. Baumgardner, 2000]. Using this value as the counts per photon efficiency produces the Rayleigh instrument response of  $0.419 \pm 0.014$  counts/s per spectrally integrated pixel. Reversing this statement, 1 count equals  $2.39 \pm 0.09$  Rayleighs. This is closely comparable with the MSP and produces the brightness expected from the literature. Thus this efficiency calculation provides the brightness calibration for the figures in this thesis. The brightness scale has an error of 31% when calculated in this way.

## 6.5 How Does the Spectrograph Performance Relate to Proton Aurora

This section summarises the calibration sections by comparing the performance of the platform to proton aurora.

### Spectrograph

The dispersion of precipitating protons/hydrogen produces proton aurora over several degrees of latitude [Oguti (1973)]. The spatial resolution of the spectrograph is high enough to study all but the smallest auroral forms [Lanchester et al. (1997)]. Proton aurora is typically broader than the field of view. The shape of the Doppler shifted profile contains information on the emitting particle population. The spectral resolution of 1.3 Å allows a details measurement of the profile, suitable for studying the Doppler profile of auroral hydrogen emission. The spectrograph is able to detect emissions as low as a single Rayleigh. The timescale of a proton auroral substorm is much faster than HiTIES integrations.

### The Video Camera

The camera filter removes H $\alpha$  and H $\beta$  emission, so the camera is useful only as a secondary source of information when studying proton aurora. It records electron activity during the studied event and is used during calibration. The camera field of view records the form and relative brightness of the electron aurora within the fields of view of all platform instrumentation. These data are then invaluable when interpreting other data at a later stage. At 110km, the spatial resolution of the video camera is not quite high enough to observe electron aurora below <100m scale [Lanchester et al. (1997)]. The video camera always records more than seven fields a second, so it is always high enough to record auroral morphology. The gain of the camera intensifier is constant at maximum, but the non-linear range of this sensor is unsuitable for intensity calibration.

## The Photometers

The temporal resolution of the photometers over-samples auroral morphology of both hydrogen and electron aurora. The photometer photomultiplier tube detector is the most sensitive instrument on the platform and is useful as an indication of the amount of activity present at any given time. The one degree field of view is small compared to the extent of the proton aurora. Photometer data were not used for the work in this thesis.

## Chapter 7

# Removing Instrumental Artifacts from the Data

This chapter describes the methods developed to remove the instrumental effects and unwanted artifacts from the raw data. The origins and forms of noise are analysed and techniques to minimise or eliminate these extraneous signals were developed. These cleaning processes treat each pixel as an individual detector to preserve data integrity.

### 7.1 Dark Subtraction

The CCD detector is a complex electronic system and many forms of unwanted circuit current may be introduced to the data [Janesic et al. (1989)]. The dark subtraction process removes counts not attributable to incident photons. The exact source of these counts and their removal is discussed in this section.

#### 7.1.1 Dark Current

The dark current is a population of electrons developed in the silicon substrate of the CCD through the thermal kinetics of the lattice. The work potential of pure silicon is very low and it is this property that makes silicon an ideal optical sensor. The silicon substrate is arrayed with potential wells or 'pixels' to capture photoelectrons created nearby. The temperature or kinetic energy of the silicon lattice takes the form of quantised lattice vibration or phonons. When these

Table 7.1: The manufacturer listing of the Boston bare CCD thermal noise as a function of temperature.

CCD Temperature (Kelvin)	Thermal electron production rate (electrons $s^{-1}cm^{-2}$ )
293	$144*10^9$
258	28
223	<1

phonons are of sufficient energy, they can release a lattice electron. This population of phono-electrons are also gathered into the pixels and become indistinguishable from the photoelectrons. The number of electrons per second ( $N_{eps}$ ) produced by the thermal vibration of the substrate is an exponential function of temperature (T). This relation is shown by Janesic et al. (1989) in equation 7.1.

$$N_e = 2^{\frac{T-T_0}{\gamma}} \tag{7.1}$$

where  $T_0$  is approximately 224 K for pure silicon and  $T$  is the temperature of the substrate. For practical purposes  $T$  is considered as  $\overline{T}$ , the average temperature during the integration period.

### Boston CCD

Table 7.1 shows the Boston CCD dark current as a function of temperature, as supplied by the manufacturer. These data are plotted with the thermal noise equation ( 7.1) in figure 7.1, and it can be seen that the agreement is very good.

The thermal electron production rate at room temperature is almost a thousand electrons per second per pixel volume. It is clear from equation 7.1, that effective minimisation of the dark current can be achieved by reducing the silicon temperature to near or below  $T_0$ . For the Boston CCD, this reduction in detector temperature is achieved using a liquid cryogen coupled to a peltier thermocouple in the CCD substrate. With these apparatus and a binary control thermostat, the CCD temperature is reduced to and maintained at the target temperature of 228°K. At this temperature, approximately two thermal electrons per second per pixel volume are produced.



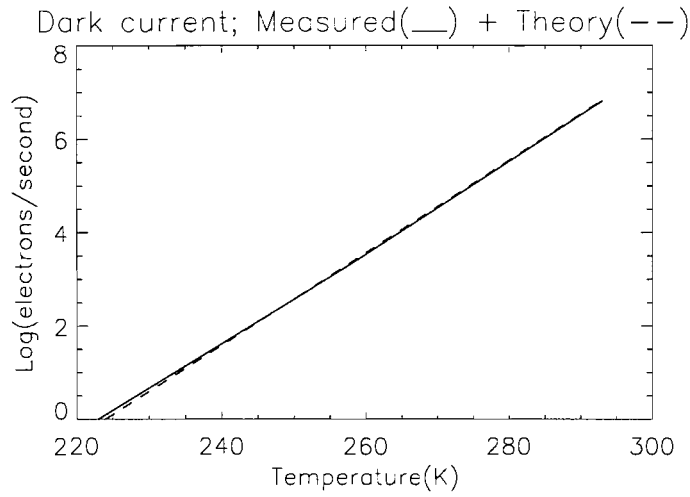


Figure 7.1: A graph of the measured dark current of the Boston CCD at three temperature plotted with the the theoretical relation between dark current and temperature.

## ICCD

The ICCD unit has a peltier thermocouple, coupled to a refrigeration unit using air as its cryogen. The cryogenic unit is able to reduce the CCD temperature to approximately  $30^{\circ}\text{K}$  below the ambient room temperature. Thus the detector is cooled to a temperature of  $260 \pm 3^{\circ}\text{K}$ . The  $\pm 3^{\circ}\text{K}$  error represents the fluctuation in room temperature between  $287^{\circ}\text{K}$  and  $293^{\circ}\text{K}$  brought on by changes in external temperature. Referring back to the instrumentation chapter, we note that the primary source of dark current comes not from the CCD unit, but the intensifier. The thermal noise generated in the bi-alkali photocathode is identical in origin to that of the CCD silicon substrate. The exception is that electrons freed by photocathode phonons are multiplied through the photomultiplier and collected in the CCD, just like the photoelectrons. Both the photocathode and the CCD are cooled to reduce thermal noise.

## Dark Current Variance

The random nature of the thermal electron production process means that the population is governed by Poisson statistics. The variance of phono-electron numbers in each pixel is well described by equation 7.2.

$$\delta\Omega = \sqrt{\Omega} \quad (7.2)$$

where  $\delta\Omega$  is the variance in the thermal electron population  $\Omega$ . The dark subtraction process cannot remove this quantum noise and it is to reduce  $\Omega$  and thus  $\delta\Omega$  that the detectors are ultimately cooled. All modern detectors constructed for low light imaging are cooled to remove thermal vibration from the photosensitive media.

Once the detector temperature is lowered and stabilised to its target value, the CCD can be used for observation. Data frames and dark frames, both integrated for time (t), can be acquired. Figure 7.2 is a dark frame integrated for a time of 10 seconds by the ICCD detector at a temperature of  $260\pm3^\circ\text{K}$ .

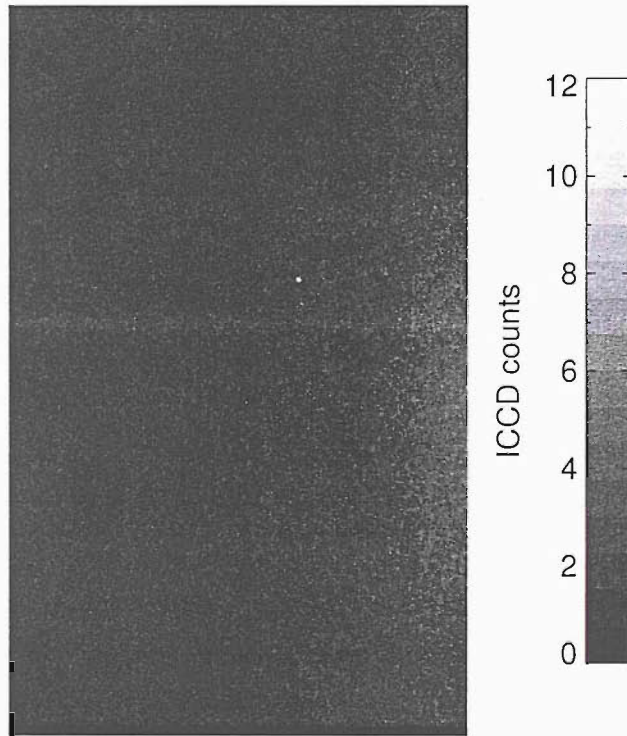


Figure 7.2: The figure shows an unexposed ICCD frame, integrated for 10 seconds. The dark noise, represented by the pixel counts in the array are shown on the colour scale bar to the right. This count range comes from the 8-bit ICCD pixel range.

Considered individually, the pixel population in figure 7.2 has a mean value of  $2.26\pm0.45$  counts. This mean value is an acceptably low thermal noise; however, the variance is disproportionately large. This variance ( $\pm0.45$  counts) is primarily due to the anisotropy of the frame and only a

small part of it is due to the thermal noise variance. There is a clear increase in pixel counts near the centre of the right edge of the frame and to a lesser extent in the corner below it. This 'hot spot' is a long standing flaw in the ICCD unit, in all likelihood caused by a thermal leak or cooling flaw in the intensifier. The intensity of this hot spot is time dependent, a fact that the experimenters were not aware of while the data was taken. This time variance makes the intensity of the flaw impossible to estimate in the data. The difficulty in finding a solution to this problem is exacerbated by having only a single month of ICCD data. Subtracting the dark frame from the data effectively removes these hot spots if the intensity of the hot spot is approximately the same in both the dark, flat and data frames. When this is not the case and the data frame hot spot is dimmer or brighter than that in the dark and flat frames, the only solution is the avoidance of pixels within the problem area. Note that the hot spot areas have a higher thermal variance. These problem pixels are defined as having greater than 201 counts in the horizontal/spatial dimension in the hydrogen filter, greater than 209 counts in the  $N_2^+ 4709 \text{ \AA}$  filter and pixels greater than 220 counts in the  $N_2^+ 4652 \text{ \AA}$  filter.

Another feature to note in figure 7.2 is the bright dot, up and right of the frame centre. This intense little spot, peaking at 12 counts, the brightest pixel in the frame, is produced by a cosmic ray interaction with the CCD. As the dark frame is a measurement of the individual pixel variance, filtering the frame for highly deviant pixels is not desirable. This being the case, each dark frame used as a pixel dark current estimate to be subtracted from the data is an average of seven or more dark frames. While this does introduce a slight error via these cosmic ray counts, this is preferable over a systematic error introduced via erroneous data manipulation. As well as minimising the effects of cosmic rays, the averaging process primarily minimises the variance of the average dark frame and therefore the variance introduced when it is subtracted from the dark frame. To perform this process,  $N$  dark frames are integrated and averaged to create a dark frame. For this thesis  $N \geq 7$  to create well averaged cleaning frames. The amount of variance in each individual dark frame is described by equation 7.2 but this variance is reduced by a factor shown in equation 7.3 in the average dark frame.

$$\delta\Omega_{Av} = \frac{\sqrt{\sum_{i=1}^N (\delta\Omega_i^2)}}{N} \quad (7.3)$$

Given that the CCD temperature ( $T$ ) is approximately constant during the integration time of the  $N$  dark frames, the variance of each dark frame is approximately equal to the other  $N-1$  dark frame variances. This gives us equation 7.4 which equates each of the  $N$  dark frame variances

to the mean of all  $N$  variances,  $\Delta\Omega_T$ .

$$\sum_{i=1}^N (\Delta\Omega_i^2) = N(\Delta\Omega_T^2) \quad (7.4)$$

Combining equation 7.3 and equation 7.4 the variance of the averaged dark frame can be written as equation 7.5.

$$\Delta\Omega_{T,Av} = \frac{\Delta\Omega_T}{\sqrt{N}} \quad (7.5)$$

where  $\Delta\Omega_{T,Av}$  is the noise of the averaged frame of pixels for a given temperature  $T$ . Thus, the variance of an average dark frame produced from  $N$  dark frames is reduced by a factor of  $\sqrt{N}$ . Equation 7.5 is redefined in equation 7.6 to consider each pixel, positioned at  $(x, y)$  on the array, as an individual detector.

$$\sum_{x,y} \Delta\Omega(x, y)_{T,Av} = \sum_{x,y} \frac{\Delta\Omega(x, y)_T}{\sqrt{N}} \quad (7.6)$$

The data displayed in this thesis were treated with averaged dark frames comprised of seven or more dark frames. Figure 7.3 is an example averaged dark frame created from the dark frame in figure 7.2 and six other dark frames acquired.

Note the hot spot is visible on the right edge of the frame. The brightness of the spot is considered constant on time scales of less than three minutes. Given that the one of the detectors used has already begun to decay, it is reasonable to assume that all detectors will change and degrade over days, weeks, months and years. Therefore it is important to acquire dark frames regularly as part of our experimental procedure, capturing them several times during our observation period. These frames will then provide an estimate of the dark current in the data as close as practically possible to the time at which the data was acquired. In addition, these frames along with the flat-fields, will provide an instrument performance benchmark. Over a long period of time a continual record of such frames will provide a reference from which to identify problems in the instrument.

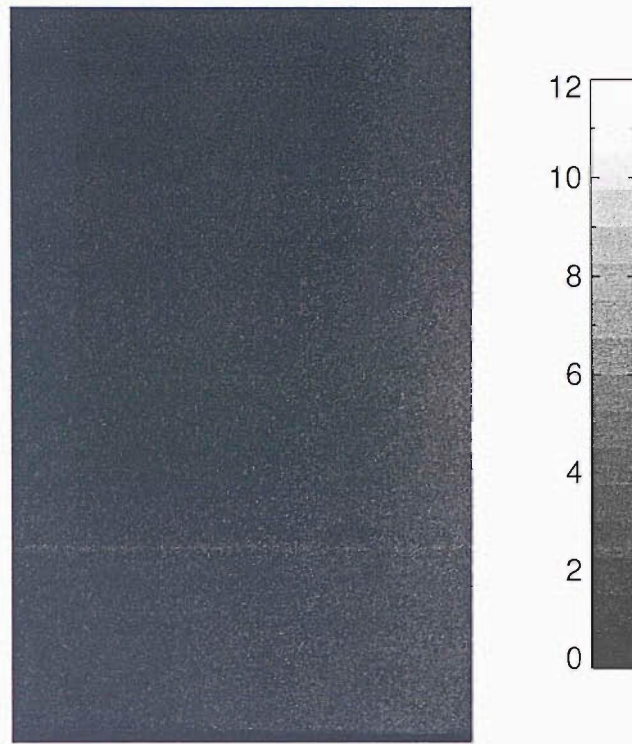


Figure 7.3: The figure shows the average of seven dark frames, each integrated for 10 seconds. The colour scale used in figure 7.2 is retained to display the difference between this averaged frame and the original 10 second integration.

### 7.1.2 Read Noise

The read noise is a broad heading for the current added by the control circuitry in a fixed pattern on the CCD during the charge transfer from the pixel array to digital memory [Janesic et al. (1989)]. The magnitude, form and variance of this read noise are a function of both the speed at which the data is read out from the CCD chip and the design and quality of the detector. Reduction of this unwanted data component is achieved by increasing the readout time or purchasing a detector with higher quality read out electronics. Increasing the readout time reduces the data observation time and a practical balance between lost observing time and readout noise is necessary.

The Boston CCD detector has high quality electronics and has been engineered to produce a readout component of only four electrons per pixel (rms), when reading out at a rate of 50,000 pixels per second. While the noise is very low, the readout time was over twenty seconds for each exposure. Unless the exposure was a very long integration, using this readout method intro-

duced an impractical observing time overhead. To achieve a low noise readout in an acceptably short time, CCD control electronics can 'bin' a number of pixels together as a larger super-pixel. This reduces in the number of pixels to read out and thus the readout time. For example, for an observation of proton aurora, the super pixel might consist of a ten spatial pixels by one spectral pixel (the spatial structure of proton aurora exists at much larger scales than 10 pixels can capture). This reduces both spatial resolution and the readout time by a factor of ten, while maintaining the important spectral resolution. For an array binned into four-pixel super-pixels, with a readout speed of 50,000 pixels per second, this introduces a read noise of four electrons per pixel while the array takes just over ten seconds to read out.

This readout noise can be measured directly by examining a zero-length CCD exposure, although the same noise exists in a dark frame so this measurement is for reference and not used for data reduction.

### 7.1.3 Removing the Dark Frame

The dark frame is created through integrating the unexposed CCD detector at temperature ( $T$ ) for time ( $t$ ). This dark frame is then a measurement of the approximately constant noise sources within a data frame integrated for time  $t$  by a detector at temperature  $T$  and read out using the same readout speed/method. Multiple dark frames are averaged to provide a more accurate measurement of this dark current and read noise. All frames of data or flat-field response should have the dark frame subtracted before any other treatment is applied. The process of subtracting the dark frame from the data frame, pixel by pixel is described by equation 7.7.

$$\sum_{x,y} Result(x,y) = \sum_{x,y} (Frame(x,y) - Dark(x,y)) \quad (7.7)$$

where (x,y) are the ordinates of a detector array x pixels by y pixels.  $Frame(x,y)$  represents the array from which the  $Dark(x,y)$  is subtracted.  $Result(x,y)$  is the processed data frame with the systematic read noise and dark current removed and the Poisson variance of the averaged dark frame added.

## 7.2 Flat-Fielding

The flat-field response of the instrument is measured by filling the instrument field of view with a homogenous, isotropically emitting, spectrally featureless light source and recording the instrument response for a given integration period. The instrument response to the flat-field provides information on the light detection capability of the spectrograph across the whole CCD chip.

### 7.2.1 Natural Vignetting

The flat-field response measures the natural vignetting present in the spectrograph optics. The centre of the light path through the spectrograph optics and onto the center of the CCD is defined as the optical axis of the spectrograph. The effect of natural vignetting is a decrease in CCD illumination as a function of distance from this optical axis centre point. Distance is more correctly considered as an offset angle  $\rho$  from the optical path.  $\rho$  is the parameter governing the drop off in illumination. The inverse square law introduces another factor of  $\cos^2(\rho)$  to the intensity arriving on the image from the lens. Lambert's law introduces a further  $\cos(\rho)$  as does the reduction of the lens pupil area from the perspective of the image point  $\rho$  is directed toward. These factors combine to form the relation in equation 7.8.

$$I_P = I_0 \cos^4(\rho_P) \quad (7.8)$$

where the subscript P denotes a point on the image plane and the respective pixel on the detector. This natural vignetting effect is the cause of the fall off of illumination toward the corners of the image array in figure 7.4.

### 7.2.2 Rectifying Pixel Performance Variance

Even though pixels have an identical construction, individual pixel performance has a degree of variation. The response frame to the flat-field lamp, or the 'flat-field' as the response frame is more commonly called, is a measurement of the sensitivity, dynamic response, illumination, fixed pattern intensification noise and recording ability of each pixel within the array with respect to the other pixels in the array. That is, the flat-field of  $x$  by  $y$  pixels shows how each pixel  $(x,y)$  measures a fixed light value in comparison with the rest of the  $x$  by  $y$  array. Normalisation of



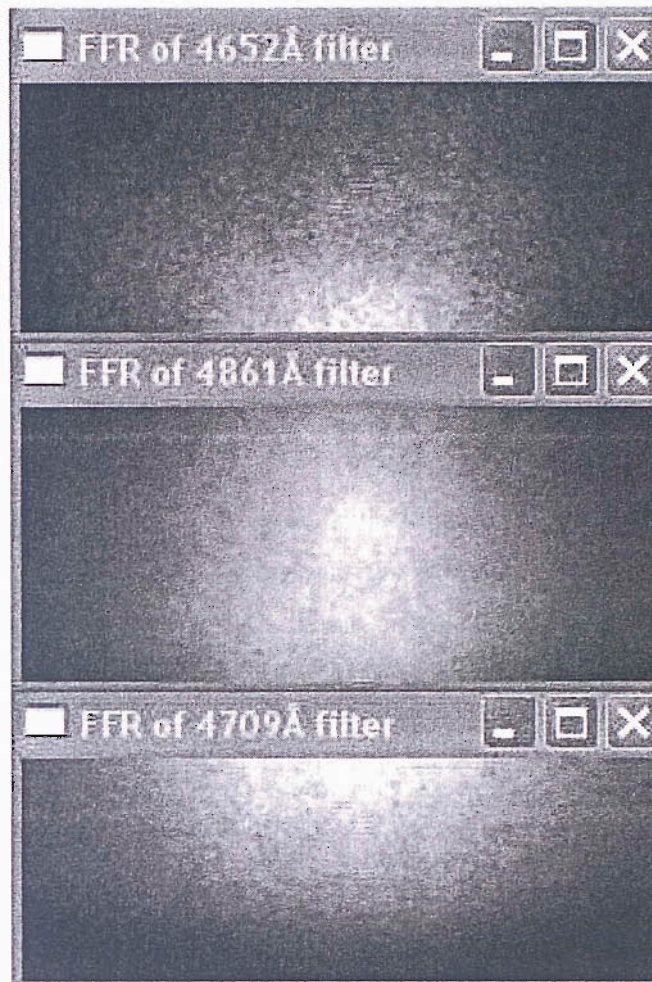


Figure 7.4: Shows the separate spectrograph filter responses to the flat-field lamp input. Note the drop in intensity toward the corners of each filter window due to natural vignetting. Each filter is plotted on a separate intensity scale for contrast, the window headers describe the filter being displayed.

this flat-field response represents the relative light measuring ability of each pixel, on a scale of  $P_{MIN}/P_{MAX}$  to 1.0. Interestingly, the inversion of this array of pixel performance factors forms a rectification matrix, an array of factors to justify the light sensitivity of each pixel throughout the array. For a constant, uniform flat-field source  $I_0$  filling the entire field of view



of the instrument, the flat-field response of the instrument  $A(x, y)$  is a direct measurement of the light response of each pixel  $V(x, y)$ . This concept is expressed in equation 7.9.

$$A(x, y) = I_0 * V(x, y) \quad (7.9)$$

Flat-fields used to manipulate data frames are first averaged in the same way as the dark frames. The quantum/Poisson variance nature of light encountered on the CCD array is written in equation 7.10.

$$v(x, y) = \sqrt{\Upsilon(x, y)} \quad (7.10)$$

where  $\Upsilon$  describes intensity of light recorded in a given pixel positioned at  $(x, y)$  and  $v$  describes the variance in the measurement. Assuming that the amount of light  $\Upsilon$  is constant for a series of  $N$  flat-field response frames, referring to equation 7.4, the noise present in any given pixel  $(x, y)$  is given by equation 7.11.

$$v(x, y)_{Av} = \frac{\sqrt{\Upsilon(x, y)}}{\sqrt{N}} \quad (7.11)$$

Thus, the variance of a average flat-field produced from  $N$  flat-fields is reduced by a factor of  $\sqrt{N}$ . The data displayed in this thesis were treated with averaged flat-fields comprised of seven or more flat-fields.

### 7.2.3 Flat-Fielding Data Frames

The measured pixel response in equation 7.9 is given by  $A(x, y)$ . The normalised array  $N(x, y)$  is created by dividing the measured pixel response by the largest element in the pixel response array  $A_{MAX}$ .

$$N(x, y) = A(x, y)/A_{MAX} \quad (7.12)$$

This normalised array is the shape of the flat-field response. Justification of the unequal array illumination and pixel sensitivity produces a flat, equally intense field of pixels. This is performed by dividing the data array by the normalised flat-field, as shown in equation 7.13.

$$J(x, y) = \frac{Data_{Result}(x, y)}{N(x, y)} \quad (7.13)$$

where dark subtracted data is represented by  $Data_{Result}(x, y)$  and the  $J(x, y)$  array holds the justified or flat-fielded data. Note that although the pixel in the corners of the flat-field receive far less light than the pixels in the centre, they are still just as sensitive.

As previously mentioned, each of the dark current, read noise and fixed pattern intensity response components approximated and removed by dark subtraction and flat-field division have a variance. This variance is by nature impossible to estimate and remove. It exists in all frames measured by the detector and is described by equation 7.14.

$$\sum_{x,y} \sigma(x, y) = \sum_{x,y} (\Delta\Omega(x, y)_T + \sqrt{I_{x,y}}) \quad (7.14)$$

By dark subtracting and flat-fielding the variance in the flat and dark frames is added to that of the data frame. Thus it becomes clear that the dark and flat frames used to clean the data are averaged to reduce the variance introduced into the data to an acceptable level. The noise introduced to the data frame by dark subtraction and flat-field division is the sum of equation 7.6 and equation 7.11 and is shown below in equation 7.15.

$$\sum_{x,y} \sigma(x, y) = \sum_{x,y} \frac{2\Delta\Omega(x, y)_T}{\sqrt{N_{Darks}}} + \frac{\sqrt{Y(x, y)}}{\sqrt{N_{Flats}}} \quad (7.15)$$

This treatment, along with the subtraction of the dark frame, removes all fixed and constant bias from the frame, irrelevant of the sensor measuring it. The ICCD has a time variant 'hot spot' flaw discussed earlier in this chapter. This noise source is not removable using this technique as it appears the hot spot is a thermally derived signal, invariant with ambient brightness on the CCD chip. With enough data, the 'hot spot' could be modelled and subtracted from the data.

Making the assumption that the flat-field lamp emits a constant amount of light, then the lamp can be used to calibrate the intensity response of the spectrograph. The wavelength dependent measurement of the known source can be directly mapped to the known brightness of the lamp for a given wavelength range. This process is more thoroughly detailed in Furniss (2001, HiTIES document).

### 7.3 Quantisation Noise

There is another source of noise to be considered in this section is the dynamic range quantisation noise [Johnston (1989)]. This is a variance due to the data lost in the analogue to digital conversion process. The spatial/spectral quantisation are not affected as the spread functions along both axes are much larger than the pixels, so the data is being over sampled. The digitisation of measured flux does however introduce this dynamic range quantisation noise during the digitisation process. Information theory [MacKay (1995)] states that the error introduced by this signal processing is a function of the number of bits ( $b$ ) in the produced digital data: shown by equation 7.16.

$$\sigma_{A2D} \propto 2^{-b} \quad (7.16)$$

In the intensified CCD, the dynamic range is only 8-bits. For reference, it is difficult to increase the dynamic range of an intensified CCD any higher. For even an 8-bit intensity scale, this source of noise tends to zero and for these purposes, this source of noise is considered negligible. The Boston CCD uses 16-bit dynamic range and thus has negligible quantization noise.

### 7.4 Warping The Pin Cushion

The pin cushion distortion about the center of the spectrograph data frame is formed by the optic path and the aperture slit, detailed in the instrumentation chapter. The distortion is larger on the spectral extremities of the CCD or if the grating is moved near its extremes of motion. The method of unbending the distorted spectral array, supplied by Boston University, is a derivative of the IDL polynomial spatial warping routine `polywarp` [IDL 5.2]. The process allows the user to input the shape of the bent spectral line, and the transform changes it to the input to make a straight line, straightening the frame in the process. This routine is not required when working on spectra acquired from the central CCD region while the grating is positioned in the central point of its range of motion. As all the spectral data in this thesis come from this area, this `polywarp` routine is neither used nor described in this thesis.

# 7.5 ESR Gain Mask For The Video Camera

To aid correlation of ESR data with data from the HiTIES platform, the instrument fields of view are mapped in figure 4.12. However, the radar beam, denoted by an asterisk in that image, is in fact a complex gain pattern defined by the shape of its antenna. By plotting this gain pattern as an image mask, it is possible to view the optical emission the radar would record if it were able to measure optical wavelengths. The sum of this masked image can be directly compared with the range gated electron density measurements around 110 km from the radar. The first step in this process is the production of the radar gain mask with which to reduce the image data. This is done by calculating the gain of the dish for each pixel of the video frame at an assumed altitude. The most complete gain measurement of the field aligned dish is shown in figure 7.5. However it is impossible to map this gain profile onto the image as it was only measured for the East-West line across the dish. A simplified model of the gain profile has been constructed from the E-W gain profile. This simplified gain profile, radially symmetric about the boresite, is displayed in figure 7.6.

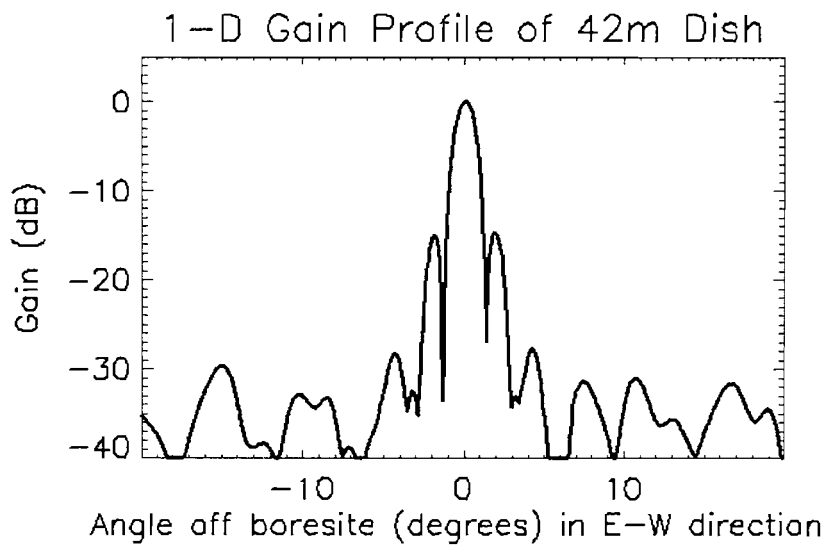


Figure 7.5: Figure showing the measured gain profile across the EISCAT Svalbard radar 42m fixed dish in the East-West direction. The gain is expressed in decibels and the spatial distribution denoted in degrees away from the central beam axis or boresite of the radar along the East-West direction.

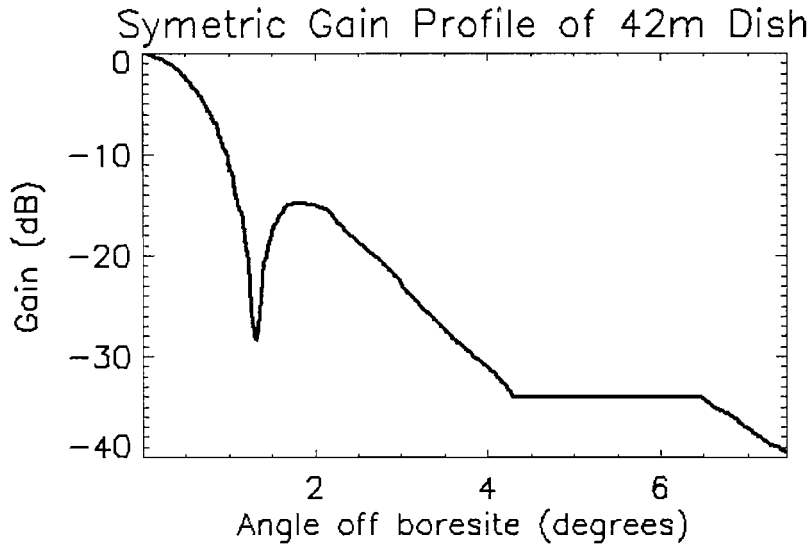


Figure 7.6: Figure showing a simplified gain profile for the EISCAT Svalbard radar 42m fixed dish. The gain is expressed in decibels and the spatial distribution denoted in degrees away from the central beam axis or boresite of the radar.

A video frame mask of the radar gain pattern within the video field of view is constructed using the profile shown in figure 7.6 and knowledge of the orientation of the radar beam with respect to the video frame from figure 4.12. Using figure 7.6 and figure 4.12, a gain mask can be calculated for a given height. This mask will provide insight into what optical emissions originate from the volume sounded by the radar on a sub-second level.

As noted, no radar data were available to compare with the optical data described in this thesis.

# Chapter 8

## Removing External Contaminants from the Data

This chapter details the process of evaluating and removing HiTIES data contaminants originating from an external source. These contaminants are scattered sunlight, cosmic rays and unshifted hydrogen emission.

### 8.1 Removal of sunlight contamination.

#### 8.1.1 Twilight Periods

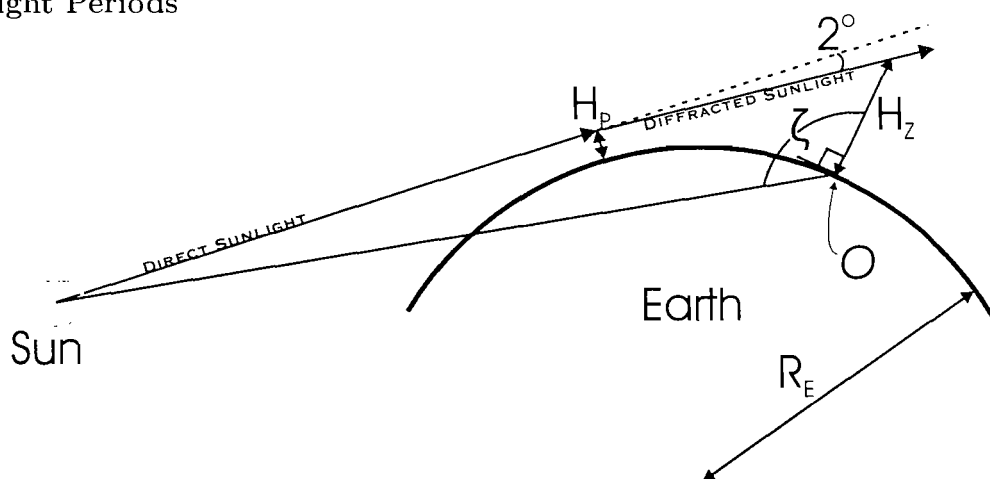


Figure 8.1: The diagram shows the geometric description of the solar zenith angle and shadow height parameters.

As mentioned in the introduction, even at winter solstice every day on Svalbard has a midday period of twilight. For the purposes on this thesis, twilight is defined as the period of time when HiTIES measures Rayleigh scattered sunlight from the atmosphere. Twilight forms a contaminant that is usually two to three orders of magnitude stronger than the emission due to proton precipitation. At local noon each day the spectrograph records data heavily contaminated with scattered sunlight. Figure 8.1 introduces solar zenith angle ( $\varsigma$ ), an angle describing the elevation of the Sun for the observer 'O'.  $H_p$  is the altitude to which the wavelength in question can penetrate the atmosphere. It also shows the sunlight diffraction by the Earth's atmospheric density gradient. The diffraction and refraction about the Earth is measured to be  $2^\circ$  by limb sounding experiments [Christian, priv. comm., 2002]. Shadow height ( $\varpi$ ) is the lowest altitude over the observation point at which direct sunlight can be observed and the effect of the earth diffraction on  $\varpi$  varies with  $\varsigma$ .

Figure 8.2 is the solar zenith angle at noon and midnight at Nordlysstasjonen, showing the periods of direct sunlight, night and twilight over the year. We detect twilight emission in HiTIES measurements between solar zenith angles  $90^\circ$  and  $103.5^\circ$ . This diagram shows that even at mid winter, several hours of auroral observation time are lost each day due to twilight contamination.

Taking an overview of the spectrograph data; the twilight signature drops below the S/N of the spectrograph at a  $\varsigma$  corresponding to  $103.5^\circ$ . The start and finish of the direct sunlight period during the year are used to limit figure 8.3. This figure shows the amount of twilight on each day, as defined by the above criteria.

The twilight incident on Nordlysstasjonen can be more intuitively understood through shadow height ( $\varpi$ ). It is a function of  $\varsigma$  shown in equation 8.1.

$$\varpi = \frac{R_E}{\cos(\varsigma\pi/180 - \pi/2) - 1} \quad (8.1)$$

Examining the twilight variation as a function of  $\varpi$  allows correlation between twilight intensity and the density of atmospheric Rayleigh scattering particles. The twilight limit of  $103.5^\circ$  corresponds to an atmospheric height of approximately 180 km, calculated without considering the light refraction about the Earth. As such, 180 km is the upper limit of  $\varpi$  at cessation of twilight. If the refraction effect is considered and ascribed a maximum value of  $2^\circ$  [Christian,

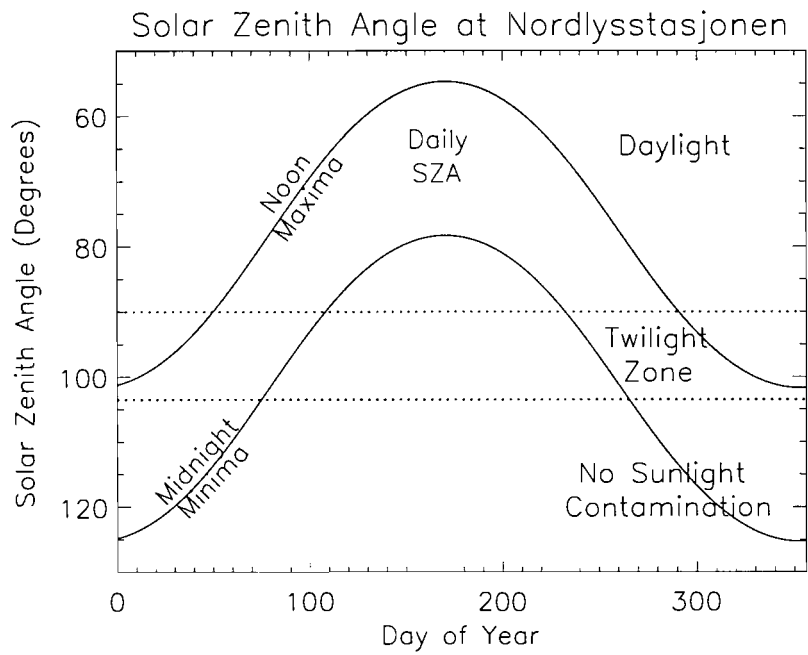


Figure 8.2: The solar zenith angle (SZA) at Nordlysstasjonen over a year. The upper curve represents the SZA at noon while the lower curve represents the SZA at midnight. The two horizontal dotted lines denote the SZA range  $90^{\circ}$  to  $103.5^{\circ}$  over which twilight contamination is observed.



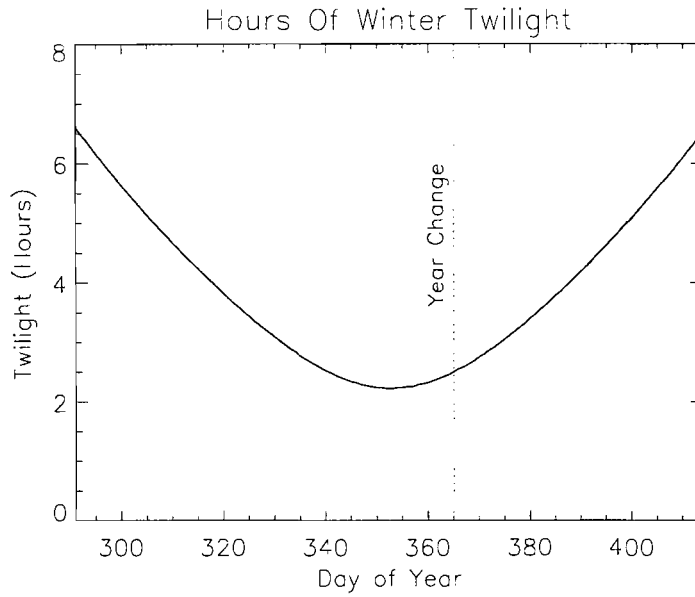


Figure 8.3: This figure shows the number of twilight hours per day during the winter of an ordinary year.

priv. comm.], the minimum shadow height would be 130 km.

### 8.1.2 Twilight Contamination

Data contamination with twilight occurs everyday around local noon, obscuring dayside auroral forms for the most part. This section presents a technique to estimate and remove the twilight contamination, using a few reasonable assumptions. It can be reasoned that the twilight contamination ( $T$ ) present in HiTIES data has just two components: Rayleigh scattered sunlight ( $S_T$ ) and atmospheric emission excited by sunlight ( $A_T$ ), expressed in equation 8.2.

$$T(\lambda) = S_T(\lambda) + A_T(\lambda) \quad (8.2)$$

Most of the contamination is scattered sunlight ( $S_T$ ). This can be more specifically stated as the Fraunhofer spectrum convolved with the Rayleigh scattering function;

$$S_T(\lambda) = F(\lambda) * \sigma_R(\varsigma) \quad (8.3)$$

where  $F(\lambda)$  represents the Fraunhofer spectrum, and  $\sigma_R$  represents the Rayleigh scattering

function given in equation 8.4,

$$\sigma_R(\varsigma) = \frac{8\pi^3}{3} \frac{(m^2 - 1)^2}{\lambda^4 (N(\varsigma))^2} \quad (8.4)$$

where  $N$  represents the number density of atmospheric scattering particles and  $m$  is the atmospheric opacity. The brightness of the spectrum varies as a function of shadow height and cloud cover. Any wavelength dependent effects introduced by changing  $\sigma_R$  are negligible over the 40 Å filter range, thus the shape of the scattered spectrum remains fixed.

The smaller secondary component is atmospheric emission. This contains a number of emissions excited directly or indirectly by sunlight, chemical processes and particle precipitation.

$$A_T(\lambda) = A_{SD}(\lambda) + A_{SI}(\lambda) + C(\lambda) + P(\lambda) \quad (8.5)$$

where  $A_{SD}(\lambda)$  is atmospheric emission due to direct sunlight excitation.  $A_{SI}(\lambda)$  is atmospheric emission due to scattered sunlight and secondary emission due to  $A_{SD}(\lambda)$  emission,  $C(\lambda)$  represents emission due to atmospheric chemistry and  $P(\lambda)$  is emission due to auroral excitation.

These emissions exist over entire HiTIES observable spectrum, and have a range of radiative lifetimes. The complexity of modelling  $A_T(\lambda)$  is compounded by the relatively small body of knowledge on the minor atmospheric emission species. Thus, to estimate  $A_T(\lambda)$  it must first be minimised by careful selection of the investigated spectral range, and crudely approximated. The auroral H $\alpha$  emission lies between 6570 Å and 6530 Å. While this is the brightest emission in the Balmer series, a strong Vegard-Kaplan band lies in the same spectral range. This contaminant cannot be easily approximated and would make accurate profile extraction difficult. The second auroral Balmer line, H $\beta$ , lies between 4870 Å and 4830 Å and this range is free from known atmospheric emission lines. By using H $\beta$  for our measurements, the effects of  $A_T(\lambda)$  are minimised. With the exception of the auroral and atmospheric H $\beta$  emission and in the absence of any contradictory knowledge,  $A_T(\lambda)$  can be considered as a spectral invariant over this range, and to vary directly with solar input.

$$A_T(\lambda) = A(\varsigma) \quad (8.6)$$

where  $\varsigma$  is solar zenith angle. Note that this assumes no long radiative lifetime or chemically

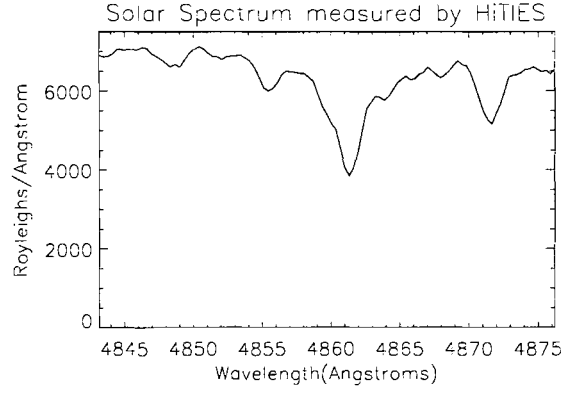


Figure 8.4: Spectrum ( $T(\lambda)$ ) recorded by HiTIES between 08:45 and 10:01 on November 30, 2002.

driven emissions are present in the band, which is not contradicted by the data. This approximation also assumes there are no auroral emissions other than  $H\beta$  in the band.

Substituting equation 8.3 and 8.5 into equation 8.2 we have:

$$T(\lambda) = F(\lambda) * \sigma_R(\varsigma) + A(\varsigma) \quad (8.7)$$

So for a fixed wavelength range, twilight contamination varies with  $\varsigma$ . Note that the overall shape of the twilight contamination spectrum does not vary, only its magnitude varies as a function of  $\varsigma$  and atmospheric opacity. The shape of the twilight spectrum is displayed in figure 8.4. No discernable auroral emission was detected by the instrumentation at Nordlysstasjonen during the integration period of this spectrum. Despite the presence of a thin, broken layer of haze during the integration time, figure 8.4 represents the best measurement of the twilight contamination spectrum ( $T(\lambda)$ ), resolved with the ICCD.

The brightness of the twilight contamination depends upon the atmospheric opacity conditions so is impossible to accurately model the twilight brightness as a function of  $\varsigma$ . Estimation of the twilight brightness, including the effect of atmospheric opacity is achieved by reference to the background level of the data spectrum. Normalising the solar spectrum to the background emission level of the data spectrum provides an accurate method of estimating the amount of solar contamination in the spectrum. The wavelength range of the  $H\beta$  filter selected to be the background area ( $\bar{\Omega}$ ) in the filter is shown in figure 8.5. This range was selected as it is effectively

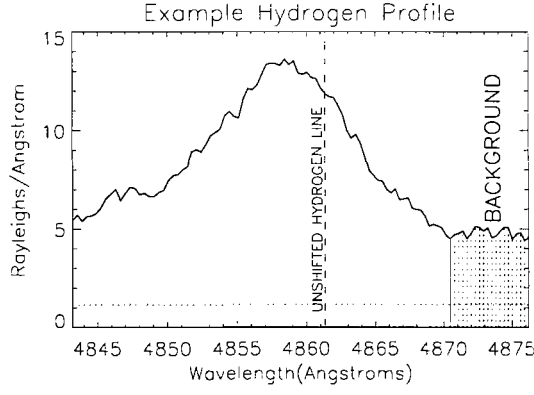


Figure 8.5: An example  $H\beta$  profile. The shaded area indicates the chosen background region of the spectrum.

featureless, thus representative of the background emission underlying the auroral emission.

An estimate of the twilight contamination can be achieved by multiplying the measured twilight spectrum by the factor  $(\phi)$ , calculated in equation 8.8.

$$\phi = \frac{\overline{\Omega_D}}{\overline{\Omega_T}} \quad (8.8)$$

where  $\overline{\Omega_D}$  is the background brightness level of the data spectrum, and  $(\overline{\Omega_T})$  is the background brightness level of the reference twilight spectrum. Note that maximising the wavelength range over which the background is measured minimises the error in  $\phi$ .

Taking a data spectrum ( $D$ ) contaminated by twilight; the twilight can be estimated using the reference twilight spectrum  $T(\lambda)$  and the scaling constant  $\phi$  from equation 8.8. This estimate can then be subtracted from  $D(\lambda)$  to reveal the underlying spectrum ( $R(\lambda)$ ).

$$R(\lambda) = D(\lambda) - \phi T(\lambda) \quad (8.9)$$

Figure 8.6 shows the twilight estimation process and the resulting subtracted spectrum.

The process apparently estimates and subtracts  $T(\lambda)$  accurately, to reveal the much smaller

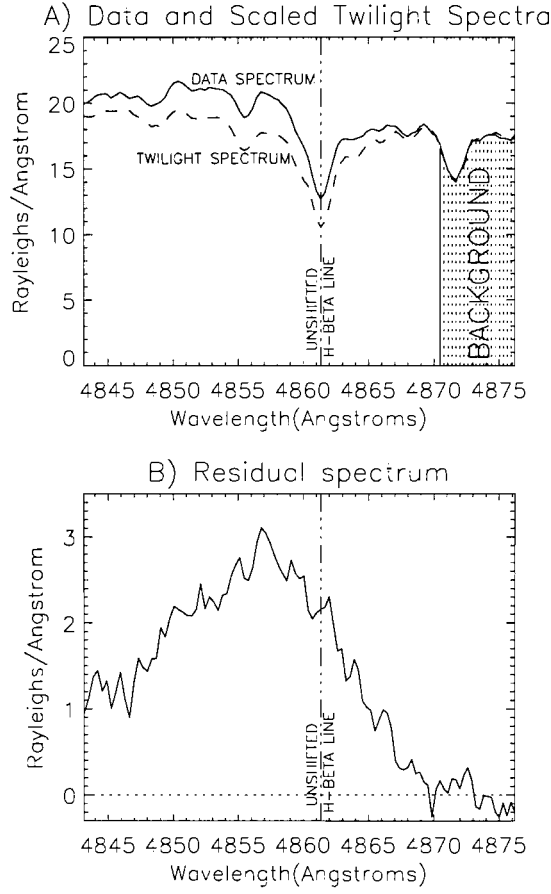


Figure 8.6: A)  $D(\lambda)$ , a 240 second integration beginning at 12:14:32 on 26/11/00, is shown as a solid line.  $\phi$  is calculated and used to scale  $T(\lambda)$ , shown as a dashed line. B) The residual spectrum ( $R(\lambda)$ ) after the scaled twilight spectrum has been subtracted from the data spectrum.

underlying hydrogen profile,  $R(\lambda)$ . Note that  $R(\lambda)$  still has the Poisson variance of the larger initial spectrum after the subtraction.

### Summary of Twilight Subtraction

This technique is a powerful tool for extending the observation period of the spectrograph into the twilight hours. It has the advantage of simplicity and can be implemented as an automated routine.

The technique assumes that the background continuum emission is negligible compared to the twilight contamination, so it may not be applied to data with very small amounts of twilight contamination. If the technique were applied to data with little or no solar contamination, the technique would overestimate the contamination and subtract more twilight spectrum than is present. This overestimation would alias in the subtracted profile as emission in the twilight spectrum absorption lines. Fortunately, almost all of the solar contamination period experienced every day contains twilight much brighter than the background emission level.

The upper limit of this subtraction mechanism has not been encountered. The process will become less practical as the magnitude of the sunlight ( $I_S$ ) quantum variance ( $I_S^{\frac{1}{2}}$ ) approaches the magnitude of the auroral emissions ( $I_A$ ) being measured. This Poisson variance is the ultimate limiting factor; once  $I_S^{\frac{1}{2}} \sim I_A$  then the variance of the sunlight will obscure the auroral spectrum.

A method of increasing this limit is to include a polarizing lens in the optical path. The sunlight scattering mechanism polarizes the scattered sunlight, so a polarizer could be used to selectively reduce the amount of incident sunlight with respect to the incident auroral light. Referring to [Ugolnikov (1999); Ugolnikov and Maslov (2002)], for a viewing elevation of  $81^\circ$ , a correctly aligned polarizer would filter out  $>80\%$  of the scattered sunlight for a solar zenith angle of  $96^\circ$ , even more for angles up to  $90^\circ$ . Of course the polarizer reduces the unpolarized light throughput by 50% so it should only be used when  $I_S > I_A$ , that is, when the improvement to S/N is greater than the loss in S/N caused by introducing it.

## Moonlight

Another problem is data contamination from scattered moonlight. While the moon does not get high enough over Svalbard to enter the spectrograph field of view, moonlight can scatter off cloud and atmospheric particles into the spectrograph aperture. The moonlight contamination spectrum is effectively the same as twilight, and removing moonlight contamination is achieved in the same way as removing twilight. With this de-contamination filter it is possible to observe during full moon periods, again dramatically increasing the annual observation opportunities.

## 8.2 Cosmic Ray Filtering

The name Cosmic Ray event or 'CRE' is the term ascribed to a CCD pixel count that is highly aberrant in time and space. The frame shown in figure 8.7 holds several cosmic ray events marked with 'CRE'.

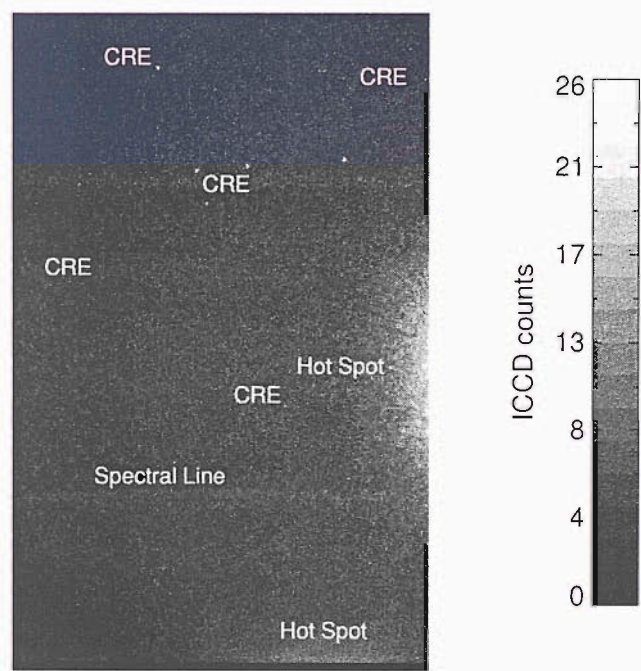


Figure 8.7: A raw frame resolved using the ICCD detector on the HiTIES Spectrograph. The bright points near the 'CRE' denominator are cosmic ray events. The detector also has two large detector flaws marked with 'Hot Spot' on the image. There is also a spectral line present in the lower filter panel.

The particles that cause CRE are primarily the constituents of a particle cascade produced

by a high altitude collision between a  $\geq 3$  GeV particle and an atomic nuclei [Gaisser (1990)]. At ground level, the remaining constituents of the cascade are mostly 1-10 MeV electrons and photons, although some hadrons and muons still exist at this altitude [Grieder (2001)]. Muons are highly penetrative, and the interaction cross section of the particles decreases even further with falling energy. Interaction between the cosmic ray cascade particles and the silicon matrix typically causes a build up of charge in the interaction region, often captured by just one pixel potential well to form the high count pixel signature of a CRE. The strength of a CRE does not necessarily indicate the energy of the interacting particle, just the energy absorbed during the interaction.

Cosmic rays  $< 15$  GeV vary with geographic latitude, although the cosmic ray population peaks above  $70^\circ$  latitude [Neher (1952)]. Cosmic ray intensity varies with viewing direction, local magnetic field strength and orientation, solar shocks [Forbush (1937)], flare events and atmospheric temperature. It is therefore not easy to model.

To register as a cosmic ray event in the spectrograph detector, a cosmic ray shower product must not only penetrate the atmosphere, it must penetrate the 20 mm glass dome of the observation hut, 20 mm of steel spectrograph casing and around 30 mm of optic glass to reach the CCD silicon. While  $\gamma$  and  $\beta$  rays are certainly capable of this, they will suffer very heavy attenuation at the solid barriers. Muons on the other hand are orders of magnitude more penetrative and are thus assumed to cause most of the CRE we detect. The muon count at sea level is 0.52 counts/minute/cm<sup>2</sup>/sterad [Groom et al. (2000)]. These muons only come from the skyward hemisphere and the silicon detector presents an area of approximately 1 cm<sup>2</sup>. The detector is inclined at angle of  $9^\circ$  to the vertical although for the purpose of examining the muon flux from the forward hemisphere there is very little effect from this. The CCD-muon interaction rate is described by equation 8.10.

$$CRE_{Muon} = (0.52)(2\pi)DQE_{Muon}T_{Muon} \quad (8.10)$$

where  $CRE_{muon}$  is the amount of CCD detected CRE due to muons in one minute.  $DQE_{muon}$  is the muon detection efficiency of the CCD.  $T_{Muon}$  is the muon transmission coefficient of the solid barriers mentioned in the above text. Similar equations can be derived for the  $\beta$  and  $\gamma$  rays although  $T_\beta$  and  $T_\gamma$  is assumed to be vanishingly small so these two factors are ignored.



In ICCD arrays, these CRE on the intensifier can form a small group of pixels around a central event point due to a flaw in the intensifier-CCD coupling. This effect is called 'blooming' and while it is difficult to see, it is visible for each of the CRE in figure 8.7. More rarely, this blooming can occur when the CRE energy input frees more electrons than the pixel potential can contain and the superfluous current leaks into the surrounding pixels.

## CRE measurements

Examination of just over two hours (7340 seconds) of ICCD data from the morning of November 30<sup>th</sup> identified 518 CRE. The difficulty in identification of the CREs is that they exist over a very wide range of intensity. The brightest CRE can drastically alter the contrast scale of the frame and the weakest CRE appears as a slightly anomalous pixel if the CCD background is flat. The sample gives a CRE frequency of 4.2 CRE/minute, more than Groom (2000) suggests. An interesting observation during the study may explain this, the CRE were found to group in both frequency and spatial distribution. Many more frames than Poisson statistics can allow, contain twelve or more CRE. It is often the case that the CRE population of a frame are grouped closely on a particular quadrant of the CCD. More intriguingly, a strong CRE will sometimes have one or two smaller CRE clustered around it, within one or two pixels. This overpopulation of CRE with spatial and temporal grouping could be explained by the chip collecting a proximity focused cosmic ray cascade. A nearby collision of a Muon with the optics or steel casing would produce a cascade of particles, some of which would be caught by the spectrograph detector. It is reasonable to assume that these collisions occur and that the cascade particles produced would go on to form counts in addition to the baseline predicted by the Groom (2000) survey. Although the exact number of detector interacting cosmic rays would require a most exhaustive search of the HiTIES data, it seems reasonable that the measured 4.2 CRE/minute are largely derived from cosmic ray cascade particles.

While these CRE are scientifically interesting, when examining the spectral data from the instrument, the CRE counts are simply unwanted noise to be removed. The removal process is a variant of a moving boxcar average. This boxcar technique investigates a particular pixel value by comparing it with the statistical mean of surrounding pixels. The surrounding pixels are selected according to the scheme shown in figure 8.8. The selection shape avoids any pixels

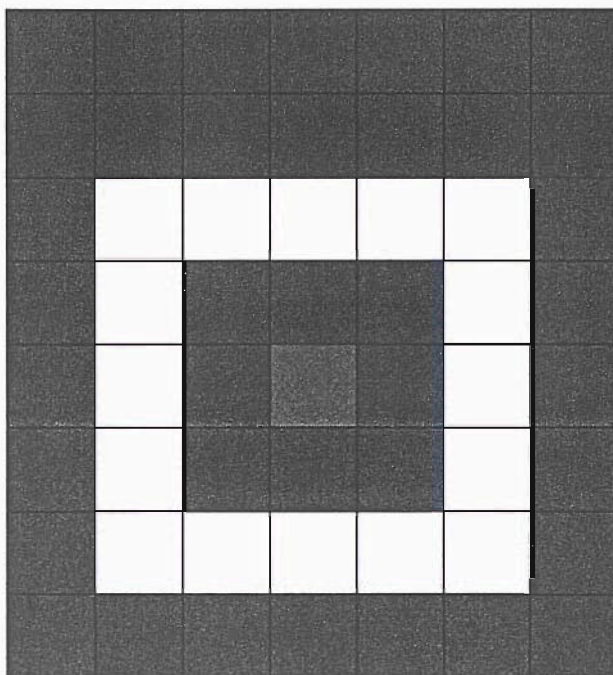


Figure 8.8: A diagram showing a extended boxcar average of this pixel population. This scheme investigates if the central pixel holds a CRE by comparing it to the average the surrounding white pixels. Note that this scheme becomes less effective when the selected pixel is one square from the edge of the array as the size of the pixel population is reduced.

adjacent to the query pixel as blooming invariably causes the CRE to occupy more then one pixel on the ICCD. This scheme is optimised for low count gradient frames like the dark and flat frames and spectrally diffuse line measurements. Spectrally narrow measurements would be better suited to a filter that used four pixels either side of the query pixel on the spatial axis. This filter would not be compromised by bright spectral lines forming a high variance pixel population. The selected pixels are treated as a gaussian distribution and the mean and variance are calculated. If the pixel in question is deviant by more than ten sigma from the distribution mean it is rejected as a CRE and replaced with the mean. This ten sigma threshold requires that in order to be flagged for removal, a CRE be very deviant from the surrounding pixels. Thus this process, while avoiding the removal of all but the most deviant pixels still manages to

typically remove between 30 and 50 pixels from each frame. The filter example shown in figure 8.9 has had 38 pixels replaced. Note, a trace element of some bloomed CREs remain, although much fainter from the smoothing process.

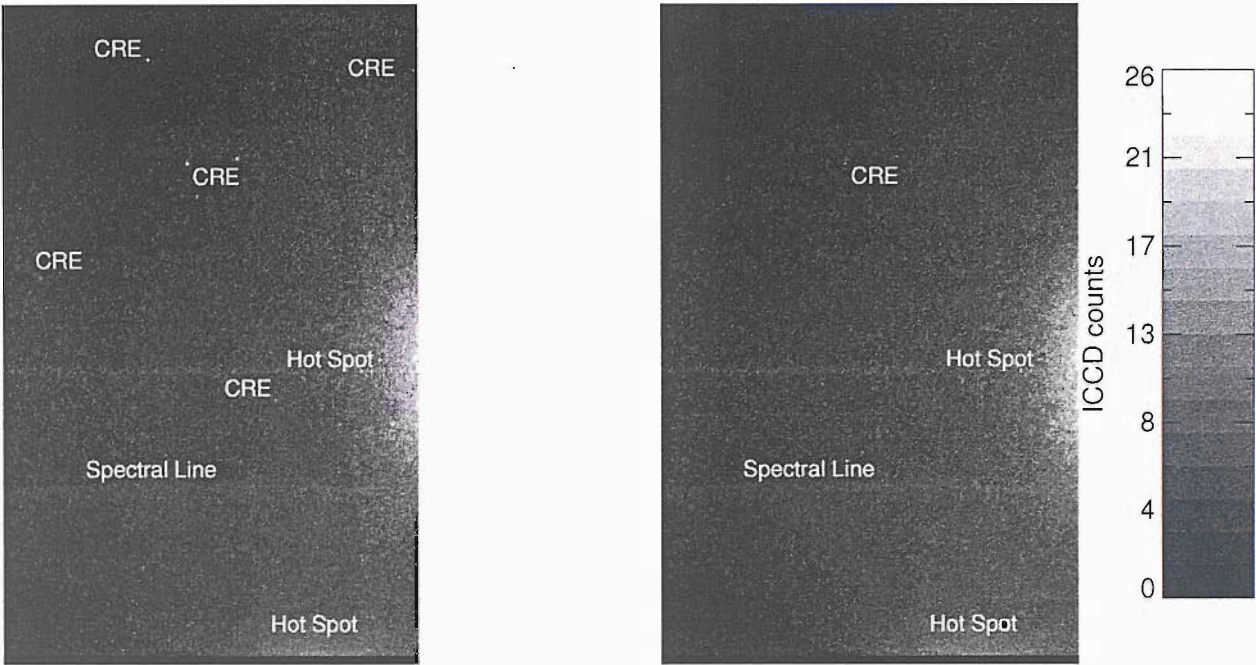


Figure 8.9: A diagram of the action of the CRE filter. The frame on the left contains several CRE. The frame on the right is the same frame after the sigma filter program has smoothed the aberrant values.

### 8.3 Removing the unshifted hydrogen line

Observation of unshifted hydrogen emission is scientifically interesting and constitutes a chapter of investigation in this thesis. However, when examining the Doppler profile of auroral hydrogen it is an unwanted contaminant. To account for this contaminant when analysing auroral hydrogen emission three distinct methods were used, described below.

#### 8.3.1 Gaussian line fit with Bi-Gaussian profile subtraction

The unshifted hydrogen line is essentially a gaussian profile. Fitting a gaussian profile to a high signal to noise data spectrum yields good results. The ideal method, given a high S/N data set is to fit a curve, described in Lummerzheim et al. (2001), plus a smaller gaussian curve to

represent the unshifted hydrogen emission. The description of this line fit is represented by  $I(\lambda)$  in equation 8.11.

$$I(\lambda) = I_L \exp^{-\left(\frac{\lambda - \lambda_0}{\Delta(\lambda)}\right)^2} + I_G \exp^{-\left(\frac{\lambda - \lambda_{H\beta}}{\lambda_{IF}}\right)^2} + I_B \quad (8.11)$$

where  $I_L$ ,  $I_G$  and  $I_B$  are the intensities of respectively: the doppler profile peak minus the background, the unshifted hydrogen emission minus both the background and the doppler profile and the background,  $\lambda_0$  is the wavelength of the peak of the doppler profile,  $\lambda_{H\beta}$  is wavelength of unshifted hydrogen and  $\lambda_{IF}$  is the instrument function (1.26Å in the 38<sup>th</sup> order).  $\Delta(\lambda)$  is given by equation 10.2 from Lummerzheim et al. (2001),

$$\Delta(\lambda) = \frac{1}{2\sqrt{\ln 2}} \left( 1 - \tanh \frac{\lambda - \lambda_0}{\lambda_S} \right) \lambda_B - \lambda_R + \lambda_R \quad (8.12)$$

where  $\lambda_B$  is the halfwidth of the half gaussian on the blue side of the profile,  $\lambda_R$  is the halfwidth of the red side of the profile and  $\lambda_S$  defines the steepness of the step function minimising the unwanted halves of each profile. An example of this fitted line is shown in figure 8.10. The fit is approximately accurate in this case as a strong unshifted hydrogen emission is present in the clearly visible auroral hydrogen emission curve. Unfortunately, the low light regime of dayside aurora and Geocoronal phenomena provides very little signal in the noisy bandpass and a signal to noise ratio such as this is usually only available for integrations of 10 minutes or more. When removing unshifted hydrogen emission from noisier data, this method usually fails to fit accurately because of low signal to noise. At the very least, the profile must be adequately smoothed or integrated before the fitting procedure acquires a satisfactory result, and this removes either spectral or temporal resolution. Even with smoothing or integration, the fit is not acquired reliably all of the time. This is not a robust process and it was concluded that it should be discarded as a survey tool.

### 8.3.2 Ignore the emission

The simplest method is to ignore any unshifted hydrogen emission present. Geocoronal emission of the order of 10 Rayleighs and other possible sources of unshifted hydrogen emission are also small. During the auroral event of November 2000 [this thesis], the unshifted  $H\beta$  emission was typically just 3% of the total auroral emission. This small emission, centered at  $H\beta$ , is often a

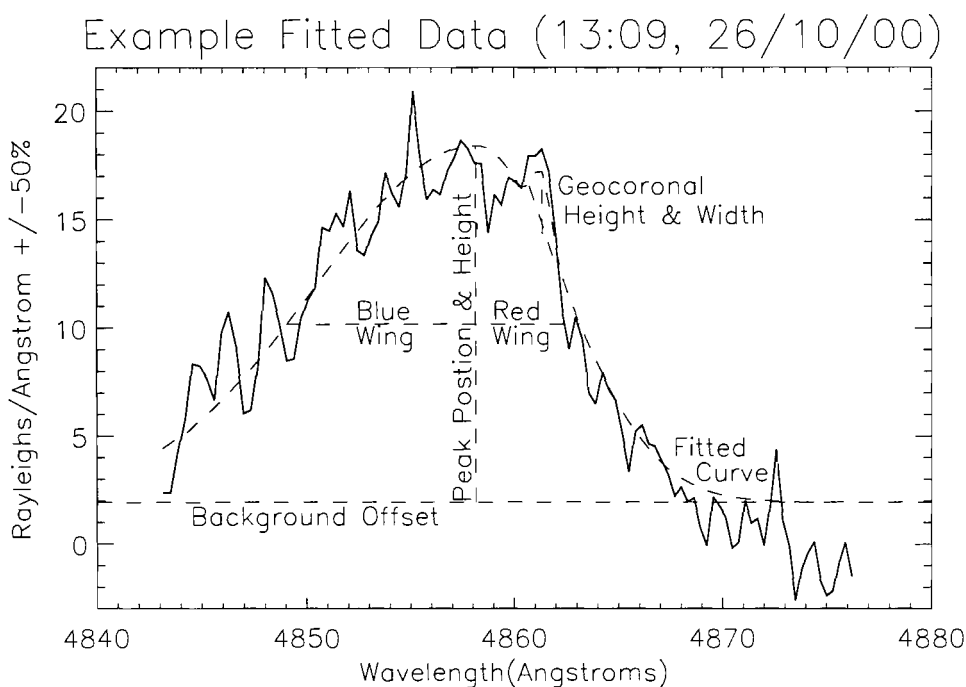


Figure 8.10: An example data spectrum. The dashed line showing the fit  $I(\lambda)$  is drawn over, and follows the data curve. The fitting parameters are described with dashed lines and descriptive labels: Peak Height ( $I_L$ ), Peak Position ( $\lambda_0$ ), Blue Wing ( $\lambda_B$ ), Red Wing ( $\lambda_R$ ), background offset ( $I_B$ ), geocoronal intensity ( $I_G$ ) and line width ( $\lambda_{IF}$ ).

very small bump on the auroral doppler emission profile. It was overlooked for a long period of time. The unshifted hydrogen component may be overlooked when the profile shape is not being fitted and analysed numerically. However, when analysis of profile shape is undertaken, the unshifted component can have a perturbing effect on the fit and a method must be used to remove the unshifted hydrogen contamination.

### 8.3.3 The flat line fit

The most reliable method of removing the hydrogen contamination is a crude straight line fit across the  $H\beta$  line position. This simple method averages pixels 48-50 and pixels 58-60 on either side of the unshifted  $\beta$  line. These two averages were used to draw a line under the unshifted hydrogen emission to approximate its baseline. This linear interpolation then replaces the geocoronal emission in the profile. Effective, reliable and crude, this method is illustrated

in figure 8.11.

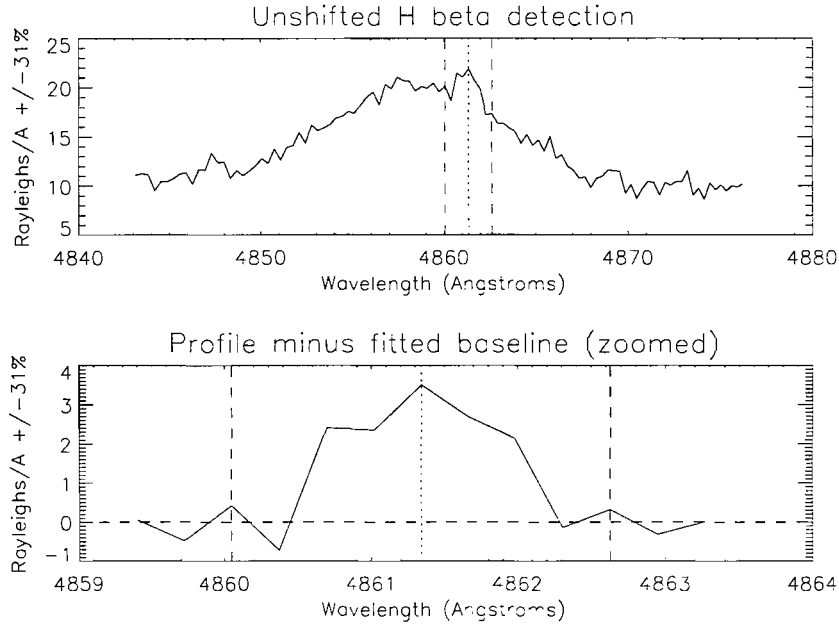


Figure 8.11: The upper graph shows a hydrogen Doppler profile combined with a unshifted hydrogen line. The two vertical dashed lines in this picture show the positions of pixels 49 and 59, the average centers. These two vertical lines are also shown in the second graph and the line drawn between them provides the baseline of this second graph. The unshifted hydrogen emission is neatly extracted from the spectrum to be summed or fitted to.

### 8.3.4 The "targeted" line fit

This method is a development from the flat line fit and the gaussian line fit. First the section of spectrum containing the unshifted  $\beta$  emission is isolated. Then the flat line fit is subtracted from it to leave a spectrum with a flat baseline containing the unshifted  $\beta$  emission. This profile can then be reliably fitted to using the minimised gaussian function shown in equation 8.13.

$$I(\lambda) = I_{Gexp} - \left( \frac{\lambda - \lambda_{H\beta}}{\lambda_{IF}} \right)^2 \quad (8.13)$$

The resulting fit closely approximates unshifted  $\beta$  emission and when subtracted from the data profile effectively removes it. Using the flat line fit as a baseline very slightly overestimates the amount of unshifted hydrogen emission; the flat line is not exactly the doppler curve on which

the line sits and the slight discrepancy aliases as extra unshifted hydrogen emission. The effect is very small however, and this method is reliable for both removing and measuring the unshifted  $\beta$  emission.

## Chapter 9

# Investigation of Atmospheric Hydrogen Emission

### 9.1 Observation

Close examination of data collected on the afternoon of November 26th, 2000, revealed an unshifted hydrogen emission line. Integrating over an hour of data from the end of that afternoon showed a clear detection of a thermal emission line at  $4861.3 \text{ \AA}$ , an unshifted  $H\beta$  emission. This unshifted emission originates from hydrogen at thermal velocities with respect to the Earth.

### 9.2 The possible origin of the emission

The lack of a peak Doppler shift serves to eliminate solar system hydrogen emission, galactic hydrogen emission and extra-galactic hydrogen emission as possible origins for this emission. To emit the unshifted hydrogen line observed, the source hydrogen must be moving with the planet. Hydrogen loosely bound to and moving with the planet is one of the possible definitions of exospheric/geocoronal hydrogen. This exospheric hydrogen is one of two possible sources for this emission in Earth's atmosphere. The second is auroral hydrogen, quenched and deposited around auroral altitudes ( $\sim 110\text{km}$ ), and thermalised with the ambient atmosphere.



### 9.2.1 Exospheric Hydrogen

The exosphere is the outermost layer of the atmosphere and it is characterised by very low density particles on ballistic, orbital or hyperbolic trajectories, and an increasingly dominant hydrogen population with altitude. The exosphere is characterised by this non-collisionless nature, and auroral precipitation does not affect particles in the geocorona.

The hydrogen atoms of the exosphere emit a small amount of Balmer  $\alpha$  emission that can be observed from the ground [Shih et al. (1985); Kerr et al. (1986)]. Balmer H $\alpha$  emission from exospheric hydrogen is excited by sunlight, as described with the following equation.

$$H + \lambda(Ly - \beta) \Rightarrow H * (Ly - \beta) \quad (9.1)$$

The Lyman- $\beta$  ( $Ly - \beta$ ) excited hydrogen atom denoted by  $H*$  then either re-emits the Lyman- $\beta$  photon (equation 9.2) (probability 88%) or a degenerate Balmer- $\alpha$  photon (equation 9.3) (probability 12%) [Nossal et al. (2004); Meirkewitz et al. (2004)].

$$H * (Ly - \beta) \Rightarrow H + \lambda(Ly - \beta) \quad (9.2)$$

$$H * (Ly - \beta) \Rightarrow H * + \lambda(Balmer - \alpha) \quad (9.3)$$

Other degenerate products include H $\beta$  photons. Preliminary evidence suggests the ratio of geocoronal Balmer- $\alpha$  emission to geocoronal H $\beta$  emission might be as low as 10:1, although this relationship requires further study [priv. comm. Nossal].

The brightness of the geocoronal H $\alpha$  emission is between 9-16 Rayleighs

[Fishkova and Marzvaladze (1966)], measured at a latitude of 55°N. A more recent Sondrestrom observation [Kerr et al. (2001a)] from 67°N, observed an average H $\alpha$  brightness of 8 Rayleighs. The distributions and concentrations of H in the auroral zone are poorly known and are subject to two opposing effects. The first is the seasonal interhemispheric flow, it results in a winter bulge of the lighter atmospheric elements. Measurements by the Atmospheric Explorer C [Brinton (1975)] observed this bulge to increase the concentration of hydrogen by approximately 2 at a latitude of  $\pm 68^\circ$ .

Emerich et al. (1976) has published evidence for the second effect, a high latitude depletion of the Geocoronal hydrogen in the winter hemisphere. The winter atmospheric bulge of hydrogen lifts hydrogen high in the polar atmosphere where it is lost up the field lines through charge exchange with  $O^+$ . This hydrogen charge exchange mechanism with ionised oxygen atoms is shown by equation 9.4.



In the polar regions this mechanism is not in equilibrium as the newly formed  $H^+$  escapes up the field lines as polar outflow, making equation 9.4 move to the right. This results in a decrease in hydrogen density with latitude increase above the subtropics [priv. comm. Milward]. Above 500 km this charge exchange between monatomic hydrogen and oxygen depletes the winter bulge from the interhemispheric flow. The hydrogen is depleted to around 75% of the global median density at a latitude of  $70^\circ$  in the winter hemisphere. The Southampton/UCL Spectrographic Imaging Facility (SIF) is situated at  $78^\circ N$  in Nordlysstasjonen and it is assumed that the high latitude depletion of hydrogen atoms through  $H \rightleftharpoons O$  charge exchange [Brinton (1975)] reduces the hydrogen density over the station to less than 75% of the global mean.

### 9.2.2 Thermalised Auroral Hydrogen

The other possible source of hydrogen emission is atmospheric hydrogen, interacting with precipitating particles between 80 km and 300 km. Collisions with precipitating protons, electrons and hydrogen atoms could excite an atmospheric hydrogen atom enough to produce a  $H\beta$  emission.



The small hydrogen density at auroral altitudes is increased by precipitating auroral hydrogen; quenched and deposited at around 120 km, and thermalised with the ambient hydrogen partial pressure.

Differentiation between exospheric hydrogen and thermospheric hydrogen as the emission source might be possible through examination of the emission lifetime and continuity, and correlating emission brightness and temperature with auroral input.

### 9.3 The Omnipresence of Unshifted Hydrogen Emission

The detection of strong unshifted hydrogen emission was at first assumed to be a geocoronal response to the impact of the solar wind shock earlier that day. However, further random sampling of the data also displayed this unshifted line. Thus the hypothesis arose that a small amount of unshifted hydrogen emission is present in every  $H\beta$  spectrum.

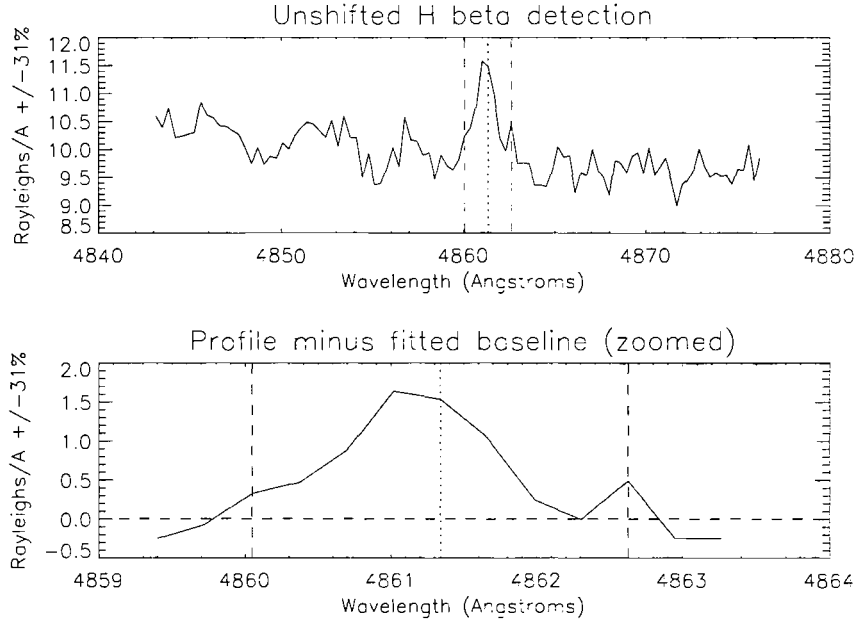


Figure 9.1: This spectrum was integrated through an overcast sky. The unshifted hydrogen line is still clearly visible in the upper spectrum. The dashed lines indicate the extraction mechanism of the unshifted hydrogen emission, detailed in section 8.3. This extracted unshifted hydrogen emission can then be summed or fitted with a gaussian least squares fit as described in section 8.3.3.

To test this, an automated routine was made to examine the data set for unshifted hydrogen  $H\beta$  emission. The routine integrated  $H\beta$  spectra over 30 minute intervals, overlapping adjoining frames by 10 minutes at each end of the integration period. This over-sampled integration scheme was employed to ensure that weak geocoronal brightenings on the order of 5-20 minutes would not be bisected by a sample border and lost in the background noise. It was also noted that over-subtraction of the Fraunhofer spectrum detailed in section 8.1 would alias as unshifted hydrogen emission/absorption. To avoid this confusion, data containing scattered daylight was systematically avoided.

Integrations from this data survey are shown in figures 9.1, 9.2 and also in 8.11 previously described. Note that rejection of 10 second frames, and the overheads involved in frame capture reduce the amount of integrated data in a 30 minute interval to between 20-25 minutes of data. Each integration displayed the unshifted hydrogen emission, at all investigated times of the day, and during all levels of activity. Figures 9.1, 8.11 and 9.2 are a representative sample of this omnipresent geocoronal emission found throughout the data set.

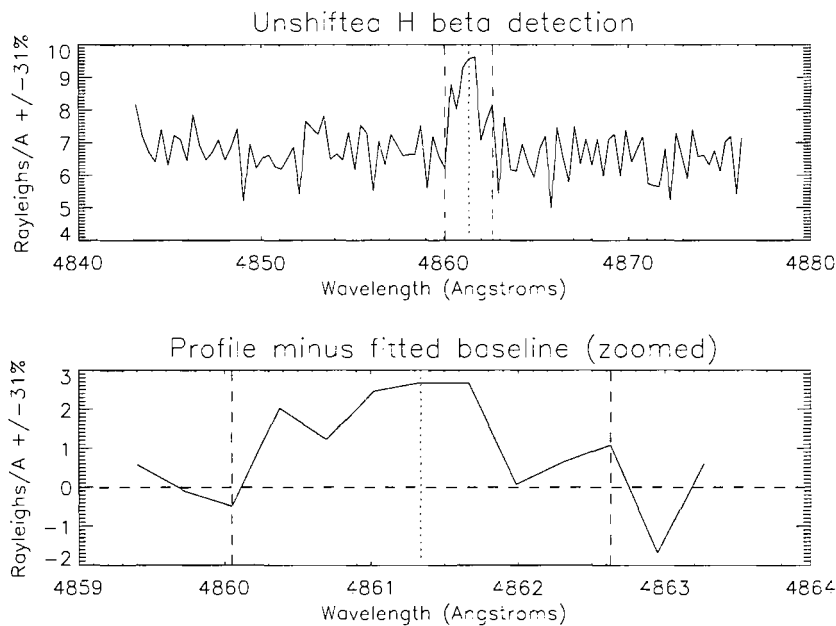


Figure 9.2: This spectrum was integrated during a quiet auroral period. The dashed indicate the extraction mechanism of the unshifted hydrogen emission, detailed in section 8.3, which is a precursor to estimation and subtraction of the emission.

While an omnipresent unshifted hydrogen emission must originate from an omnipresent source, it is possible that a discrete and regular particle precipitation occurring in each of the 30 minute samples, might alias as a omnipresent source.

### 9.4 A Higher Time Resolution Survey of Unshifted Hydrogen

To provide greater insight into the origin of the emission, a higher time resolution search of unshifted hydrogen emission in the data set was conducted. Of the available ICCD data between November 21<sup>rd</sup> and December 18<sup>th</sup> in 2000, only the period between 16:00 UT on November 23<sup>rd</sup>

and 01:30 UT on November 29<sup>th</sup> was found to be suitable. When selecting this period, factors such as coverage, continuity, weather and sunlight/moonlight contamination were considered.

Extracting weak unshifted hydrogen emission from the data spectra at all levels of auroral and unshifted hydrogen activity is a challenging exercise with short integration time data. To avoid skewing the data set routine, a consistent analysis method and fixed integration period had to be used throughout this second data survey. A number of methods of estimating the amount of unshifted hydrogen emission from each spectrum were tried and these are described in detail in section 8.3. The multiple-gaussian line fit described in section 8.3.1 was found to be unreliable when used on spectra with a short (below 10 minutes) integration time, as was the simpler method in section 8.3.4. The straight line fit described in section 8.3.3 was crude, but reliable even on the lowest resolution data integrated for just 4 minutes.

The results of this data spectra survey are presented in three sections. The first is the spectral analysis of the unshifted H $\beta$  line emission. The second is the analysis of the general temporal behavior of the emission. The third part presents the investigation of the unshifted hydrogen emission response to an intense auroral hydrogen precipitation event on November 26<sup>th</sup>, 2000.

#### 9.4.1 Unshifted Hydrogen Line Analysis

The emission line is seen to peak at the wavelength of H $\beta$ : 4861.3 Å in most of the recorded data. Statistical analysis of the surveyed data displayed in figure 9.3 showed an average emission of  $2.0 \pm 1.5$  Rayleighs, where the error is derived from the 55% sample variance and brightness scale error.

The Abustuan survey between 1956 and 1962 from 55°N measured H $\alpha$  emission in the range 9 to 16 Rayleighs. The hydrogen depletion over Svalbard will reduce this to at most 6 to 11 Rayleighs. If the H $\alpha$ :H $\beta$  ratio is the same for geocoronal emission as it is for auroral emission, then this survey indicates we should see H $\beta$  geocoronal emission of between 2-4 Rayleighs at most. As previously stated, [Nossal et al. (2004)] indicates the H $\alpha$ :H $\beta$  ratio is larger than 3:1, perhaps as large as 10:1, indicating a H $\beta$  geocoronal emission of between 0.6 and 1.1 Rayleighs. Combining these two estimates, the average geocoronal H $\beta$  emission over Svalbard should lie between 0.6 and 4 Rayleighs. Our average H $\beta$  brightness measurement of  $2.0 \pm 1.5$  Rayleighs, is consistent with this estimate.

The line profile is symmetrical with the full width-half maximum of the fitted line equal to

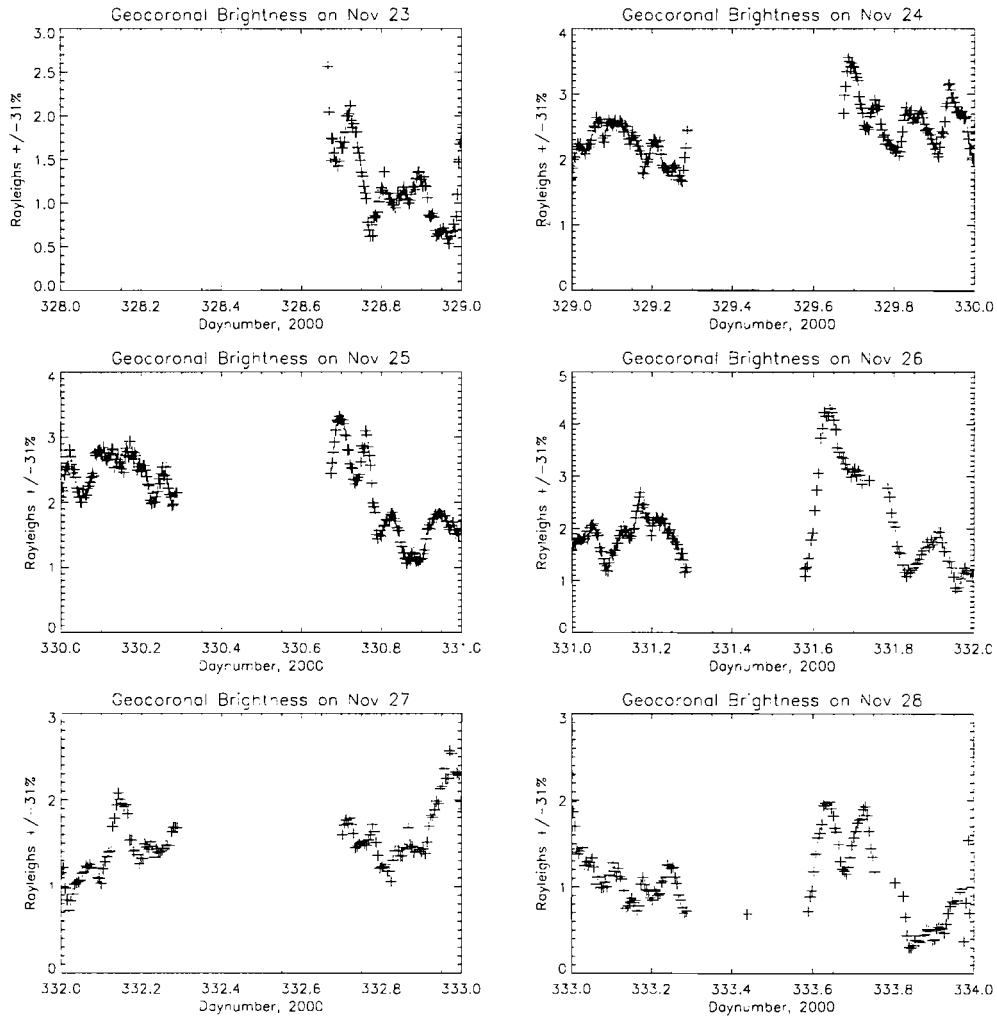


Figure 9.3: The graphs display the total  $H\beta$  brightness of the Geocorona from the data set gathered between 16:00 on November 23<sup>rd</sup> and midnight on November 28<sup>th</sup>. The graphs are plotted against decimal day in UT.

$1.20 \pm 0.07 \text{ \AA}$ . This line-width did not vary throughout the survey and is consistent with the instrument function of  $1.26 \text{ \AA}$  in this diffraction order. Kerr et al. (1986) reports a vertical velocity of around  $\pm 5 \text{ km/s}$  ( $0.08 \text{ \AA}$   $H\beta$  Doppler shift) from geocoronal hydrogen Balmer  $\alpha$  line profile analysis of emissions from the collisional particle distribution at exobase, at an altitude of around 500 km. Most models and measurements of hydrogen temperature at the exobase over the last 30 years indicate that it is just over 1000 K. Analysis of the originating particle distribution using thermal line-width analysis of the HiTIES data set is not possible with our spectral resolution of  $1.26 \text{ \AA}$ .

### 9.4.2 Temporal Behavior of the Unshifted Hydrogen Emission

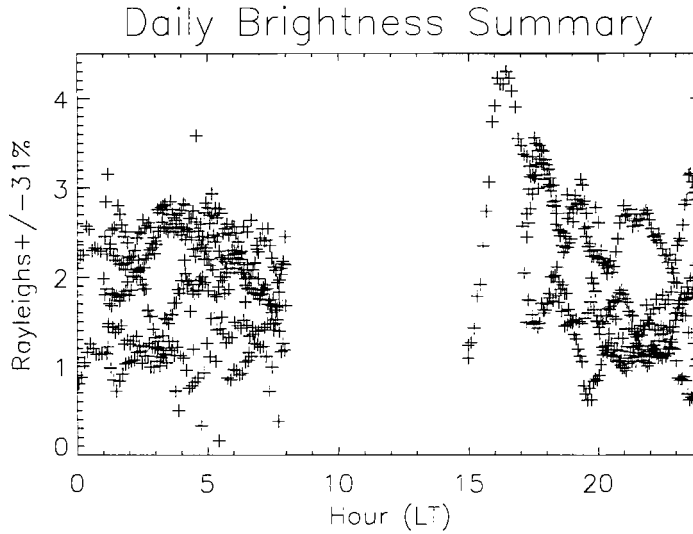


Figure 9.4: The Geocoronal data gathered between 16:00 on November 23<sup>rd</sup> and 01:30 on November 29<sup>th</sup>, plotted on a 24 hour axis.

A summary plot of the survey data set is shown in figure 9.3. These plots show the brightness of the unshifted hydrogen emission on each day of the survey. Note that data before 14:00 UT are discarded due to sunlight contamination and only a limited quantity of data exists to describe the 14:00 UT to 16:00 UT period. Shih et al. (1985) find a H $\alpha$  diurnal variation of the order of 10% with maxima and minima occurring at 04:00 LT (02:56 UT) and 16:00 LT (14:56 UT) respectively, a maxima and minima result supported by many other publications [Kerr et al. (1986), Kerr et al. (2001a)]. Assuming that the variation of H $\alpha$  emission mimics that of H $\beta$  emission, our results are different from those reported by Shih et al. (1985). However like Shih, we see a stable morning maximum; 60% of the fully sampled morning periods peak at  $03:50 \pm 00:05$  LT. As this particular data set spanned just a week, seasonal conclusions were not possible.

Unlike the diurnal shadow height of the observatories used by Kerr and Shih, our shadow height only varies between 200 km and 1400 km as shown by figure [?].

As the bulk of the hydrogen geocorona is above this height, constantly in sunlight, our geocoronal emission does not vary by much at all.

From figure 9.4, and discounting the errant spike of the shock event, a daily maxima can be seen

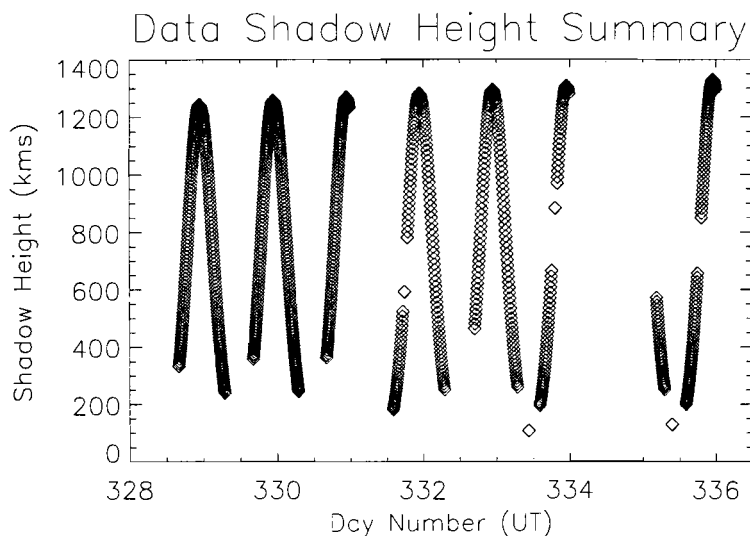


Figure 9.5: The shadow height of each geocoronal data point gathered between 16:00 on November 23<sup>rd</sup> and 06:30 on December 1<sup>st</sup> plotted vs day number.

to occur in the afternoon sector between 17:30 LT and 18:00 LT. The data set shows a variance of approximately 50% in the unshifted hydrogen emission under non-auroral conditions. This is almost certainly a function of the variable seeing conditions at our site. This variation could be investigated more accurately using a variant of the star calibration process described in chapter 6. The technique provides a method of periodically updating the observation efficiency, including opacity losses, and should provide a more accurate estimate of the brightness variation in the unshifted H $\beta$  emission.

## 9.5 The unshifted hydrogen emission response to the shock on November 26th, 2000

The response of the unshifted hydrogen emission to auroral precipitation is illustrated clearly in figure 9.6. This graph shows two traces, the solid line represents the brightness of auroral emission and the dotted line represents the brightness of the unshifted hydrogen emission. These traces are shown on a normalised brightness axis in order to compare the temporal variation of the two traces.

From figure 9.6 the unshifted hydrogen emission clearly responds to auroral brightness or a



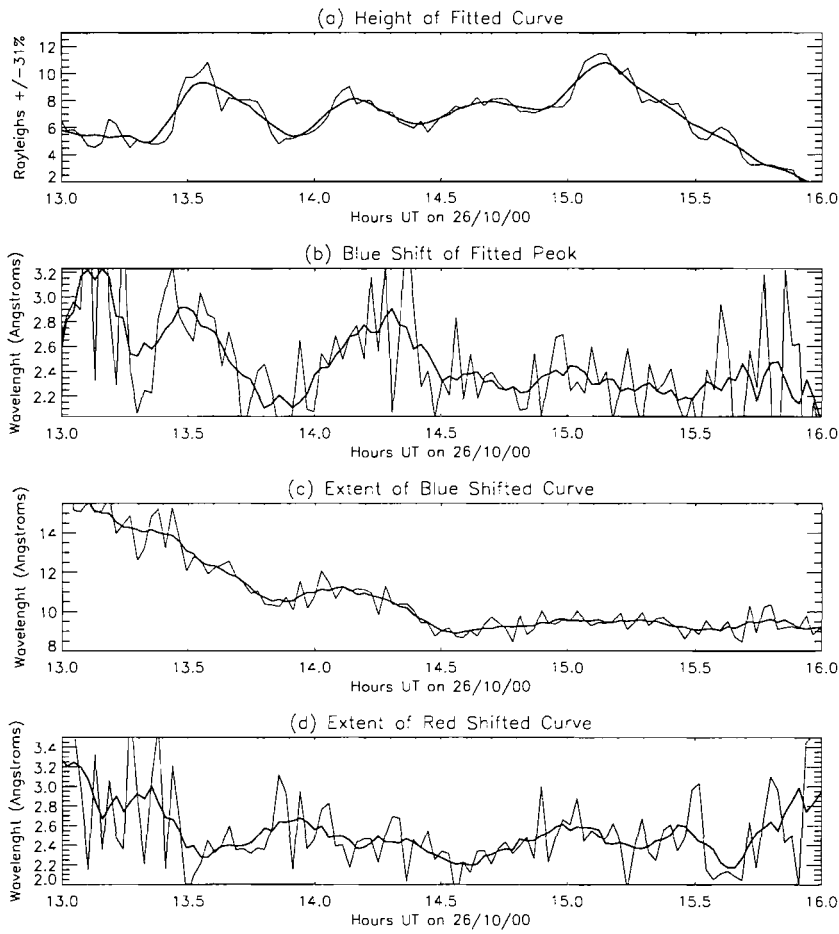


Figure 9.6: This plot shows the normalised brightness of auroral  $H\beta$  and unshifted hydrogen emission over the seventeen hour period between maintenance times from 12:00 UT on November 26<sup>th</sup> to 05:00 UT the following morning. The solid line shows the normalised brightness of  $H\beta$  emission and the boxes joined with a dotted line show the normalised brightness of the unshifted hydrogen emission. There is a factor of 30 between the two brightness.

physical process linked with auroral emission. There is no correlation between the geocoronal emission and hydrogen energetics, represented by the extent of the Doppler blue shift of the profile. To investigate this response an understanding of the dynamics of hydrogen deposition should be developed. Auroral protons are most likely to be deposited at an altitude of about

120 km. Atmospheric conditions at these altitudes is collisional and the horizontal winds tend to move tidally, northward during the day and southward during the night [Dobbin, private communication], with a speed of the order 15 m/s, increasing with altitude. At these low densities, atomic motion has a more dispersive effect than the tidal winds. The half-life of hydrogen at these altitudes is several months to a year [Brasseur and Solomon (1984)]. [Rees (1989)], table A1.3, indicates the column content of hydrogen above 100 km is approximately  $3 \times 10^{13} \text{ cm}^{-2}$ . An order of magnitude hydrogen input estimate is  $1 \times 10 \text{ cm}^{-2} \text{ s}^{-1}$  [Rees (1989)] assuming that all protons are stopped as neutral hydrogen above 100 km. This implies a time scale of around an hour to double the initial hydrogen density above 100 km. In principle then, the number density of H above 100 km can thus be greatly affected by prolonged proton precipitation, although diffusion will disperse this additional hydrogen in a few hours.

Figure 9.6 holds several interesting features. The sharp initial rise of the unshifted hydrogen emission is due to the fading effect of solar contamination. Sunlight contamination is present as it cannot be removed from geocoronal investigation data without the possibility of introducing an effect that could alias as geocoronal emission. As it is, the H $\beta$  absorption line in the Fraunhofer spectrum subtracts from the H $\beta$  emission from the thermalised hydrogen until the scattered sunlight fades to zero just before 15:00 UT.

The auroral peak just after 15:00 UT is matched exactly by a peak in the unshifted hydrogen emission. The auroral H $\beta$  emission peaks at 450 R, two orders of magnitude larger than the unshifted hydrogen emission peak at that time. This indicates the H $\beta$  auroral particle collision excitation mechanism acting on hydrogen at auroral altitudes is responsible for this emission. To further qualify this, the sunlight did not vary to produce this effect, and the collisional excitation of hydrogen is only possible below the exobase, with most collisions occurring at around 120 km. Any H $\beta$  emission in response to precipitating particles is immediate.

Elevated levels of hydrogen through auroral proton deposition strengthen this emission response. Doubling the hydrogen at this altitude through auroral influx should double the emission response to auroral precipitation, although this is a difficult result to extract from this data set due to solar contamination.

Auroral activity quickly decays to near zero as the auroral flux moves south [Lanchester (2003)]. Unlike the auroral activity, the unshifted hydrogen emission retains an elevated emission level for four hours, until 19:00 UT. The reason for this is not entirely clear. It is not, as was first suspected, nearby auroral emission scattered into the SIF aperture by atmospheric hydrogen;

the global auroral emissions do not follow a similar pattern. One explanation is the intense proton precipitation elevated hydrogen density at every level over the station. Thus the elevated hydrogen density above the shadow height was excited by sunlight and we observed higher than usual geocoronal emission. The shape of the emission decay is a plausible shape for hydrogen dispersion, and lends support to this theory. The varied baseline of the unshifted hydrogen emission trace is a composite of the geocoronal emission and the unexcited emission from the auroral hydrogen population deposited at various altitudes throughout the upper atmosphere.

## 9.6 Analysis and Discussion

The unbroken H $\beta$  emission during the 4-minute-sample survey indicates that at least part of the unshifted hydrogen emission is omnipresent. Thus, the continuous  $2.0 \pm 1.5$  Rayleigh unshifted hydrogen emission, originates from the omnipresent hydrogen geocorona. Additionally, the survey also shows a clear and immediate response to the auroral event on November 26<sup>th</sup>. The geocoronal emission increased by 230% of its average unshifted hydrogen emission to almost 5 Rayleighs, when the proton aurora brightened to 150 Rayleighs. These observations indicate the unshifted hydrogen emission is derived from two sources: a relatively stable geocoronal hydrogen emission component and an auroral excited emission from hydrogen at auroral altitudes. The H $\beta$  line width can not be resolved with SIF and analysis finds the width of the geocoronal emission line to be comparable with that of the instrument function. No measurable change in the line width is detected with varying auroral activity.

## Chapter 10

# Measurement of the Auroral Proton Emission.

This chapter contains two investigations of the  $H\beta$  emission over Svalbard during periods of aurora activity. The first investigates the auroral emission resulting from the impact of a shock front in the solar wind on November 26<sup>th</sup>, 2000 [Lanchester et al., 2001]. The analysis includes bi-gaussian line analysis of the  $H\beta$  Doppler profile and discusses the implications of these results on the particle dynamics. The second investigation is of a very strong auroral emission detected during the late morning period of November 27<sup>th</sup>, 2000. This is the first such analysis of sunlight-contaminated proton aurora data, enabled by the novel sunlight subtraction mechanism developed in section 8.1.

### 10.1 The Event of November 26<sup>th</sup>

#### 10.1.1 Satellite Observations of the Event

The ACE satellite observes the solar wind in situ from its orbit around the first Lagrangian position at 230  $R_E$  sunward of Earth. At 05:30 UT on November 26<sup>th</sup>, ACE registered an increase in the solar wind flow speed. This increase continued steadily for two hours until at 07:30 UT; the flow speed suddenly became constant and an increase from 10 to 40 particles/cm<sup>3</sup> was recorded. For the next four hours the density gradually returned to 10 particles/cm<sup>3</sup>. At 11:40 UT a large discontinuity in solar wind density, and thermal and flow velocities synonymous

with a shock in the solar wind was detected. Lockwood et al. (2003) study the results of the short negative excursion of the IMF  $B_z$  component at around 15:00 UT.

### 10.1.2 HiTIES $H\beta$ Observations

The pressure shock measured by ACE at 07:30 UT resulted in a short timescale brightening when it struck the magnetosphere, observed over Nordlysstasjonen by HiTIES at 08:03 UT. Similar events are presented in [Lühr et al. (1996)]. This brightening is studied in much more detail in Lockwood et al. (2003), and can be seen in figure 10.1. HiTIES was switched off between 09:20 UT and 12:11 UT. The remaining data between 07:00 UT and 15:00 UT were contaminated and obscured by scattered sunlight. The technique described in section 8.1 was used to estimate and remove the contaminant. The revealed brightness of the  $H\beta$  emission is shown in figure 10.1. a 24 hour overview plot of the  $H\beta$  brightness between 05:00 UT on November 26th to 05:00 UT on November 27th. HiTIES was turned off at 09:20 UT and not reactivated until 12:10 UT. 12:10 UT is 40 minutes after first detection by ACE at the L1 point and the shock protons are already precipitating into the atmosphere over Nordlysstasjonen. Unfortunately a mistake was made in the ESR data recording during the event, and radar data is not shown for the period. The auroral  $H\beta$  spectra produced from these particles were integrated by HiTIES directed at the magnetic zenith between  $79.2^\circ$  and  $83.2^\circ$ .

The average brightness of the event varied around 250 Rayleighs for 3.5 hours between 12:10 UT and 15:40 UT. The peak brightness of this event was  $380 \pm 117$  Rayleighs a few minutes after 15 UT. This corresponds to brief negative excursion of the IMF  $B_z$  component, detected by ACE at around 14:30 UT [Lockwood et al. (2003)]. This change in the IMF causes a southward movement of the area of auroral emission shortly after. Figure 10.2 shows two plots of the event in more detail. The upper graph presents the brightness of the  $H\beta$  emission, while the lower panel presents the spectrogram at that time. Further analysis of the event requires more insight into the particle dynamics. This insight is gained through the Lummerzheim bi-gaussian line fit technique detailed in section 10.1.3.

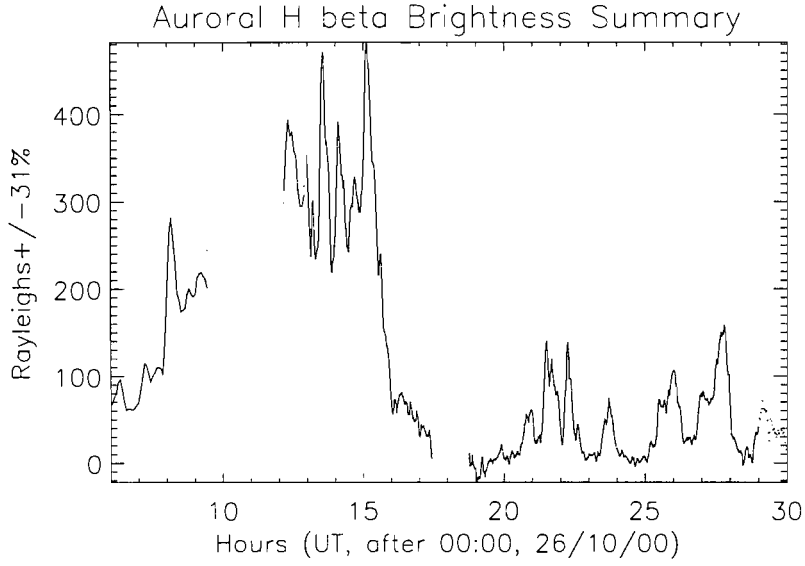


Figure 10.1: The overall brightness of the  $H\beta$  emission recorded between 05:00 UT on November 26th and 05:00 UT on November 27th. This period contains times during which the spectrograph took no data.

### 10.1.3 The Lummerzheim Bi-Gaussian Line Fit

This is a line fitting procedure [Lummerzheim et al. (2001)] for parameterising the shape of the doppler shifted auroral hydrogen beta emission. All of the data analysed using this fitting method have had the contaminating sunlight removed as described in section 8.1 of chapter 8. The reduction of the auroral profile to a number of parameters describing its shape enables quantitative analysis of profile shape with time. The fitting equation described by the paper is reproduced in equation 10.1

$$I(\lambda) = I_L \exp^{-\left(\frac{\lambda - \lambda_0}{\Delta(\lambda)}\right)^2} + I_B \quad (10.1)$$

where,  $I(\lambda)$  is the profile shape as a function of wavelength,  $I_B$  is the background brightness,  $\lambda_0$  is the wavelength at which the doppler profile peaks, and  $I_L$  is the peak brightness at  $\lambda_0$  minus the background.  $\Delta(\lambda)$  is given by equation 10.2 [Lummerzheim et al. (2001)] below;

$$\Delta(\lambda) = \frac{1}{2\sqrt{\ln 2}} \left[ 1 - \tanh \frac{\lambda - \lambda_0}{\lambda_S} \right] (\lambda_B - \lambda_R) + \lambda_R \quad (10.2)$$

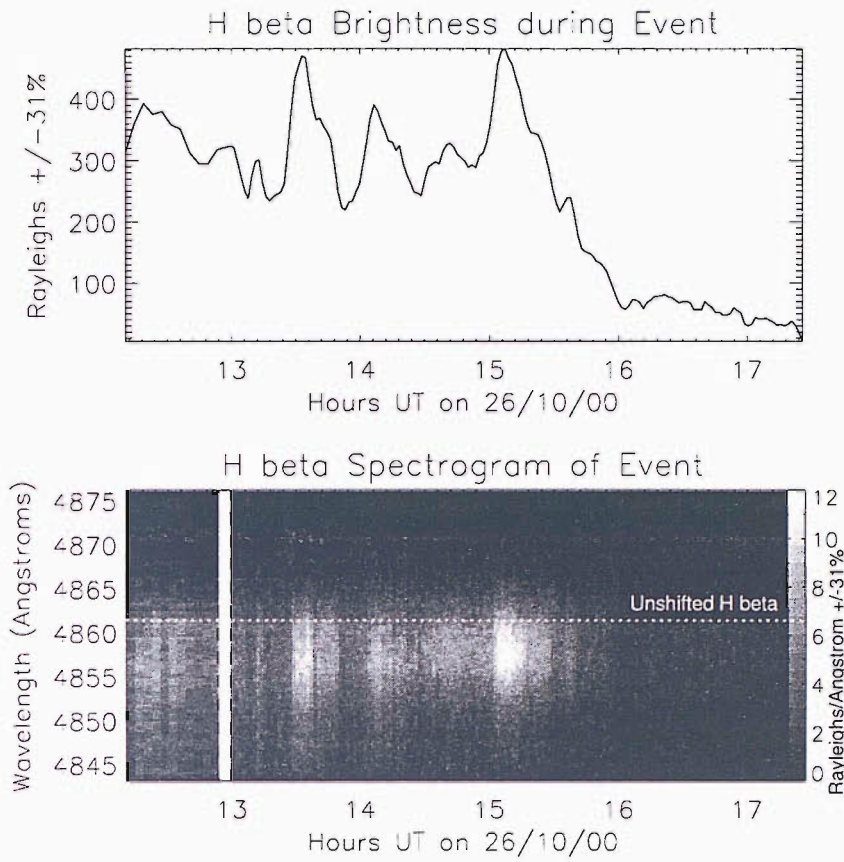


Figure 10.2: The Balmer beta brightness plot and spectrogram recorded from 12:20 UT to 17:27 UT on November 26th. The vertical wavelength axis of the spectrogram represents the full size of the H $\beta$  filter on the spectrograph. The position of unshifted H $\beta$  emission is indicated by a dashed white line. The black pixels in the centre of the spectrogram are saturated.

where  $\lambda_B$  is the half-width of the half gaussian on the blue side of the profile peak( $\lambda_0$ ),  $\lambda_R$  is the half-width of the red side of the profile peak( $\lambda_0$ ) and  $\lambda_S$  defines the steepness of the step function minimising the unwanted halves of each profile.

A modification of this procedure was made to incorporate the unshifted hydrogen component of the curve. The function is described in section 8.3.1 and its action displayed in figure 10.3. The added complexity of this equation required good signal to noise in the target data to acquire an accurate fit. This made using this procedure impractical when processing large data sets. The unshifted hydrogen emission was estimated using the targeted gaussian fit method described in section 8.3.4 and then this estimate was subtracted from the data profile. Once

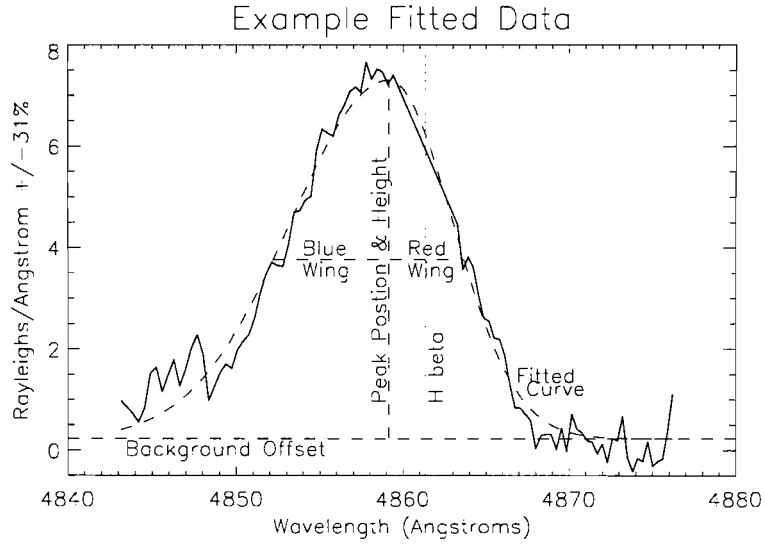


Figure 10.3: An example data curve in bold. The fitted line  $I(\lambda)$  is drawn as a curved dashed line. The fitting parameters are described with straight dashed lines and the labels: Peak Height( $I_L$ ), Peak Position ( $\lambda_0$ ), Blue Wing ( $\lambda_B$ ), Red Wing ( $\lambda_R$ ), background offset ( $I_B$ ), geo-coronal intensity ( $I_G$ ) and line width ( $\lambda_{IF}$ ). The unshifted hydrogen line position is marked with a vertical dotted line.



the contamination from sunlight and atmospheric hydrogen has been removed, the parameters of equation 10.1 are acquired by a least squares fit of the function to the processed data profile.

The data between 12:10 UT and 16:00 UT was selected for analysis. The function was fitted to each spectrum in the data range and the fitting parameters recorded. A selection of these parameters are plotted in figure 10.4. In figure 10.4(a),  $[I_L]$ , shows the peak amplitude of the fitted curve. In figure 10.4(b),  $[\lambda_{H\beta} - \lambda_0]$  shows the peak position with respect to  $\lambda_{H\beta}$ . The peak position gives the mean emission velocity of the precipitating particle population. In figure 10.4(c),  $[\lambda_{H\beta} - \lambda_0 + \lambda_B]$  shows the blue shift between  $\lambda_{H\beta}$  and the half maximum of the blue shifted curve and in figure 10.4(d),  $[\lambda_R - (\lambda_{H\beta} - \lambda_0)]$  shows the red shift between  $\lambda_{H\beta}$  and the half maximum of the red shifted curve.

#### 10.1.4 Fitting Parameter Analysis

##### A Measured Red Extent

The fitted curve displays a Doppler red shifted full width half maximum (FWHM)  $[\lambda_R - (\lambda_{H\beta} - \lambda_0)]$  of more than 2 Å. This red shift is clearly larger than can be accounted for by the  $\pm 0.63$  Å instrument function broadening of the unshifted hydrogen emission. This constitutes the first unambiguous measurement of red shifted auroral hydrogen emission from dayside precipitation: empirical evidence that large angle scattering occurs during proton precipitation.

During the proton transit of the atmosphere, the auroral particles are involved in numerous scattering processes with atmospheric particles. A small fraction of these scattering events result in a large angle deflection from their incident trajectory. If this deflection is large enough, it reverses the particle velocity, back out into space. The velocity distribution of these backscattered particles is described by the red shift of the emission profile. If the velocity ( $v_P$ ) of the emitting hydrogen in km/s, away from the spectrograph is defined as positive,  $\lambda_D$  is the Doppler shift due to the particle velocity,  $\lambda_{H\beta}$  is 4861.3 Å, and 'c' is the speed of light in km/s. Then  $v_P$  is expressed in equation 10.3:

$$v_P = \frac{\lambda_D}{\lambda} c \quad (10.3)$$

Using this relationship, the profile brightness can be plotted versus the emitting particle velocity. The brightness is displayed in brightness/velocity step and the velocity is in km/s away from

the spectrograph. The instrument function of  $\pm 1.97$  pixels or  $\pm 0.63 \text{ \AA}$  in this order, is equal to  $\pm 39 \text{ km/s}$ . This is plotted about the unshifted  $\text{H}\beta$  position using a dotted line in figure 10.5. This plot indicates the velocity distribution of the population of precipitating particles that have been large angle scattered.

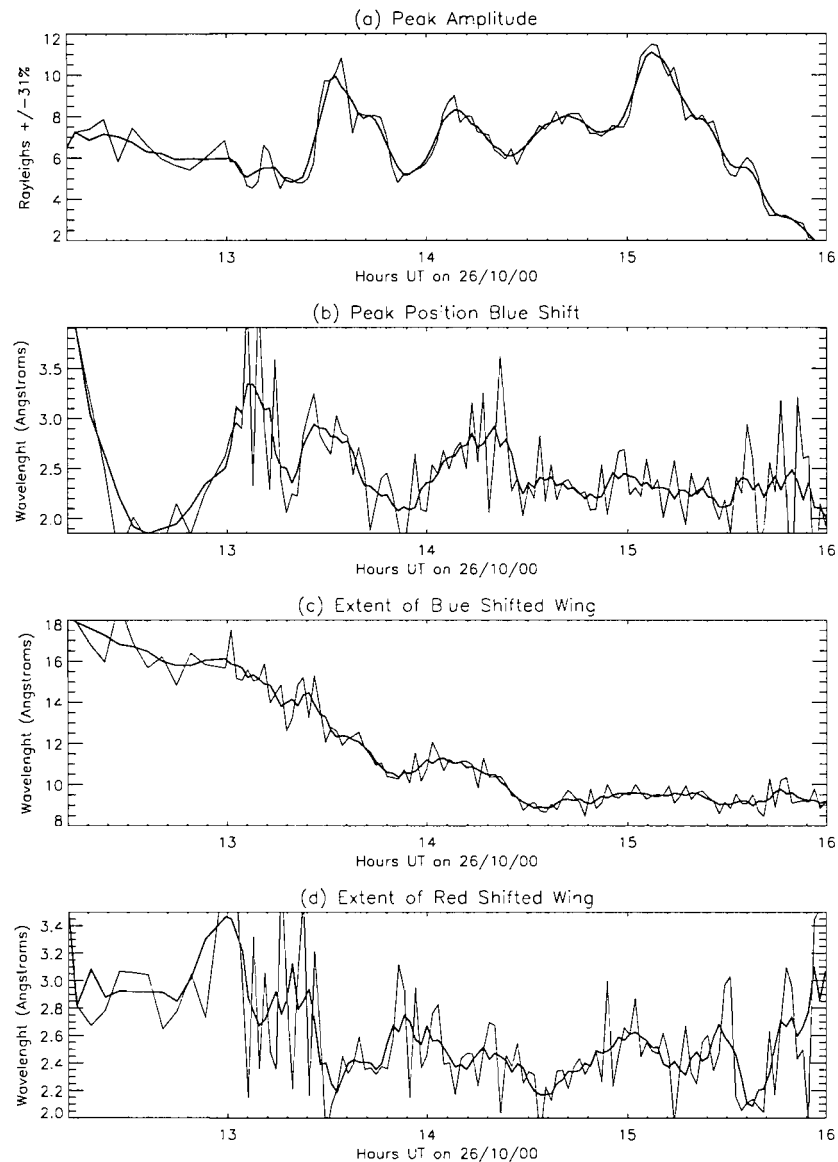


Figure 10.4: These graphs represent the temporal evolution of four parameters derived from curve fitted variables: (a) Peak Amplitude, (b) Peak Centre with respect to  $4861.3 \text{ \AA}$ , (c) The bit of the FWHM to the blue of  $4861.3 \text{ \AA}$  and (d) the bit of the FWHM to the red of  $4861.3 \text{ \AA}$ . The thin line shows the fitted parameter, while the thick line shows the running mean of that and the two nearest pixels.

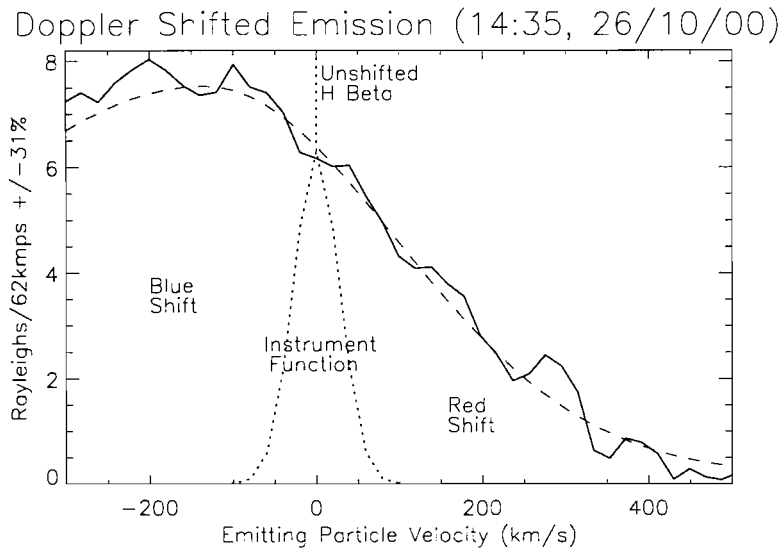


Figure 10.5: A generic auroral hydrogen emission profile displayed vs emitting particle velocity along line of sight. Positive is defined as away from the spectrograph. The instrument function is plotted about the 0 km/s position. The scale corresponds a wavelength range of 4858 Å to 4869 Å. A minute integration on from four degrees of slit elevation, centered on the local magnetic zenith. The fitted Lummerzheim function is shown as a dashed line.

### The Doppler Profile and the Energy spectrum of the Originating Population

Auroral proton precipitation involves reconnection, motion along changing magnetospheric field lines and ultimately, atmospheric collision processes. The shape of the Doppler shifted profile observed in the H $\beta$  filter is dictated by the velocity of the emitting particles. Changes in the profile size and shape are evidence for changes in the incoming proton flux and energy.

Ground based observation from HiTIES provides an excellent monitor for changes in the precipitating proton energy spectrum and flux. The temporal and spatial ambiguity associated with single point measurements can be offset with data from Earth observation satellites and low orbit satellite in-situ sampling. Lanchester et al.(2003) present a multi-instrumental and modelling investigation of this event. This thesis only presents data acquired from the HiTIES platform.

The faster particles produce larger doppler shift. The Doppler shifted part of the profile to the blue of the profile peak ( $\lambda_0$ ) is called the blue wing. An elevated and/or extended blue wing indicates the presence of a particle population with higher energy particles. The results of

Lanchester et al. (2003) confirm that the presence of an extended blue wing indicates the presence of a high energy tail in the incident particle population. The blue wing of the auroral profile when the event was at its most energetic was almost twice the size of the blue wing 3 hours later. Reduction in this blue wing is seen clearly over the afternoon in figure 10.4(c):  $[\lambda_{H\beta} - \lambda_0 + \lambda_B]$ , indicating a decrease in precipitating particle energy. Lummerzheim et al. (2001) suggest that the ratio between the peak intensity and a specified section of the blue wing yields information on the relative energetics of the precipitating particle population.

Figure 10.4(b):  $[\lambda_{H\beta} - \lambda_0]$  shows that the peak position clearly varies between 2 Å and 3 Å from the unshifted wavelength. Deehr et al. (1998) find the same pronounced variation in peak position in dayside proton aurora and maintain that it is due to the particle population being dominated by mono-energetic or narrow gaussian energy distributions. If we consider that the peak position is a function of penetration altitude [private communication, Rees], and the penetration altitude is a function of the particle energy; then logically the peak position varies as a function of input energy. This is not confirmed by the model.

This analysis reveals that the peak brightest of the event between 15:00 UT and 15:18 UT was not the result of an increase in the energetics of the proton precipitation. During the brightening both the peak position and the blue wing remained low and constant, indicating that this brightening was the result of an increase in the number of precipitating particles. IMF data taken by ACE indicates there was a brief negative excursion of the IMF  $B_z$  component that, with a 40 minute transit time, coincides with the brightening. The resulting increase in reconnection did not alter the velocity spectra of the precipitating particles, it only increased the number of precipitating particles. The corresponding rise in Doppler shifted Lyman- $\alpha$  emission, as seen by the IMAGE satellite has been studied by [Lockwood et al. (2003)].

### **The profile holds information on precipitation dynamics**

The distribution of the input energy thus governs the blue shift of the spectrum and the peak position of the spectrum. Comparisons between figure 10.4(b):  $[\lambda_{H\beta} - \lambda_0]$  and figure 10.4(c):  $[\lambda_{H\beta} - (\lambda_0 + \lambda_B)]$  reveal a clear relationship between the blue shift and the peak position. The blue extent, shown in figure 10.4(c), has three local maxima at 13:06 UT, 13:25 UT and 14:08 UT. The peak shift, shown in figure 10.4(b), also has three maxima at 13:09 UT, 13:30 UT and 14:18 UT. These data indicate that an elevation of the blue wing is followed, 4-10 minutes later, by an increased blue shift of the peak position. That is, an increase in the precipitation of

Table 10.1: This table shows the time lag between the local maxima in blue wing and the local maxima in peak position and the velocity associated with these Doppler shifts in km/s.

Peak (Hours)	Lag (minutes)	Blue Wing Velocity (km/s)	Peak Position Velocity (km/s)	Source Separation (km)
13:06	4	900	190	58,000
13:25	5	820	179	69,000
14:08	10	680	180	147,000

high energy tail particles is followed by an increase of the mean particle energy. The observed lag between blue shift maxima and peak position maxima is shorter for higher blue shifts. The velocity equating to the Doppler shift of the peak or the blue wing is calculated using equation 10.3. The data are presented in Table 10.1.

The nature of this lift in blue shift, followed by a lift in mean energy is indicative of a dispersion profile. Assuming a population of particles with a velocity distribution disperses from a remote magnetospheric point with little or no acceleration after exiting that point,  $velocity = distance/time$  can be solved for the distance to the origin. The calculated distance to the origin is shown in the last column of Table 10.1.

The first two data points indicate the particles travelled a distance of around  $10 R_E$ . Referring to [Deehr et al. (1998)] for the topology and approximate location of the merging point on the dayside, this distance is commensurate with dayside low latitude merging with a southward IMF. The first of these two points indicates a closer merging point, perhaps because the magnetosphere was compressed by the higher pressure of the solar wind at that time. The third and last data point indicates the particle population has travelled around  $20-25 R_E$  from the source of dayside reconnection. This distance is commensurate with high latitude dayside merging with a northward IMF and occurred after the IMF had turned northward [Lockwood et al. (2003)].

## 10.2 Observation of aurora due to cusp precipitation during northward IMF

It was thought that no other major events were observed during the campaign. Sometime after the campaign, the sunlight contamination removal technique was developed (described in

section 8.1), which allowed the investigation of data from the previously inaccessible sunlight contaminated periods. Data from this period is minimal however as our campaign observation plan considered the daylight period to have little value, and it was allocated to maintenance.

Using this technique, the collected daylight contaminated data was examined. Data near the average cusp position at around 11:42 MLT was regarded of most consequence, although coverage of this period is minimal. The sunlight was subtracted from contaminated data and a significant auroral event was found on November 27<sup>th</sup>, 2000 between 09:00 UT and 09:45 UT.

## 10.3 Observations

The detected event was the brightest yet observed with HiTIES. This section presents data collected from Svalbard, near magnetic noon on November 27, 2000.

### 10.3.1 HiTIES

The event observed in the HiTIES data started just before 09:00 UT (roughly 12:00 MLT) and lasted for approximately 45 minutes. The solar contamination was already strong by 09:00 UT. The later part of this period contains twilight emission two orders of magnitude brighter than the  $H\beta$  emission. Using the solar subtraction technique, this contamination was removed from the data spectra. Three example plots of this subtraction technique are shown in figure 10.6 - 10.8.

A time series plot of spectra observed by SIF between 08:00 UT and 10:00 UT is shown in the lower panel of figure 10.9. The upper panel shows the integrated brightness of the  $H\beta$  emission between 08:00 UT and 10:00 UT. It shows a strong brightening in auroral  $H\beta$  emission, with a maximum of  $750 \pm 232$  R peak at 09:25 UT.

### 10.3.2 IMAGE

The IMAGE satellite was well located between 08:00 UT and 10:00 UT to resolve the position of the cusp in the auroral oval. A sample of IMAGE data from the SI-12 instrument at 09:26 UT, near the peak brightness of the event, is shown in figure 10.10.

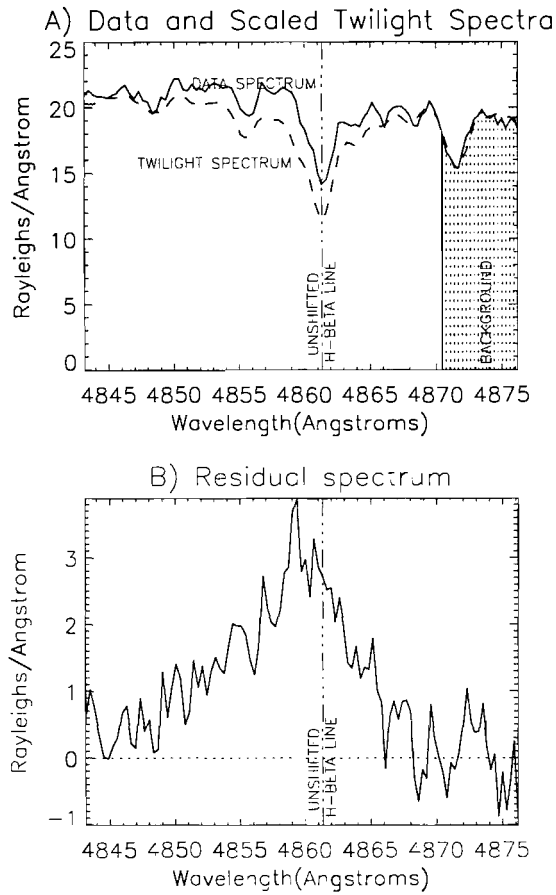


Figure 10.6: A: A measured spectrum (solid line), integrated for 60 seconds beginning at 08:40:56 UT on November 27, 2000. The  $\phi$  scaled twilight spectrum is drawn as a dashed line. B: The residual spectrum after the scaled twilight spectrum has been subtracted from the data spectrum.

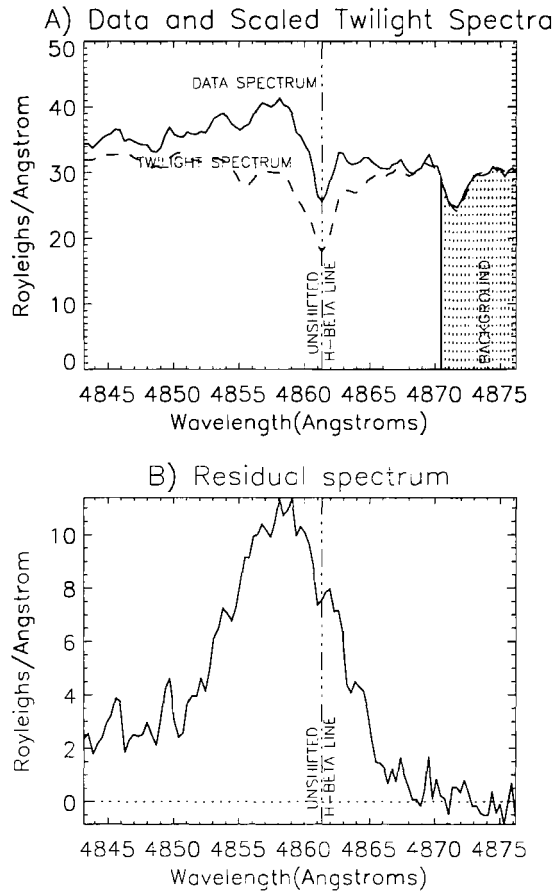


Figure 10.7: A: A measured spectrum (solid line), integrated for 60 seconds beginning at 09:15:06 UT on November 27, 2000. The  $\phi$  scaled twilight spectrum is drawn as a dashed line. B: The residual spectrum after the scaled twilight spectrum has been subtracted from the data spectrum.



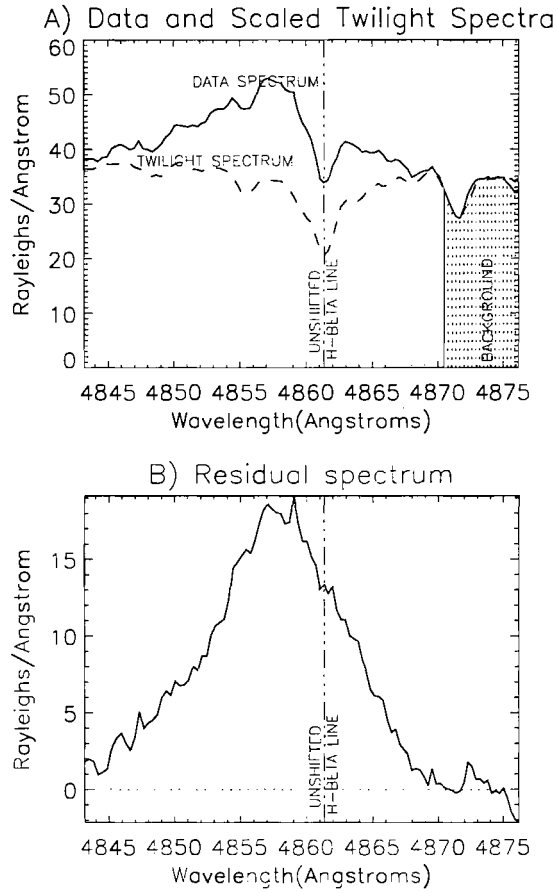


Figure 10.8: A) A measured spectrum (solid line), integrated for 60 seconds beginning at 09:21:57 UT on November 27, 2000. The  $\phi$  scaled twilight spectrum is drawn as a dashed line. B) The residual spectrum after the scaled twilight spectrum has been subtracted from the data spectrum.

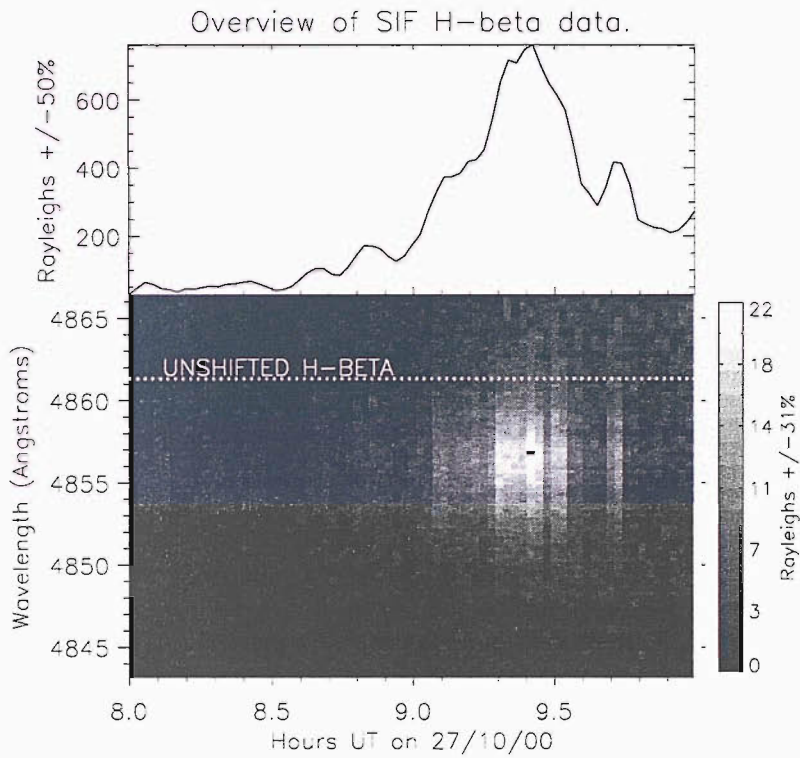


Figure 10.9: These two plots show the brightening in context. Both plots are over two hours: upper trace displays the integrated brightness of the  $H\beta$  emission in the lower spectrogram. The dotted line on the spectrogram marks the position of the unshifted  $H\beta$  wavelength.

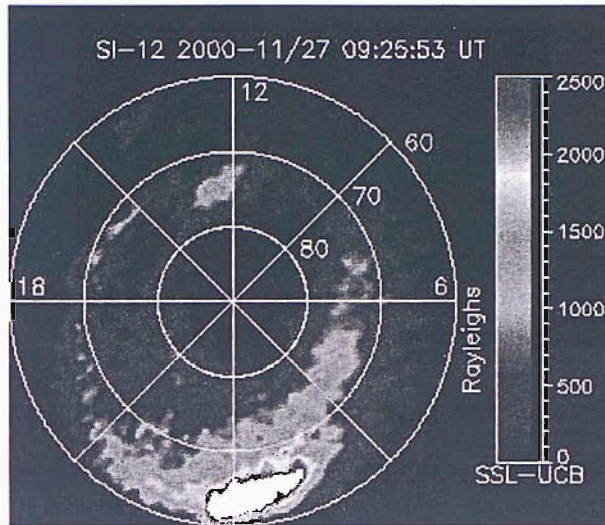


Figure 10.10: IMAGE Lyman- $\alpha$  spectrograph data at 09:25:53 UT. The radial lines are marked with magnetic latitude and the circumference is marked with magnetic local time.

Figure 10.10 shows a cusp spot [Frey et al. (2002)] on the duskward side of 12:00 MLT at a magnetic latitude of between  $72^\circ$  and  $76^\circ$ .

### 10.3.3 ESR Observations

There was no coverage of this period.

### 10.3.4 The IMF

In-situ observations of the IMF by ACE and WIND were analysed using a simple average speed time of flight calculation. WIND is positioned about 22 minutes away with a footprint at around 10:30 LT and a GSM x-component (the Sun-Earth Line) travel time of 14 minutes. The satellite observes the GSM z-component of the magnetic field becoming positive at 08:36 UT and some time later we observe the cusp spot brightening and moving northwards over Svalbard. This observation is in accord with the statistical observation that northward IMF is linked with cusp reconnection [Frey et al. (2002)]. ACE at the L1 point, is 40 minutes away at the average velocity of the solar wind. Figure 10.11 presents the ACE measurements of the solarwind and IMF. ACE observed the z-component become positive at 08:09 UT and stay positive for our observed duration apart from a very small and brief excursion at 09:04 UT. These conditions

are excellent for creating the northward IMF cusp spot observed in figure 10.10. The GSM-y component was observed turning negative at 08:42 UT, implying a dawnward movement of the cusp beginning at 09:22 UT. This was just before the peak brightness was observed by SIF and the cusp moved dawnwards out of the field of view.

## 10.4 Analysis and Discussion

The position of the cusp varies with the direction of the IMF and the flux of the solar wind [Newell and Meng (1994); Frey et al. (2002)] The IMAGE data in figure 10.10 show that the cusp spot was located at an MLT and MLAT corresponding to Svalbard around 09:25 UT. This is the auroral signature of lobe reconnection with the northward IMF. The movement of this spot about the dayside auroral oval captured by IMAGE is as predicted for the varying IMF clock angle [Lockwood et al. (2003)]. The local effect of the cusp movement on the Lyman- $\alpha$  emission brightness can be approximated by tracing the Lyman- $\alpha$  brightness over Svalbard with time. Integrating the IMAGE Lyman- $\alpha$  brightness within 2 degrees of latitude and longitude of Nordlysstasjonen, a trace of the Lyman- $\alpha$  brightness over Svalbard for the period 08:00 UT to 10:00 UT is created. This trace is shown in figure 10.12.

The brightness time series measured in Lyman- $\alpha$  from orbit and solar-decontaminated Balmer H $\beta$  from the ground are shown in figure 10.12. These measurements of hydrogen emission in Lyman- $\alpha$  and Balmer- $\beta$  are excited through similar mechanisms.

The IMAGE trace represents a sum of pixel brightness subtending hundreds of square kilometers over Svalbard for 5 seconds every 2 minutes. The HiTIES data on the other hand, is in 1 minute integrations of a small region sky over Svalbard. These traces are similar due to proton aurora diffusion away from the field lines. The similarity of these traces also indicates a level of reliability in the respective data reduction mechanisms. Visual inspection of figures 10.6 - 10.8 show the resulting profiles to have a relatively low blue-shift. The profiles were analysed using the line fitting parameterisation [Lunmerzheim et al. (2001)] and the fit parameter results are displayed in figure 10.13.

Figure 10.13 displays the Lunmerzheim fit parameters of the hydrogen emission profiles provide some insight into the particle energetics. The graphs are: figure 10.4(a):  $[I_L]$  - the peak amplitude of the fitted curve; figure 10.4(b),  $[\lambda_{H\beta} - \lambda_0]$  - the Doppler shift of the peak position, and

## ACE Solar Wind Measurements

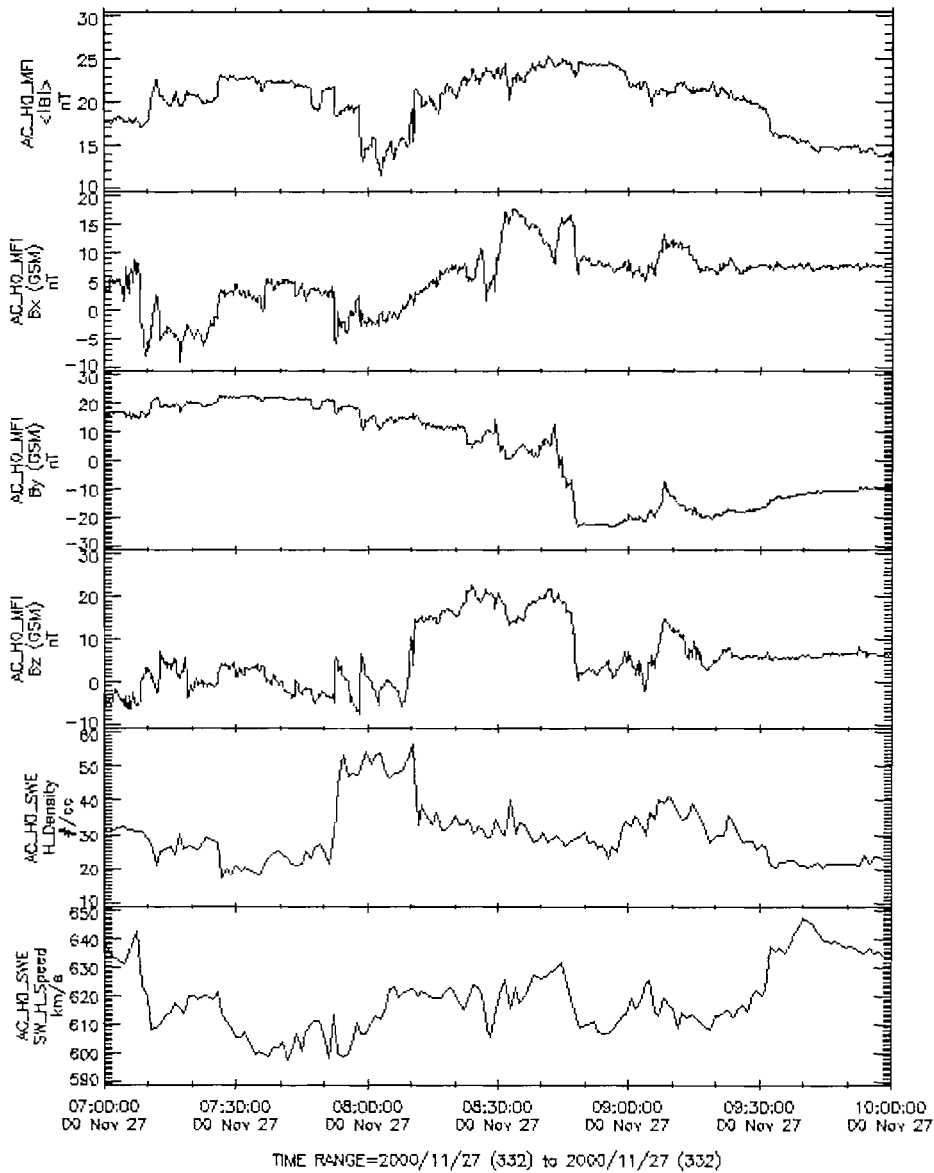


Figure 10.11: Observations of the solarwind and IMF from the Advanced Composition Explorer (ACE). The magnetic field is described in terms of its magnitude and X, Y and Z components in the Geocentric solar-magnetospheric (GSM) coordinate system. The solarwind plasma density and speed is also presented.

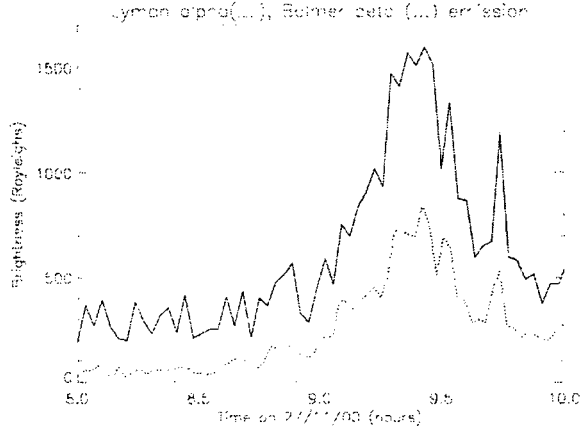


Figure 10.12: The solid line presents the Lyman- $\alpha$  brightness measured by the IMAGE S12 imager and the dotted line represents the H $\beta$  brightness. The Lyman- $\alpha$  trace has roughly twice the brightness of the Balmer- $\beta$  trace, although the H $\beta$  data has a 31% error.

figure 10.4(c);  $[\lambda_{H\beta} - (\lambda_0 + \lambda_B)]$  - a measure of the blue shift. The most interesting facet of these traces is that between 09:06 UT and 09:24 UT the peak position increased by 1.0 Å, while the blue wing remained constant. The data after 09:36 UT results from a poor fit to lower signal to noise data. The low blue extent (just 9 Å) indicates that the very high brightness stems from an increase in the particle flux, not from an increase in the particle energy. This indicates that this aurora originates from dayside reconnection [Burch (1968)]. Taken within the context of the event of the day before, the signature of a high brightness and low blue extent also signifies a strong reconnection process. As more ground based data is collected on cusp aurora, this analysis technique will allow comparative study of the ground observed cusp auroral spectra and related energetics.

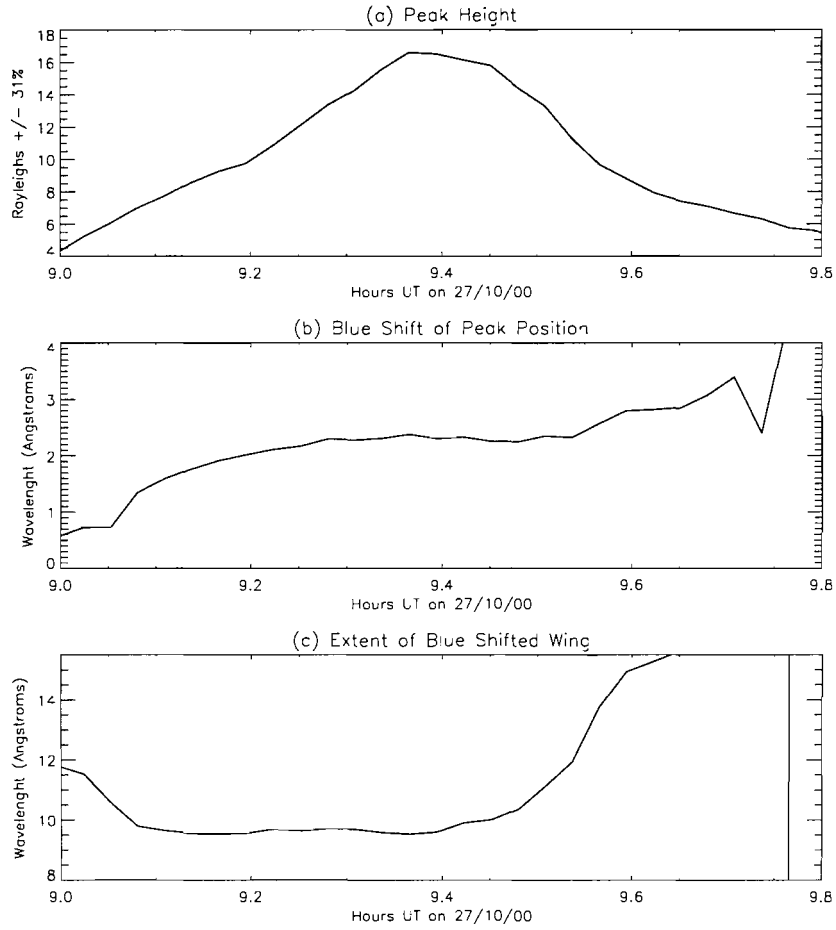


Figure 10.13: These graphs represent the temporal evolution of three parameters derived from curve fitted variables: (a) Peak Height, (b) Peak position with respect to  $4861.342 \text{ \AA}$ , (c) The FWHM of the curve to the blue of  $4861.342 \text{ \AA}$ .

## Chapter 11

# Conclusion

The thesis holds the characterisation of the High Throughput Imaging Echelle Spectrograph and several pieces of original research.

### 11.1 Sunlight Subtraction

A mechanism of subtracting scattered sunlight was developed. This technique proved to be effective in removing twilight contamination accurately. Use of this technique enabled the study of previously unexamined data around the noon period. This furthered the investigation of the event of November 26<sup>th</sup> and was essential in finding and investigating the HiTIES detection of auroral emission from lobe reconnected precipitation. Further study of dayside cusp emission using HiTIES and related spectrographic instruments will require use of this technique.

### 11.2 Ground Based Observation of the High Latitude Cusp

Confirmation that the cusp has moved over SIF was achieved from IMAGE data. The data recorded by HiTIES at that time was seen to contain a large brightening, and it was deduced that this emission is due to cusp reconnection precipitation resulting from the reconnection at high latitudes. The profile shape contains information on the dynamics of cusp precipitation. This is the first published ground-based optical measurement of  $H\beta$  auroral emission from the high latitude cusp.



### 11.3 Proton Aurora Observation

HiTIES recorded a signature of dayside proton aurora during the event of November 26<sup>th</sup>. This was an important milestone for HiTIES. It recorded the event with enough resolution to resolve red shifted  $H\beta$  emission in dayside auroral proton precipitation. Using the Lummerzheim fit to parameterise the spectra was a useful method of data reduction. This method clearly showed the doppler profile peak to move between 2 Å and 3 Å from the unshifted position. This result has been used to improve the proton precipitation models of both Galand [Galand et al. (1997)] and UCL [Aylward, priv. comm.]. The technique also showed a lagged relation between blue shift and peak position, that allowed an extrapolation of the changing distance to the merging point, even when the mode of reconnection changed. These data support the hypothesis of continuous reconnection [Frey et al. (2003)].

### 11.4 Geocorona Study

Investigation of geocoronal emission has not been carried out so far north. The data survey indicates that at least part of the unshifted hydrogen emission is always present. A continuous  $2.0 \pm 1.5$  Rayleigh unshifted hydrogen emission, originates from the omnipresent hydrogen geocorona. Additionally, the survey also shows a clear and immediate response to the auroral event on November 26<sup>th</sup>. The geocoronal emission was shown to increased by 230% of its average unshifted hydrogen emission to almost 5 Rayleighs, when the proton aurora brightened to 150 Rayleighs. The decay phase of the geocoronal event requires further study.

### 11.5 Further Work

Further study of emission from the cusp is suggested. This study would require recording data three hours either side of 11.7 MLT, a period contaminated by sunlight. A polarizer could be employed to reduce the amount of scattered sunlight by up to 80% and the data by just 50%. This would allow study of strong daytime auroral emission in the presence of strong daylight emission. The same technique could be used to study any emission not excited by sunlight. Development of the stellar efficiency brightness calibration method is suggested.

## Using the hydrogen Balmer $\alpha$ band

The  $H\beta$  emission was chosen because the stronger  $H\alpha$  band is contaminated by Vegard-Kaplan emission. Recording and investigating  $H\alpha$  would potentially improve instrument sensitivity to auroral hydrogen emission by up to four times. It would also allow the study of the Balmer decrement in auroral hydrogen emission.

# Bibliography

- [Ångström (1869)] Ångström, A.J., Spectrum des Nordlichts, *Poggendorf's Annalen*, 137, p.161-163, 1869.
- [Baker and Romick (1976)] Doran J. Baker and Gerald J. Romick. The rayleigh: interpretation of the unit in terms of column emission rate or apparent radiance expressed in SI units.". *Applied Optics*, 15(8), August, 1976.
- [Baranne et al. (1972)] Baranne. A., "ESO/CERN Conf on Aux. Instrumentation for large telescopes". 227, Edited by S. Laustsen and A. Reiz. *ESO conf. proc.*, 1972.
- [Basu et al. (2001)] Basu, B., D. T. Decker, J. R. Jasperse, Proton transport model: A review. *J. Geophys. Res.*, 106(41), p.93-106. 2001.
- [Baumgardener et al. (1993)] Baumgardner. J., Flynn, B., and Mendillo, M., Monochromatic imaging instrumentation for applications in aeronomy of the earth and planets, *Optical Engineering*, 32(12), p.3028-3032. 1993.
- [Bertaux (1978)] Bertaux, J.L., Interpretation of OGO-5 shape measurements of Lyman  $\alpha$  emission from terrestrial exospheric hydrogen. *Planet.Space.Sci.*, 26, p.431-447, 1978.
- [Blixt et al (2005)] Blixt. E. M., T. Grydeland, N. Ivchenko, T. Hagfors, C. La Hoz, B. S. Lanchester, U P. Lauvhaug, and T. S. Trondsen, Dynamic rayed aurora and enhanced ion-acoustic radar echoes. *Annales Geophys.*, 23, p.3-11, 2005.
- [Brasseur and Solomon (1984)] Brasseur, G., and Solomon, S., Aeronomy of the middle atmosphere: Chemistry and physics of the stratosphere and mesosphere, *Dordrecht, D. Reidel Publishing Co., Institut d'Aeronomie Spatiale de Belgique; Bruxelles, Universite Libre, Brussels*, p457, 1984.

- [Brinton (1975)] Brinton, H. C., H. G. Mayr, W. E. Potter, Winter bulge and diurnal variations in hydrogen inferred from AE-C composition measurements, *National Aeronautics and Space Administration*, Goddard Space Flight Center, Greenbelt, MD. & National Aeronautics and Space Administration, 06/1975.
- [Burch (1968)] Burch J.L. Low-energy electron fluxes at latitudes above the auroral zone, *J. Geophys. Res.*, *73*, p.3585, 1968.
- [Chakrabarti et al. (2001)] Chakrabarti, S., Pallamraju, D., and Baumgardner, J., HiTIES: A High Throughput Imaging Echelle Spectrograph for ground-based visible airglow and auroral studies, *J. Geophys. Res., Space Physics Special Section*, *106*, p.30337, 2001.
- [Chamberlain (1961)] Chamberlain, Physics of the Aurora and Airglow, *International Geophysics Series*, New York: Academic Press, 1961.
- [Copernicus (1514)] Copernicus, N., Commentariolus, 1514. Referred to by 'On the revolutions'. Edward Rosen. *Johns Hopkins University Press. ISBN 0-801-84515-7*, 1992.
- [Cowley (1982)] Cowley, S.W.H.. The causes of convection in the Earth's magnetosphere: A review of developments during IMS, *Rev. Geophys.*, *20*, p.531-565, 1982.
- [Crooker (1979)] Crooker, N. U., Dayside merging and cusp geometry, *J. Geophys. Res.*, *84*, Mar. p.951-959, 1979.
- [Dashkevich et al. (1996)] Dashkevich, B.V., B.V. Kozelov, V.Y. Ivanov, Lyman -Birge-Hopfield bands in proton auroras. *Geomag. and Aeron.*, *35*, *6*, p.812-817, 1996.
- [Deehr et al. (1998)] Deehr, C.S., Lorentzen, D.A., Sigernes, F., and Smith, R.W., Dayside auroral hydrogen emission as an aeronomic signature of magnetospheric boundary layer processes, *Geophysical Research Letters*, *25*, p.2111, 1998.
- [Donovan (2002)] Donovan, E., The Aurora: A Review, Private Communication eric@clearwater.phys.ucalgary.ca, 2000.
- [Dungey (1953)] Dungey J.W., Conditions for the occurrence of electrical discharges in astrophysical systems, *Philosophical Magazine*, *44*, p.725, 1953.
- [Dungey (1961)] Dungey J.W., Interplanetary magnetic field and the auroral zones, *Physical Review Letters*, *6*, p.47, 1961.

- [Eather and Jacka (1966)] Eather, R.H., Auroral hydrogen emission, *Australian Journal of Physics*, 19, p.241-274, 1966.
- [Eather (1967)] Eather, R.H., Proton precipitation and hydrogen emissions, *Rev. Geophys.*, 5, p.207-285, 1967.
- [Eather (1970)] Eather, R.H., *Ann. Geophys.*, 26, p.609, 1970.
- [Emerich et al. (1976)] Emerich, C., S. Cazes, J. E. Blamont, Exobase hydrogen density temperature from Lyman alpha absorption and polarization measurements. II - Dayside and nightside results during April 1971, *J. Geophys. Res.*, 81, p.6103-6114, 1976.
- [Fishkova and Marzvaladze (1966)] Fishkova, L. M. and Marzvaladze, N. M., On the H-emission variations and on the hydrogen distribution in the upper atmosphere, *Aurorae and Airglow, in Results of the IGY, USSR. Acad. Sci.*, 13, 35-40, 1966.
- [Forbush (1937)] Forbush, S. E., On Sidereal Diurnal Variation in Cosmic-Ray Intensity, Department of Terrestrial Magnetism, Carnegie Institution of Washington, *The American Physical Society*, 1937.
- [Fordham (1992)] Fordham, J. L. A.; Bone, D. A.; Oldfield, M. K.; Bellis, J. G.; Norton, T. J., The MIC photon counting detector, *In ESA, Proceedings of an ESA Symposium on Photon Detectors for Space Instrumentation*, p103-106, 1992.
- [Frey et al. (2002)] Frey, H. U., Mende, S. B., Immel, T. J., Fuselier, S. A., Claffin, E. S., Gerard, J.-C. and Hubert, B., Proton aurora in the cusp, *J. Geophys. Res.*, 107, A7, 2002.
- [Frey et al. (2003)] Frey, H. U., T. D. Phan, S. A. Fuselier, S. B. Mende, Continuous magnetic reconnection at Earth's magnetopause, *Nature*, 426, 533-537, 2003.
- [Gaisser (1990)] Gaisser, T.K., Cosmic rays and particle physics, *Cambridge University Press*, ISBN 0521326676, 1990.
- [Galand et al. (1997)] Galand, M., Lilensten, J., Kofman, W., Sidje, R.B., Proton transport model in the ionosphere 1. Multistream approach of the transport equation, *J. Geophys. Res.*, 102, p.22261-22272, 1997.
- [Galand et al. (2001)] Galand, M., Baumgardner, J., Pia, U., Chakrabarti, S., Pallamraju, D., Lummerzheim, D., Lanchester, B.S., and Rees, M.H., High spectral resolution observations of proton aurora at Troms, Norway, *J. Geophys. Res.*, 2001.

- [Galand (2001)] Galand, M., Introduction to special edition: Proton precipitation into the atmosphere, *J. Geophys. Res.*, *106*, p.1-6, 2001.
- [Galand et al. (2004)] Galand, M., J. Baumgardner, D. Pallamraju, S. Chakrabarti, U. P. Lvhaug, D. Lummerzheim, B. S. Lanchester, and M. H. Rees, Spectral imaging of proton aurora and twilight at Troms, Norway, *J. Geophys. Res.*, *109* (A7), 2004.
- [Gartlein (1951)] Gartlein, C. W., Protons and the Aurora, Cornell University, New York, *The American Physical Society*, 1951.
- [Geitel and Elster (1893)] Geitel and Elster, Einige Demonstrationsversuche zum Nachweis einseitiger Elektrizitätsbewegung in verdünnten Gasen bei Anwendung glühender Elektroden, *Annalen der Physik*, *48*, p.625, 1893.
- [Gloeckler and Geiss (1989)] Gloeckler, G., and Geiss, J., The abundances of elements and isotopes in the solar wind, *AIP Conf. Proc.* *183*, *Cosmic Abundances of Matter*, p.49-71, 1989.
- [Grieder (2001)] Grieder, P.K.F., Cosmic rays at Earth, *Elsevier Science Ltd*, ISBN 0444507108, 2001.
- [Groom et al. (2000)] Groom, D.E., Aguilar-Benitez, M., Amsler, C., Barnett, R.M., Burchat, P.R., Carone, C.D., Caso, C., Conforto, G., Dahl, O., Doser, M., Eidelman, S., Feng, J.L., Gibbons, L., Goodman, M., Grab, C., Gurtu, A., Hagiwara, K., Hayes, K.G., Hernández, J.J., Hikasa, K., Honscheid, K., Kolda, C., Mangano, M.L., Manohar, A.V., Masoni, A., Mönig, K., Murayama, H., Nakamura, K., Navas, S., Olive, K.A., Pape, L., Piepke, A., Roos, M., Tanabashi, M., Törnqvist, N.A., Trippe, T.G., Vogel, P., Wohl, C.G., Workman, R.L., Yao, W.-M., Armstrong, B., Casas Serradilla, J.L., Filimonov, B.B., Gee, P.S., Lugovsky, S.B., Nicholson, F., Babu, K.S., Besson, D., Biebel, O., Bloch, P., Cahn, R.N., Cattai, A., Chivukula, R.S., Cousins, R.D., Damour, T., Desler, K., Donahue, R.J., Edwards, D.A., Erler, J., Ezhela, V.V., Fassò, A., Fetscher, W., Froidevaux, D., Fukugita, M., Gaisser, T.K., Garren, L., Geer, S., Gerber, H.-J., Gilman, F.J., Haber, H.E., Hagmann, C., Hinchliffe, I., Hogan, C.J., Höhler, G., Igo-Kemenes, P., Jackson, J.D., Johnson, K.F., Karlen, D., Kayser, B., Klein, S.R., Kleinknecht, K., Knowles, I.G., Kolb, E.W., Kreitz, P., Landua, R., Langacker, P., Littenberg, L., Manley, D.M., March-Russell, J., Nakada, T., Quinn, H.R., Raffelt, G., Renk, B., Rolandi, L., Ronan, M.T., Rosenberg, L.J., Sadrozinski, H.F.W., Sanda, A.I., Schmitt, M., Schneider, O., Scott, D., Seligman, W.G., Shaevitz, M.H., Sjöstrand, T., Smoot, G.F., Spanier, S., Spieler, H., Srednicki, M., Stahl, A., Stanev, T., Suzuki, M., Tkachenko,

- N.P., Turner, M.S., Valencia, G., van Bibber, K., Voss, R., Ward, D., Wolfenstein, L., and Womersley, J., Review of Particle Physics, *The European Physical Journal*, vol C15, p1+, <http://pdg.lbl.gov>, 2000.
- [Guiducci et al. (1619)] Guiducci, M., G. Galilei, Discorso delle comete DI Mario Gvidvcci fatto DA lvi nell'Accademia fiorentina, In Firenze, Nella stamperia di Pietro Ceconcelli, 1619.
- [Halliday et al. (1993)] Halliday, D., Resnick, R., and Walker, J., Fundamentals of Physics, *John Wiley & Sons, ISBN 9232801*, 1993.
- [Hapgood and Taylor (1982)] Hapgood, M.A., and Taylor, M.J., Analysis of airglow data, *Ann. Geophys.*, 38(6), p.805-813, 1982.
- [Hardy et al. (1989)] Hardy, D. A., M. S. Gussenhoven, D. Brautigam, A Statistical Model of Auroral Ion Precipitation. *J. Geophys. Res.*, 94, p.370, 1989.
- [Hardy et al. (1991)] Hardy, D. A., W. McNeil, M. S. Gussenhoven, and D. Brautigam, A statistical model of auroral ion precipitation. 2. Functional representation of the average patterns, *J. Geophys. Res.*, 96(A4), p.55395547, 1991.
- [He et al. (1993)] He, X., Kerr, R.B., Bishop, J., and Tepley, C.A., Determining exospheric hydrogen density by reconciliation of H $\alpha$  measurements with radiative transfer theory, *J. Geophys. Res.*, 98(A12), p.21611-21626, 1993.
- [Henriksen (1985)] Henriksen, K., Fedorova, N.I., Totunova, G.T., Deehr, C.S., Romick, G.J., and Sivjee, G.G., Hydrogen emissions in the polar cleft, *J. Atmospheric Terrestrial Physics*, 47, p.1051, 1985.
- [Hunten (1955)] Hunten, D. M., The interpretation of twilight measurements of sodium emission. Proceedings of the Airglow and the Aurorae symposium, *Belfast, Pergamon Press*, p.183. Sep 1955.
- [IDL 5.2] IDL 5.2, [www.rsinc.com](http://www.rsinc.com).
- [Ivchenko et al. (2004a)] Ivchenko, N., M. H. Rees, B. S. Lanchester, D Lummerzheim, M. Galand, K. Throp and I. Furniss Observation of O+ (4P-4D0) lines in electron aurora over Svalbard, *Ann. Geophys.*, 22, 2004.
- [Ivchenko et al. (2004b)] Ivchenko, N., M. Galand, M. H. Rees, B. S. Lanchester, D Lummerzheim, I. Furniss and J. Fordham. Observation of O+ (4P-4D0) lines in proton aurora over Svalbard, *Geophys. Res. Let.*, 31, 2004.

- [Ivchenko et al. (2005)] Ivchenko, N., M. Blixt and B. S. Lanchester, Multispectral observations of auroral rays and curls, *Geophys. Res. Lett.*, *32*, 2005.
- [Janesic et al. (1989)] Janesic, J.R., Blouke, M.M., and Freeman, J.. Scientific charge-coupled devices, *Optical Engineering*, *26(8)*, p.692-714, 1987.
- [Johnston (1989)] Johnston, W.E., A/D Conversion, *Optical Engineering*, *28(6)*, p.678, 1989.
- [Kerr et al. (1986)] Kerr, R.B, Atreya, S.K., Meriweather JR, J.W., Tepley, C.A., and Burnside, R.G., Simultaneous H $\alpha$  line profile and radar measurements at Arecibo, *J. Geophys. Res.*, *91(A4)*, p.4491-4512, 1986.
- [Kerr et al. (2001a)] Kerr, R.B, Garcia. R., He, X., Noto, J., Lancaster. R.S., Tepley, C.A., Gonzalez, S.A., Friedman, J., Doe, R.A., Lappen, M., and McCormack, B., Periodic variations of geocoronal Balmer-alpha brightness due to solar-driven exospheric abundance variations. *J. Geophys. Res.*, *106(A12)*, p.28797-28817, 2001.
- [Kerr et al. (2001b)] Kerr, R.B, Garcia. R., He, X., Noto. J., Lancaster, R.S., Tepley, C.A., Gonzalez, S.A., Friedman, J., Doe. R.A., Lappen, M., and McCormack, B., Secular variability of the geocoronal Balmer-alpha brightness: magnetic activity and possible human influences. *J. Geophys. Res.*, *106(A12)*, p.28819-28829, 2001.
- [Krassovsky and Galperin (1958)] Krassovsky V.I. and Galperin G.I., *Trans. Inst. Ast. Union.* *10*, 367, 1958.
- [Lanchester et al. (1997)] Lanchester, B.S., Rees, M.H., Lummerzheim, D., Otto, A., Frey, H.U., and Kaila, K.U., Large fluxes of auroral electrons in filaments of 100 m width, *J. Geophys. Res.*, *102(A5)*, p.9741-9748, 1997.
- [Lanchester et al. (2002)] Lanchester, B.S., Rees, M.H., Robertson, S.C., Lummerzheim, D., Galand, M., Mendillo, M., Baumgardner, J., Furniss, I., and Alyward, A.D., Proton and electron precipitation over Svalbard - first results from a new imaging spectrograph (HiTIES), *Proc of Atmospheric Studies by Optical Methods, Oulu*, p1-4, 2002.
- [Lanchester et al. (2003)] Lanchester, B.S., Galand, M., Robertson, S.C., Rees, M.H., Lummerzheim, D., Furniss, I., Peticolas, L.M., Frey, H.U., Baumgardner, J., and Mendillo, M., High resolution measurements and modelling of auroral hydrogen emission line profiles, *Annales Geophysicae*, *21*, p1-14 2003.



- [Lockwood et al. (2003)] Lockwood, M., B.S.Lanchester, H.U.Frey, K.Throp, S.K.Morley, S.E.Milan and M.Lester, IMF control of cusp proton emission intensity and dayside convection: implications for component and anti-parallel reconnection, *Annales Geophysicae*, 21, p.955-982, 2003.
- [Lummerzheim et al. (2001)] Lummerzheim, D., and Galand, M., The profile of the hydrogen  $H\beta$  emission line in proton aurora, *J. Geophys. Res.*, 106(A1), p.23-31, 2001.
- [Lloyd (1971)] Lloyd, K.H., Concise method for photogrammetry of objects in the sky, Weapons Research Establishment Technical Note 72, *Australian Defense Scientific Service, Canberra, Australia*, 1971.
- [Lorentzen et al. (1998)] Lorentzen, D. A., Sigernes, F., Deehr, C. S., Modeling and observations of dayside auroral hydrogen emission Doppler profiles, *J. Geophys. Res.*, 103(A8), p.17479-17488, 1998.
- [Lühr et al. (1996)] Lühr, H., Lockwood, M., Sandholt, P. E., Hansen, T. L., Moretto, T., Multi-instrument ground-based observations of a travelling convection vortices event, *Annales Geophysicae*, 14, Issue 2, p.162-181, 1996.
- [MacKay (1995)] MacKay, D.J.C., A Short course in Information Theory, [www.inference.phy.cam.ac.uk/mackay/info-theory/course.html](http://www.inference.phy.cam.ac.uk/mackay/info-theory/course.html), Cavendish Laboratory, Cambridge, UK, 1995.
- [Meaburn (1939)] Meaburn, J., Detection and spectrometry of faint light, ISBN 9027706786, *Astrophysics and Space Science Library*, 56, Manchester, England, 1939.
- [Meinel (1951)] Meinel, A. B., Doppler-Shifted Auroral hydrogen Emission, *Astrophysical Journal*, 113, p.50, 1951.
- [Mende et al (2000)] Mende, S. B., Far ultraviolet imaging from the IMAGE spacecraft, *Space Sci. rev.*, 91, p.287, 2000.
- [Meriwether et al. (1980)] Meriwether, J. W. Jr., S. K. Atreya, T. M. Donahue, R. G. Burnside, Measurements of the spectral profile of Balmer alpha emission from the hydrogen geocorona, *Geophys. Res. Let.*, 7, p.967, 1980.
- [Mierkiewicz et al. (2004)] Mierkiewicz, E.J., F. L. Roesler, J. Bishop, S.Nossal, A systematic program for ground-based Fabry-Perot observations of the neutral hydrogen exosphere: in-

- strumental characteristics, in *Optical spectroscopic techniques and instrumentation for atmospheric and space research III: Proc. Int. Soc. Opt. Eng.*, 3756, SPIE 323, 2004.
- [Montalbetti (1959)] Montalbetti, R., Photoelectric measurements of hydrogen emissions in aurora and airglow, *Journal Atmospheric Terrestrial Physics*, 14, p.200-212, 1959.
- [Neher (1952)] Neher, H.V., Progress in elementary particle and cosmic ray physics, North Holland Publishing Company, Amsterdam, 1952.
- [Newell and Meng (1994)] Newell P.T. and C-I Meng, Ionospheric projections of magnetospheric regions under low and high solar wind pressure conditions, *J. Geophys. Res.*, 99, p.273, 1994.
- [Nossal et al. (2004)] Nossal, S. M., F. L. Roesler, E. J. Mierkiewicz, R.J. Reynolds, Observations of solar cyclical variations in geocoronal H $\alpha$  column emission intensities, *Geophys. Res. Lett.*, 3, p.1+, 2004.
- [Oguti (1973)] Oguti, T., Hydrogen emission and electron aurora at the onset of the auroral breakup *J. Geophys. Res.*, 78, p.7543-7547., Nov. 1973.
- [Omholt (1957)] Omholt, A., Photometric observations of rayed and pulsating aurorae, *Astrophys. J.*, 126, p.461-463, 1957.
- [Oulu Space Physics Textbook] [www.oulu.fi/spaceweb/textbook/](http://www.oulu.fi/spaceweb/textbook/)
- [Pitout (2002)] Pitout, F.. The polar cusp and its ionospheric footprint, PhD thesis, Uppsala University, 2002.
- [Phan (2003)] Phan, T. et al., Simultaneous cluster and IMAGE observations of cusp reconnection and auroral proton spot for northern IMF, *Geophys. Res. Lett.*, 30, 2003.
- [Ptolemy (2)] Ptolemy, Almagest. GJ Toomer, London. 1984.
- [Rees (1989)] Rees, M. H., Physics and chemistry of the upper atmosphere, Cambridge University Press, Cambridge, UK, ISBN: 0521368480, 1989.
- [Schroeder (1987)] Schroeder, D.J., Astronomical Optics, Elsevier, USA, ISBN: 0126298106, 1987.
- [Sheglov (1963)] Sheglov, P. V., Concentration of nightglow H $\alpha$  emission to the ecliptic and the radial velocities of this line, *Nature*, 199, p.990, 1963.

- [Shih et al. (1985)] Shih, P., Roesler, F.L., and Schrb, F., Intensity variations of geocoronal Balmer alpha emission, *J. Geophys. Res.* 90(A1), p.477-490, 1985.
- [Shumilov and Robertson (2000)] [www.unis.no/gpsmeasurements.html](http://www.unis.no/gpsmeasurements.html), 2000.
- [Sigernes et al. (1993)] Modulation of the auroral proton spectrum in the upper atmosphere, *Journal Atmospheric Terrestrial Physics*, 55, 9, p.1289-1294, 1993.
- [Sigernes et al. (1994)] Sigernes, F., Lorentzen, D. A., Deehr, C. S., Henriksen, K., Calculation of auroral Balmer volume emission height profile in the upper atmosphere, *Journal Atmospheric Terrestrial Physics*, 56, 4, p.503-508, 1994.
- [Smart (1965)] Smart, Spherical Astronomy, 5th Ed., Cambridge University Press, Cambridge, UK, 1965.
- [Smith and Lockwood (1996)] Smith, M.F., and Lockwood, M., Earth's magnetospheric cusps, *Reviews of Geophysics*, 34, p.233-260, 1996.
- [Thorne (1974)] Thorne, A.P., Spectrophysics, Springer, USA, ISBN: 3540651179, 1974.
- [Tinsley (1974)] Tinsley, B.A., Variations of Balmer- $\alpha$  emission and related hydrogen distributions, *Space Research*, 10, p.582-590, 1970.
- [Trondsen (1996)] Trond S. Trondsen. The Portable Auroral Imager, PhD Thesis from the University of Calgary, 1996.
- [Ugolnikov (1999)] Ugolnikov, O.S.. Twilight sky photometry and polarimetry: The problem of multiple scattering at the twilight time. *Cosmic Research*, 37, p.159, 1999.
- [Ugolnikov and Maslov (2002)] Ugolnikov, O.S., and Maslov, I.A., Multi-color polarimetry of the twilight sky - The role of multiple light scattering as a function of wavelength, *Cosmic Research*, 40, p.224, 2002.
- [Vegard (1938)] Vegard, L., Vorgnge und Zustnde in der Nordlichtregion, *Geofys. Publikasjoner* 12, No. 5, 1938.
- [Vegard (1948)] Vegard, L., Emission spectra of night sky and aurora, Report of the Gassiot Committee, *The Physical Society London*, 82, 1948.
- [Wagner (1984)] Wagner, W. J., Coronal Mass Ejections, Annual review of astronomy and astrophysics, Palo Alto, CA, *Annual Reviews*, 22, p. 267-289, 1984.

[www.wsrcc.com] <http://www.wsrcc.com/wolfgang/gps/accuracy.html>

[XEphem (2000)] Xephem, [www.xephem.com](http://www.xephem.com)